Aspect Ratio Effects on Wings at Low Reynolds Numbers

by

Ali A. Abtahi

Dissertation submitted to the Faculty of the
Virginia Polytechnic Institute and State University
in partial fulfillment of the requirements for the degree of
Doctor of Philosophy
in
Aerospace and Ocean Engineering

APPROVED:

J. F. Marchman III, Chairman

J. A. Schetz

B. Grossman

W. L. Neu

E. M. Kaiff

May, 1985

Blacksburg, Virginia

ACKNOWLEDGEMENTS

I would like to express my appreciation to Dr. J. F. Marchman III for his guidance and advice during the time of the preparation of this dissertation and for his help in setting up the wind tunnel experiments.

Also sincere thanks to Drs. J.A. Schetz, B. Grossman, W.L. Neu and E.M. Cliff for agreeing to be on my advisory committee.

Finally I would like to thank Mr. G.C. Bandy for always being very helpful in the operation of the wind tunnel and the building, testing and operation of all the hardware used in this study.

This work was supported by the Office of Naval Research.

TABLE OF CONTENTS

LIST OF VARIABLES

AR = aspect ratio

AR_{el} = aspect ratio for elliptic lift dist. wing

b = wing span

c = airfoil chord

C_l = lift coefficient

C_d = drag coefficient

C_{di} = induced drag coefficient

e = span efficiency factor

L = lift force

m = actual lift slope

m_0 = 2-D lift slope

p = downwash velocity ratio

Re_c = Reynolds number based on wing cord

Re_{δ}^* = Reynolds number based on displacement thickness

S = total Wing area

$\vec{u}$ = unit vector

U = non-dimensionalized velocity (with V_∞)

V_∞ = free stram velocity

V = aircraft velocity

w = indiced velocity

x = coordinate in direction opposite of relative wind

y = coordinate in direction of right wing

GREEK SYMBOLS

α = angle of attack

α_{l0} = zero lift angle of attack

ρ = air density

μ = air viscosity

ν = kinematic viscosity

δ = boundary layer thickness

δ^* = displacement thickness

Γ = circulation

1.) INTRODUCTION

The desire of the United States Navy to design a remotely piloted vehicle which can cruise at ship speed, just above the surface of the sea, has led to the need for data concerning aerodynamic behavior of wings at low Reynolds numbers.

Fig. 1.1 is a plot of Reynolds number versus flight speed for various types of aircraft. Clearly most aircraft operate at Reynolds numbers above 1,000,000. This is especially true for commercially significant types of aircraft. Aircraft that operate below a Reynolds number of 1,000,000 are mainly gliders and model airplanes. These however do not represent a commercially interesting branch of the airplane industry and correspondingly little research has been devoted to the study of aerodynamics especially pertaining to these aircraft.

Most data obtained in the past for wings at low Reynolds numbers have come from model airplane or sailplane enthusiasts. The earliest such work was that of Schmitz (1) for model airplane wings. Schmitz was the first to report the now fairly well known stall hysteresis effect seen on airfoils at low Reynolds

numbers. In another effort to provide data to model airplane designers, Althaus (2) of the University of Stuttgart, studied a selection of airfoils and obtained 2-D lift and drag data. Other studies were conducted at the University of Delft (3), again determining only lift and drag for two dimensional airfoil sections.

In 1981, as interest in low Reynolds number wing aerodynamics increased in the United States, Carmichael (4) published an excellent survey paper on the subject. Within the last few years, interest has continued to increase and research is now being performed in several U.S. Universities. Most of this work however still appears to concentrate on 2-D airfoils rather than on 3-D wings and to examine only lift and drag behavior. No pitching moment data has been published at this time.

Some consideration should be given to the various factors that cause an airplane to end up operating in the low Reynolds number regime. Considering the definition of Reynolds number and lift coefficient :

$$Re = \frac{\rho V c}{\mu} \qquad 1.1$$

$$C_l = \frac{L}{\frac{\rho}{2} V^2 S} \qquad 1.2$$

and assuming straight and level flight we can write

$$L=W \tag{1.3}$$

Substituting this into eqn. 1.2 and combining with eqn. 1.1 results in

$$Re = \sqrt{\frac{\rho}{\mu^2}\frac{2W}{C_l}\frac{c^2}{S}} \tag{1.4}$$

For an unswept wing with any planform

$$\frac{c^2}{S} = \frac{1}{AR} \tag{1.5}$$

Substituting 1.5 into 1.4

$$Re = \sqrt{\frac{\rho}{\mu^2}\frac{2W}{C_l}\frac{1}{AR}} \tag{1.6}$$

Eqn. 1.6 demonstrates to some extent the effects of the various operating parameters of an aircraft on the wing Reynolds number. It can be seen that the Reynolds number is proportional to $\sqrt{\frac{\rho}{\mu^2}}$. This factor generally decreases with increasing altitude in the atmosphere. At sea level and under standard conditions it is $8.79*10^4$ at an altitude of 30,000 ft it decreases to

$6.28*10^4$ and at 60,000 ft it becomes $2.96 * 10^4$. Above an altitude of 60,000 ft the decrease in this factor becomes even more rapid.

The other two factors influencing the Reynolds number directly are $\sqrt{\frac{2W}{C_1}}$ and $\frac{1}{\sqrt{AR}}$. From these one sees that low weight in combination with a high operating C_1 and high aspect ratio will mean lower Reynolds numbers. It should be noted that an aircraft with more than one wing, as for instance biplanes and canards, will have a lower effective chord to wing area ratio and thus will fly at lower Reynolds numbers also.

Since the apparatus required for control of a remotely piloted vehicle is in general much lighter then a human pilot and all the associated support equipment, these aircraft are more compact and overall weight is much smaller. Thus remotely piloted vehicles (RPV's) will be very likely to end up operating at low Reynolds numbers.

The references cited above have generally shown that between Reynolds numbers of 70,000 and about 500,000 flow separation on an airfoil is subject to a hysteresis phenomenon. This occurs because of the existence of a laminar separation bubble near the leading edge of the upper surface of the airfoil. In the "normal" hysteresis loop, the behavior is as

follows:

1. At low angles of attack, there is laminar separation followed by transition to a turbulent flow which causes flow reattachment.

2. As the angle of attack is increased, the location of the turbulent boundary layer separation moves forward over the rear of the airfoil's upper surface in a manner similar to that seen at higher Reynolds numbers.

3. A stall angle is reached where the flow breaks away from the entire airfoil upper surface at the laminar separation location.

4. If the angle of attack is now reduced, the pattern will not reverse itself; i.e. the flow will not reattach at the stall angle. Some lower angle of attack must be reached before the flow is able to reattach and the laminar bubble reform.

The problem that results from this hysteresis loop behavior in stall is the airfoil's inability to recover easily from stall. This is a potentially dangerous situation, especially for a vehicle flying at low speeds (near stall) and subject to gusts and low altitude.

Reverse hysteresis loops have also been observed on some airfoils in this Reynolds number range. Here the flow separates early as the angle of attack is increased but when it is later decreased a higher C_{lmax} is reached (5).

Below a Reynolds number of 70,000 the airfoil used in this study shows laminar separation and behaves much like an ordinary flat plate with separated upper surface flow at most positive angles of attack.

Many unknowns still exist with regard to low Reynolds number airfoil behavior. It is known that the size and shape of the hysteresis loop is dependent on the shape of the airfoil. Most work on laminar separation bubbles is two dimensional in nature and even here it is not quite clear why reattachment occurs in one case (corresponding to the upper branch of the hysteresis loop) and fails to occur in another (on the lower branch of the hysteresis loop). The effects of three dimensionality of the flow on the laminar separation bubble were previously not known at all.

It can also be assumed that wind tunnel noise and turbulence can greatly affect the results of tests in this range since both are well known to influence boundary layer stability; i.e. transition and

separation. Presumably also the "history" of the boundary layer at the location of laminar separation determines if turbulent reattachment will occur or not. Unfortunately, not enough studies have been done in different wind tunnel facilities to define the role of wind tunnel turbulence and noise in observed low Reynolds number test results.

A unique type of wind tunnel test facility appears to be needed for low Reynolds number airfoil and wing research. The facility must be able to maintain a steady flow at low speeds. It must be acoustically quiet and have a low turbulence free stream flow. In addition to these flow qualities, the tunnel needs force and moment balances and pressure measurement equipment sensitive enough to accurately measure the small forces, moments and pressures found at low Reynolds number conditions.

It is also mandatory that measurements be made via a remotely controlled balance system. Without such a system the hysteresis loop cannot be observed. For instance, if a hysteresis loop exists between the angles of attack of 12 and 18 degrees and if the wind tunnel is started up with the airfoil at an angle of attack between these values, one will only observe one

leg of the loop. For a normal loop, without a remotely controlled balance, only the lower or separated part of the loop will be seen.

The Virginia Tech Stability Wind Tunnel is one of the very few facilities in the nation capable of successfully obtaining accurate wing aerodynamic data at low Reynolds numbers. This facility has documented free stream turbulence intensities of 0.02% or less and a very sensitive, remotely operated six component strain gauge balance system.

The primary purpose of this research was to investigate the effects of aspect ratio on the low Reynolds number aerodynamic behavior of the Wortmann FX-63-137 airfoil. Two dimensional data exists for this airfoil at low Reynolds numbers but no 3-D data exists with pitching moment results and, to the authors' knowledge, no studies have ever been done to examine aspect ratio effect on the low Reynolds number behavior of any airfoil. Hence the primary objective was a systematic study of aspect ratio influences on the low Reynolds number behavior of the test airfoil.

Because of past questions about the reliability of various wind tunnel measurement techniques at low Reynolds numbers, a second purpose was to examine the effectiveness of several experimental methods of

measuring forces and moments on wings at low Reynolds numbers. Force measurements are difficult in this regime because of the very small magnitudes of the aerodynamic loads (particularly drag forces). This may be one reason why most investigators in the past have attempted to obtain drag data primarily via the "wake rake" technique.

In spite of the fact that the wake rake technique and the surface pressure integration method are essentially 2-D methods, they still provide valuable information about both the accuracy of the results obtained by the strain gauge method and in the case of surface pressure measurements the flowfield around the airfoil itself.

Some researchers in the past have observed that at high Reynolds numbers the flow over a wing in the post stall regime shows distinct cellular structure. The question existed wether in the case of low Reynolds numbers the same three dimensionality of the flow is present or not. One of the purposes of this study was to ascertain what types of flow patterns exist in the post stall regime.

Also it was unknown what the effect of the presence of the wingtips on the laminar separation

bubble is. The laminar separation bubble has traditionally been looked at from a two dimensional point of view since 3-D separation is an especially complex problem. It is essential therefore that the laminar separation bubbles' behavior be examined under 3-D flow conditions.

Another effect that could be present is that of disturbances generated by the presence of pressure taps. Some speculation exists on the effects that pressure taps could have on the laminar separation bubble. Therefore in this study the effects of pressure taps on the flow as a whole and on measurements made from other taps is examined in detail.

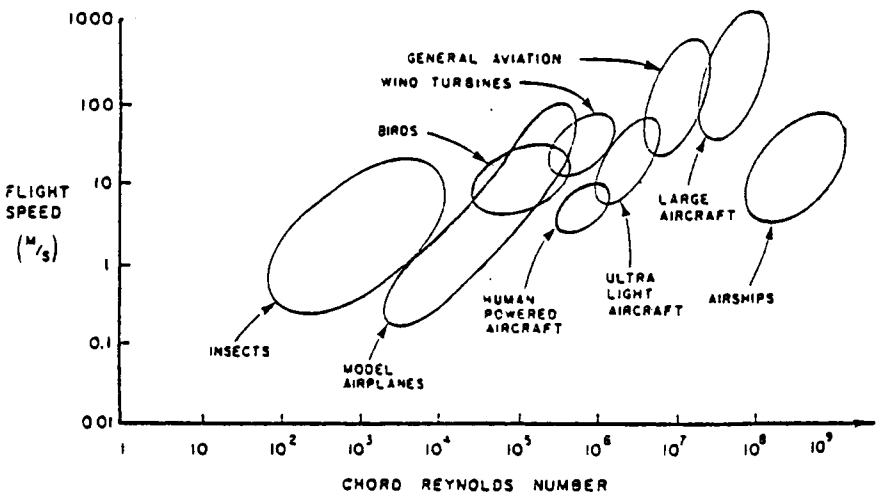

Fig. 1.1 Reynolds number range for various aircraft

2.) THEORETICAL BACKGROUND

2.1) The Laminar Separation Bubble

The laminar separation bubble is a phenomenon that occurs on most airfoils at low to moderate Reynolds numbers. A low, chord-based Reynolds number generally means that a significant part of the boundary layer will be laminar and that natural transition to a turbulent boundary layer would take place far back on the airfoil. This in turn implies that the laminar boundary layer is subject to a large region of severe adverse pressure gradients. It is well known however that a laminar boundary layer is not able to withstand adverse pressure gradients as well as a turbulent boundary layer due to the lower momentum transfer rate within the layer. This leads to the occurence of laminar separation on airfoils operating at low Reynolds numbers.

At high Reynolds numbers natural transition occurs early enough on the upper surface of an airfoil to only leave the turbulent portion of the boundary layer exposed to the high adverse pressure gradients present at angle of attack and on an airfoil with finite thickness. This precludes laminar separation and in general means higher stalling angle for the airfoil.

It is appropriate here to look briefly at the details of the transition and separation processes. In the presence of favorable and zero pressure gradients the mechanism responsible for the occurence of transition is basically the growth of unstable disturbances. Initially these disturbances are two-dimensional; however, they quickly become three-dimensional, and finally the boundary layer flow becomes fully turbulent. Fig. 2.1 shows an idealized sketch of transition on a flat plate in the absence of any localized surface disturbance. Similar patterns have been observed for favorable pressure gradients by Knapp and Roache (6). An approximation for the transition Reynolds number based on the displacement thickness of the boundary layer can be given by

$$Re_{\delta^*,tr} \simeq 2900\, e^{.08\Lambda} \qquad 2.1$$

where $\Lambda = \frac{\delta^2}{\nu}\frac{dU}{dx}$. One can see that $Re_{\delta^*,tr}$ is not a strong function of the pressure gradient. Substituting the definition of Re_{δ^*} into eqn. 2.1 and rearranging we obtain

$$\delta^*_{tr} \simeq \frac{\nu}{V} 2900\, e^{.08\Lambda} \qquad 2.2$$

If we assume for a moment that the non-dimensionalized pressure gradients on an airfoil do not change significantly with Reynolds number, (this of course is only possible within a small range of Reynolds numbers) it can be seen that the approximate displacement thickness at which natural transition occurs will be inversely proportional to the velocity.

Thus, barring a significant change in pressure gradients, the location of transition will move forward on an airfoil as free stream velocity is increased. This change in transition location is more rapid in regions of adverse pressure gradients ($\Lambda>0$) than in regions of favorable pressure gradients. Therefore on the upper surface of an airfoil at very high velocities transition will occur near the leading edge and in a region of favorable pressure gradients.

As the velocities are decreased the location of transition will move rearward and reach a point where the pressure gradients are adverse. At this point the possibility of an additional phenomenon has to be dealt with, namely that of laminar separation. It can be said in general that laminar boundary layers do not have the capability to withstand adverse pressure gradients for very long, and laminar separation occurs quite readily

after encountering an adverse pressure gradient. Thus as the velocity is decreased such that the transition point is pushed beyond the minimum pressure area laminar separation begins to appear.

Unfortunately the prediction of transition is an extremely difficult problem and, to date, available methods are either prohibitively complex, or based on approximations and empirical results. The problem becomes especially complex when one has to deal with a boundary layer that has evolved under the influence of varying pressure gradients as is the case on an airfoil.

A similar situation presents itself when one deals with the prediction of laminar separation. Most of these methods require detailed knowledge of the entire history of a boundary layer to make a prediction of the velocity profile and separation location. The history of the boundary layer, however, depends on the shape of the airfoil, on the angle of attack and naturally on the chord based Reynolds number Re_c.

Several attempts have been made in the past with varying degrees of success to write a computer code for the prediction of transition and laminar separation. In this study the code developed by Eppler and Sommers (8) has been used to attempt to predict boundary layer flow

on an airfoil.

The appearance of laminar separation does not mean in most cases that the flow is completely separated from that position onward. The laminar free shear layer that immediately follows behind the separation point represents a particularly unstable situation and therefore transition to turbulence occurs quite readily. The turbulence spreads and soon reaches the surface. If certain conditions are met, a short distance downstream the velocity profile of the flow becomes that of a turbulent boundary layer. Thus the laminar separation bubble acts in most cases the same way a boundary layer trip would function.

Fig. 2.2 shows a cutaway view of a laminar separation bubble. It should be noted that the vertical scale is expanded ten-fold so that the bubble is much flatter in reality.

In certain other cases the reattachment fails to occur in the way described above. Here the flow does become turbulent soon after laminar separation occurs but fails to form a turbulent boundary layer at this point. Instead the usual pattern for a fully separated flow is observed.

The length of the bubble naturally varies with

airfoil shape, angle of attack and Reynolds number. Some researchers have observed two distinct bubble types (short bubbles and long bubbles) on the same airfoil under different conditions. In general, laminar separation bubbles that are small enough not to change the character of the external flowfield significantly are called short bubbles. The actual length of the short bubble might be quite large. This terminology is actually quite inadequate since many variables (i.e. airfoil shape and Reynolds number) determine whether a bubble will be called long or short. It is not quite clear to date whether the two distinct bubble types are different flow phenomena or just manifestations of the same phenomenon under different conditions. Problems arise due to the fact that long bubbles significantly alter the surrounding flowfield whereas small bubbles do not cause such changes.

Thus the flow over an airfoil can be of four different types :

1.) Laminar separation at the leading edge with no reattachment.

2.) Formation of the short laminar separation bubble.

3.) Formation of the long laminar separation bubble.

4.) Natural transition before appearance of adverse pressure gradients and thus, no separation near the leading edge.

Case 4.) can be observed only at high Reynolds numbers. Cases 1.), 2.) and 3.) were observed to happen in the Reynolds number range used for this study.

This leads to the question of what the cause is for reattachement after separation and exactly what geometry the laminar separation bubble has.

One can assume that the pressure gradient in the region of the bubble would have a strong effect on the ability of the turbulent layer to attach itself to the surface. The other factor involved must be the rapidity of the breakdown of the laminar shear layer and transition to turbulence. In the past both of the above factors were used separately and later together in attempts to predict the behavior of the bubble.

In 1948 Maekava and Atsumi (9) found that flow reattachment did not occur when the bubble length Reynolds number exceeded 75,000. In the mid 50's Mc.Cullough and Gault (10,11) found that $Re_{\delta,sep}^{*}$ had to exceed 500 for reattachment to occur after a short bubble. The use of $Re_{\delta,sep}^{*}$ is quite logical since this

Reynolds number is in a way representative of the history of the boundary layer and thus contains information about the presence of instabilities. More recently powerful numerical techniques have been applied to the laminar separation bubble problem (14,29,30,31). The approach that is used here is either that of solving the Navier-Stokes equations or the use of viscous-inviscid interaction methods. The viscous-inviscid interaction schemes involve the solution of the boundary layer equations and the inviscid outer flow in parallel until they "match". This method is used by Carter and Vatsa (29), Davis and Carter (30) and Gleyzes, Cousteix, and Bonnet (31) with considerable success. In fact the results from the computations done with the viscous-inviscid interaction schemes are in the same good agreement with experimental results as the computationally more expensive Navier-Stokes solutions.

The shape of the bubble is shown in Fig. 2.2. A good approximation is to say that the separation streamline is tangential to the airfoil surface. Its length depends, as was stated before, on both the disturbance environment and the pressure gradients present on the airfoil. References 10,11, and 12 contain both experimentally determined and computed

present on the airfoil. References 10,11, and 12 contain both experimentally determined and computed results for bubble length.

Research is currently under way to better understand the mechanisms involved in causing reattachment to occur. The most promising approach is the incorporation of boundary layer stability analysis into the calculations since this is one major factor in causing reattachment.

The influence of the existence of a bubble on skin friction is evident and need not be discussed any further. The effect of the bubble on the inviscid outer flow, however, should be described briefly. If the thickness of the bubble is of the order of one boundary layer thickness there is very little influence of the bubble on the pressure distribution, since the effective shape of the airfoil is changed by a small amount only. This means small changes in lift, but still can mean noticeable changes in drag since on an airfoil with no large regions of separation the viscous drag is the dominant factor.

Unfortunately sometimes laminar separation bubbles are quite large relative to the airfoil so that the effective airfoil shape changes sufficiently to produce

completely different pressure distributions. Now of course both, lift and drag will change. The airfoil will perform very poorly. Usually the large bubble and completely separated flow are quite similar. The suction peak at the leading edge dissappeares almost completely and pressures are uniform over almost the entire upper surface.

2.2) Airfoil Stall at Low Reynolds Numbers

One of the major effects of low Reynolds numbers is the reduction of the stalling angle and changes in stalling characteristics so that a discussion of the various stalling types is necessary at this point.

It is appropriate to start with a brief description of the "usual" stall pattern, i.e. the type that occurs at high Reynolds numbers. This type of stall is commonly referred to as trailing edge stall.

As the angle of attack of an airfoil is increased, the turbulent boundary layer on the upper surface is subject to increasingly severe adverse pressure gradients. This causes the boundary layer to be unable to stay attached all the way to the trailing edge. A loss in lift and increase in drag results from this separation. The special characteristic of this type of stall is that as the angle of attack is increased the separation point gradually moves forward on the upper surface of the airfoil and thus, with the gradual increase in the area of the separated flow, the lift decreases gradually. Fig. 2.3 shows a typical C_l versus α curve for this type of stall.

The appearance of a short laminar separation bubble by itself does not change the lift very much as was pointed out earlier, however, if a laminar

separation bubble is present this can have significant effects on the stalling behavior. The bubble itself moves forward on the airfoil as α is increased, since laminar separation occurs earlier. At some point the bubble moves into a region with such severe adverse pressure gradients that reattachment fails to occur. Here the flowfield around the airfoil changes abruptly from attached to separated close to the leading edge. This will cause a sudden and severe drop in lift and increase in drag. Fig. 2.4 a) shows this kind of stall.

It is possible that abrupt flow separation as described above is preceded by some separation at the trailing edge. In this case the lift will first decrease gently as observed with trailing edge stall and then drop abruptly. Fig. 2.4 b) shows the $C_l \rightarrow \alpha$ curve for this kind of stall. This type of stall in general occurs at intermediate Reynolds numbers (between 100,000 and 300,000) since here the bubble is comparatively small and reattachment can occur over a range of angles of attack.

As Reynolds numbers drop below 100,000 two things can happen. Either the bubble size becomes sufficiently large to encompass almost the entire upper surface of the airfoil, or the flow is unable to reattach

altogether. If the leading edge radius is sufficiently large and the Reynolds numbers are not extremely low it is possible for a bubble to form but since it is very long and rather thick it changes the pressure distribution around the airfoil significantly and reduces the obtainable lift.

If the leading edge radius is very small or Reynolds numbers are extremely low, reattachment cannot occur since the laminar boundary layer separates immediately after forming. Again lift is reduced drastically.

Fig. 2.5 shows this type of stall which is classified as thin airfoil stall. This name is somewhat misleading since the airfoil in question does not necessarily have to be thin to display this type of stalling behavior. A low Reynolds number can cause this type of stall to occur even on rather thick airfoils. It should however be said that the thinnest of all airfoils i.e., the flat plate displays this type of stall and that this is probably where the name came from.

A detailed discussion of the three types of stall was first given by Mc Cullogh and Gault (10). All three types of stall were observed in this study on the FX-63-137 airfoil in the Reynolds number range from

50,000 to 500,000. Thus for this airfoil the most significant changes in behavior take place in this range. In Mc Cullough and Gaults' work, different airfoil sections were analyzed and thus the Reynolds number range where the changes take place is different.

2.3) Three Dimensional Effects

For most wings at relatively high aspect ratios the simple methods of Prandtl's Lifting Line Theory can be used to predict the effects of three dimensionality on wing performance.

On an infinite (2-D) wing the ciculation generated on the airfoil is constant by definition along the wing (in the infinite span-wise direction). In the case of the finite wing this cannot be the case since vortex lines cannot end at the wingtip (Helmhotz's Theorem). Thus the vortex lines extend downstream into the flow to form what is called a horseshoe vortex (Fig. 2.6 a). If the circulation in the span-wise direction varies, as is indeed the case on all wings, the change in circulation at every span-wise location will cause that much vorticity to spill into the wake of the wing. Fig. 2.6 b shows such a vortex system. At the wing this trailing vortex system induces a certain downward velocity component thereby reducing the actual angle of attack. This effect increases with the strength of the trailing vortex system which in turn increases with the angle of attack. The result is a decrease in lift slope and an increase in the drag.

Prantl's Lifting Line Theory assumes that the wing can be approximated by a line on which all the

circulation is generated and that the trailing vortex filaments are straight and at a 90 degree angle from the lifting line (as shown in Fig. 2.6 b). A detailed derivation of the resulting equations can be found in the various texts on applied aerodynamics (15,16,17). The famous monoplane equation relates the local angle of attack to the local circulation for each span-wise point.

$$\alpha-\alpha_{l0} = \left(\frac{2\,\Gamma}{m_0 V_\infty c}\right)_{y_0} + \frac{1}{4\pi V_\infty}\int_{-\frac{b}{2}}^{\frac{b}{2}} \frac{d\Gamma}{dy}\,\frac{1}{(y_0 - y)}\,dy \qquad 2.3$$

The remaining unknown here is the distribution of Γ which unfortunately is difficult to obtain in most cases. One easy solution to this problem is the use of an elliptical lift distribution as the base line case to which all others are related. The results are given here as equations for the induced drag (additional drag due to 3-D effects) and lift slope :

$$C_{di} = \frac{C_l^{\,2}}{\pi\, AR} \qquad 2.4$$

$$m = \frac{m_0}{1 + \frac{m_0}{\pi\, AR}} \qquad 2.5$$

For the case of a non-elliptical lift distribution slightly different approaches are used by the various texts. The approach used here is that of finding the

aspect ratio of the wing with an elliptical lift distribution that will produce the same effects as the given wing.

$$AR = e\, AR_{el} \qquad 2.6$$

Where e is the "span efficiency factor". The value for e is different for the same wing if used in the two different equations 2.4 and 2.5. Since the elliptical lift distribution produces the least 3-D effects (see reference 15 for confirmation) e is a number smaller than 1. In this study rectangular wings are used. These do not of course have an elliptical lift distribution so that it is necessary to find the span efficiency factor for each aspect ratio separately. This is done through the method of assuming a circulation distribution of the following form.

$$\Gamma = \frac{1}{2} m_{0_s} c_s V_\infty \sum_{n=1}^{\infty} A_n \sin n\theta \qquad 2.7$$

where the subscript s refers to the value in the plane of symmetry. Substituting this into eqn. 2.3 and using $y=\frac{b}{2}\cos\theta$ we obtain

$$\alpha+\alpha_{l_0} = \frac{(m_0 c)_s}{(m_0 c)_{\theta_0}} \sum_{n=1}^{\infty} A_n \sin n\theta_0 + \frac{m_0 c_s}{4\pi b} \int_0^{\pi} \frac{\frac{d}{d\theta}\left(\sum_{n=1}^{\infty} A_n \sin n\theta\right) d\theta}{\cos\theta - \cos\theta_0} \qquad 2.8$$

Now we can perform the differentiation and

integration to obtain :

$$\alpha+\alpha_{l_0} = \frac{m_{0_s} c_s}{m_0 c} \sum_{n=1}^{\infty} A_n \sin n\theta + \frac{m_0 c_s}{4b} \sum_{n=1}^{\infty} n A_n \frac{\sin n\theta}{\sin\theta} \qquad 2.9$$

From this the local angle of attack relative to the zero lift line is known and using it one can proceed to obtain the equations for lift slope and induced drag (for a detailed derivation of these equations see reference 15).

$$C_{di} = C_{di,el} \sum_{n=1}^{\infty} n \frac{A_n^2}{A_1^2} \qquad 2.10$$

$$m = \frac{m_0 A_1 \pi}{4} \qquad 2.11$$

Using e_d for the drag span efficiency factor and e_m for the lift slope span efficiency factor we obtain:

$$e_d = \frac{1}{\sum_{n=1}^{\infty} n \frac{A_n^2}{A_1^2}} \qquad 2.12$$

$$e_m = \frac{A_1 m_0}{4AR(1-A_1\frac{\pi}{4})} \qquad 2.13$$

In order to find e_d and e_m all that remains to be done is to find the coefficients A_n for equation 2.7. This however can be done easily with the use of eqn. 2.9 if one truncates the two summation sequences. For a rectangular untwisted wing with constant profile shape along the span equation 2.9 can be written in the

following form :

$$\alpha+\alpha_{l0} = \sum_{n=1}^{\infty} A_n \sin n\theta \left(1+\frac{m_0 n}{4 AR \sin\theta}\right) \qquad 2.14$$

For the purpose of solving this equation easily for the A_n's it is necessary to know the lift slope m_0 for the 2-D case. The value obtained for the profile used in this study by computation (panel method) agreed quite closely with the theoretical prediction of 2π so that it is a good assumption to say that the lift slope for the 2-D airfoil is equal to 2π. This does not hold true at Reynolds numbers below 100,000 since the behavior of the wing in this regime differed significantly from the predicted inviscid behavior, as can be expected, thus the analysis presented here is not valid at these extremely low Reynolds numbers. In this study only the case of a Reynolds number of 70,000 fell into this category and will be dealt with individually in section 4. With $m_0 = 2\pi$ eqn.2.14 becomes:

$$\alpha+\alpha_{l0} = \sum_{n=1}^{\infty} A_n \sin n\theta \left(1+\frac{n \pi}{2AR \sin\theta}\right) \qquad 2.15$$

Since this equation must be satisfied everywhere along the wing (i.e. for all angles of θ) a system of as many equations as one desires can be written from 2.16 so that for any choice of number of A_n's to be considered the right amount of equations can be

written.

Before this is done it becomes neccessary to analyze the influence of the wind tunnel walls on the 3-D effects on the wing. In this study wings with four different aspect ratios were used mounted horizontally in the center of the test section. The vortex filaments spilled into the wake of the wing are influenced by the fact that the wind tunnel walls restrict the flow. Fig 2.7 shows the rear view of a calculated flowfield without the walls for a vortex present at 10% tunnel width from the tunnel walls. Clearly the induced velocities are not tangential to the walls.

To find the proper correction to the flowfield due to the presence of the wall the method of images is used. The corrections are found by adding image vortices to the flowfield outside the physical tunnel boundaries to "straighten" the velocity vectors. The position of the image vortices is chosen such that the velocity vectors at the wall become parallel to it. Then the influence of this image vortex system on the flowfield in the vicinity of the wing is determined to find the effect of the walls on the wing.

For a square test section this problem becomes somewhat more difficult since there are four walls

present. Each time one wall is accomodated by an image system the other three walls now require images of the first image to be included. The result is a field of infinitely many vortex images in the plane under consideration. Fig. 2.8 shows the system of images used here. The assumption that has to be made here is that the vortex filaments that extend from the wing downstream are straight and parallel to all four tunnel walls. This can obviously not be the case in the real flowfield but in the past it has been shown experimentally that the theoretical predictions of 3-D effects using this assumption are accurate. The reason why this assumption is so crucial is that with it the Biot-Savart Law can be used to determine the velocities induced by these straight vortex filaments.

Fig. 2.9 shows the geometry used for the setup of the computations that were done to determine the wall effects in the special case of this study. It should be noted that the relative changes in the flowfield due to the image vortices are the same in any plane both upstream and downstream of the wing and therefore the image vortex system truly reproduces the tunnel wall effects in three dimensions.

The velocity induced at a given point in the plane to be analyzed and due to a vortex m can be found by

adding the contribution due to each of the infinitely many vortices present in the field.

$$\vec{w}_{i,m} = \sum_{n=0}^{\infty} \frac{\Gamma_{n,m}}{4\pi} \frac{\vec{u}_n}{d_n} \qquad 2.16$$

where $\vec{u}_n$ is a unit vector normal to the line connecting the point i (the location at which w is to be determined) and the location of the vortex. Since the strengths Γ_m of all the image vortices for a given vortex in the tunnel are the same the subscript can be dropped. Fig. 2.10 shows the effect of adding the image vortex system on the flowfield within the boundaries of the test section. Each arrow represents the velocity vector at that location. Clearly now the velocity at the tunnel wall is parallel to the wall.

For a trailing vortex system as the one given in Fig. 2.6 b it becomes necessary to include a complete image vortex system for each and every filament in the wake of the wing since each of the filaments can have a different strength and its location relative to the tunnel walls is different. So in order to find the induced velocity at some point P_i due to an entire trailing vortex system it becomes necessary to integrate over all the vortex filaments :

$$w_i = \int_{-\frac{b}{2}}^{\frac{b}{2}} \left(\sum_{n=0}^{\infty} \frac{\Gamma(y)}{4\pi} \frac{\vec{u}_n}{d_n} \right) dy \qquad 2.17$$

Eqn. 2.17 cannot be used in its present form. It is necessary to approximate both the integral and the infinite sum by some means that makes the equation suitable for computer solution.

For the integral the wing was subdivided into 20 segments each with a constant circulation. This gives a trailing vortex system of 20 discrete vortex filaments. Through this it is possible to replace the integral by a summation.

The infinite sum represents a more difficult problem since it is necessary to truncate the series and then estimate the truncation errors. To find out what upper limit for n would produce sufficiently accurate results several runs were made for one filament and 2 to 40,000 images. It turned out that for n>400 there were absolutely no changes in the computed value of the induced velocity (14 digits accuracy). Also it was ascertained that the velocity vectors were parallel to the tunnel wall as far as the resolution of the plotter is concerned even after using only 25 images so that a truncation of the series after considering 400 elements is accurate. Thus the series can be re-written as :

$$\vec{w}_i = \sum_{m=1}^{20} \sum_{n=0}^{N} \frac{\Gamma_n}{4\pi} \frac{\vec{u}_{n,m}}{d_{n,m}} \qquad 2.18$$

where N=400 if the images are to be present and N=0 if they are to be not present.

Finally it becomes necessary to find the Γ_m's. The procedure used here was to first find the Γ_m distribution by the method described in the beginning of this section and then to find the average changes in induced velocity at the wing due to the walls using the following equation :

$$p = \frac{\sum_{i=1}^{20} w_i(N)}{\sum_{i=1}^{20} w_i(0)} \qquad 2.19$$

Assuming that the shape of the downwash distribution does not change significantly it can be said that

$$AR_{eff} = \frac{AR}{p} \qquad 2.20$$

thus determining an effective aspect ratio. This means that a wing with a given physical aspect ratio will act as if it had an aspect ratio of AR_{eff}. Of course the downwash distribution is changed slightly by the images but this effect is not significant since the absolute changes in w_i are small to begin with at the model dimensions used here.

Once the effective aspect ratio corresponding to

the physical aspect ratio is found it is possible to return and apply the procedure described in the beginning of this section again to find the approximate values for e_d and e_m. Figs. 2.11 a),b),c) and d) show the circulation distribution, the strength of the trailing vortex sheet and the downwash velocity distribution for both cases with and without the walls present for the wing used in this study.

Fig.2.12 gives an overview of the results obtained for 3-D effects for the wing used in this study.

Because of the chord of the model being very small relative to the size of the test section no further corrections are required (blockage and 2-D streamline curvature). This is the biggest advantage of the large wind tunnel used in this study. In section 4 it will become evident that the theoretical 3-D effects described here are a remarkably good approximation even at low Reynolds numbers.

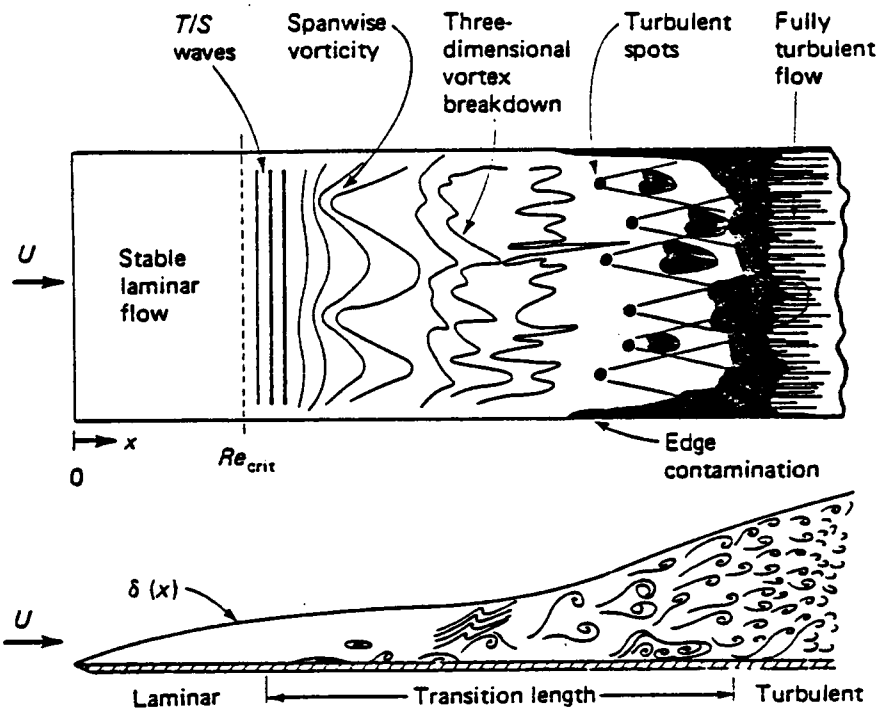

Fig. 2.1 Sketch of natural transition process

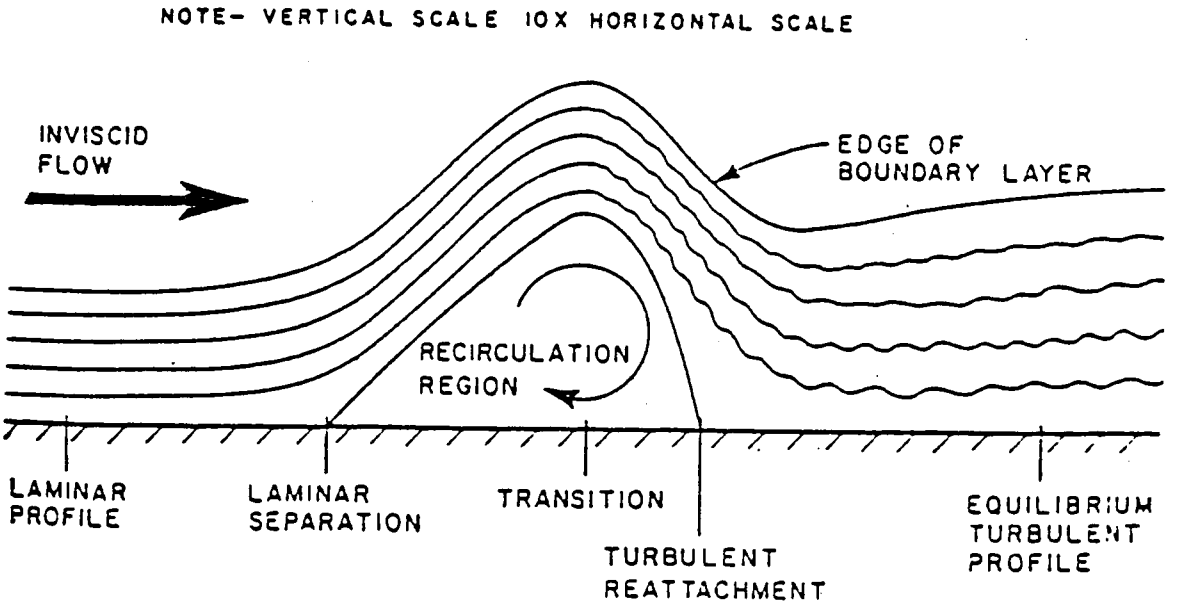

Fig. 2.2 Cross section of the laminar separation bubble

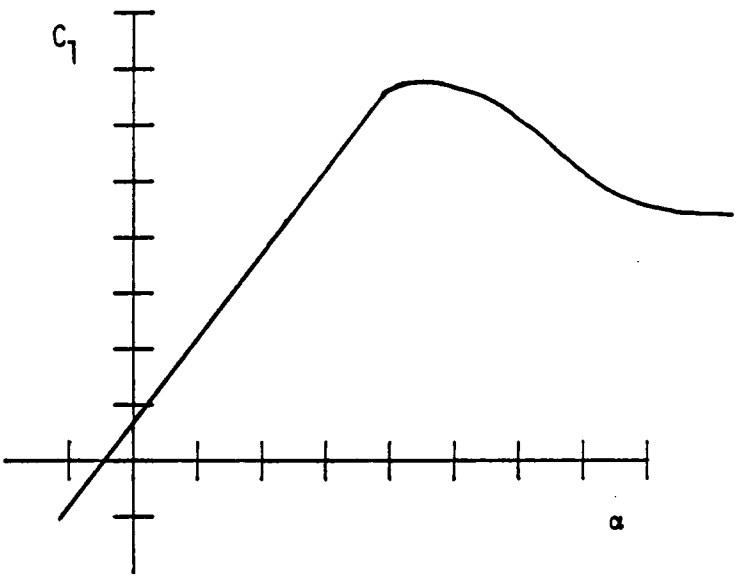

Fig. 2.3 Typical lift curve for trailing edge stall

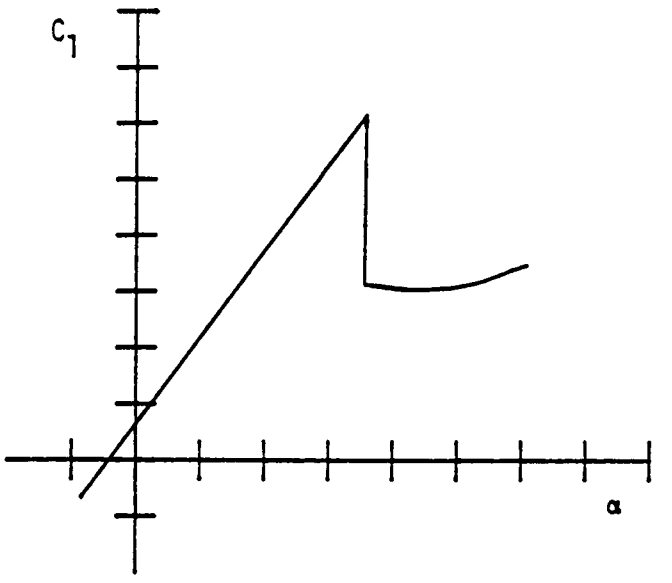

Fig. 2.4 a) Typical lift curve for leading edge stall

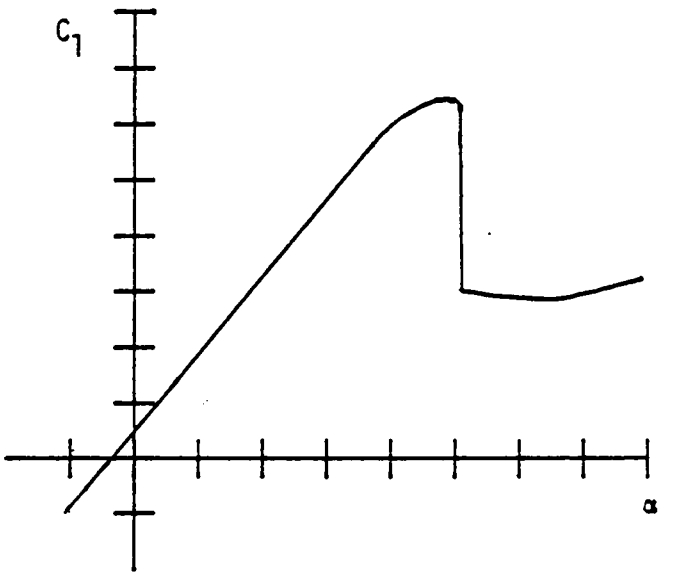

Fig. 2.4 b) Typical lift curve for leading edge stall preceded by some trailing edge separation

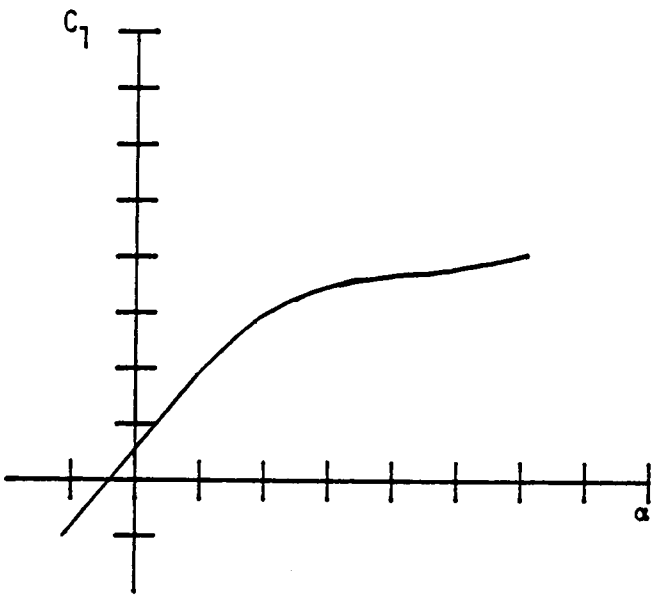

Fig. 2.5 Typical lift curve for thin airfoil stall

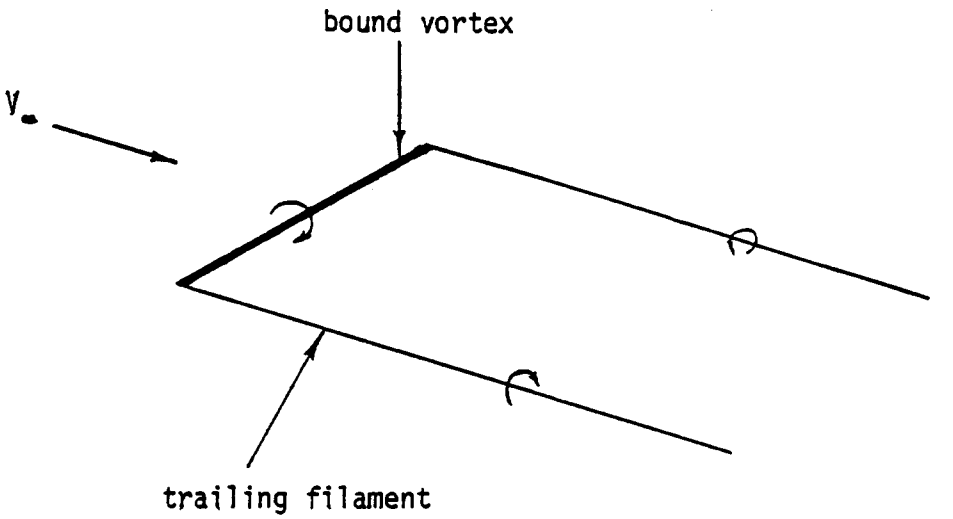

Fig. 2.6 a) Horseshoe vortex

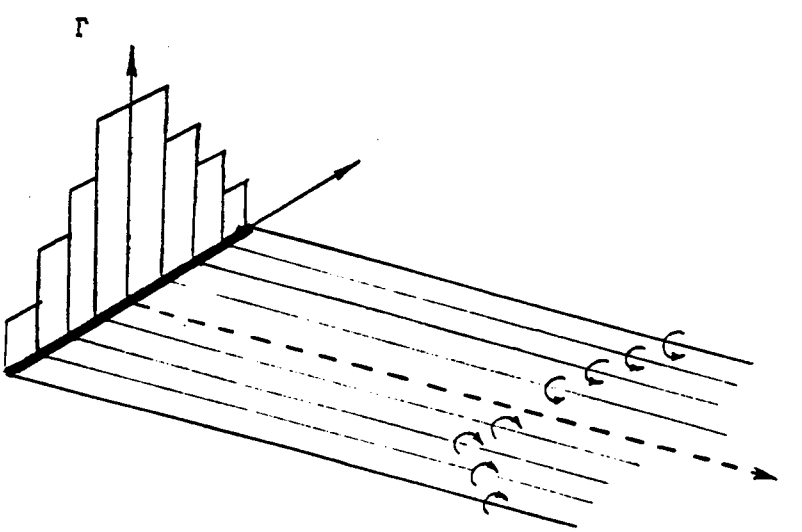

Fig. 2.6 b) Trailing vortex system to approximate shed vortex sheet

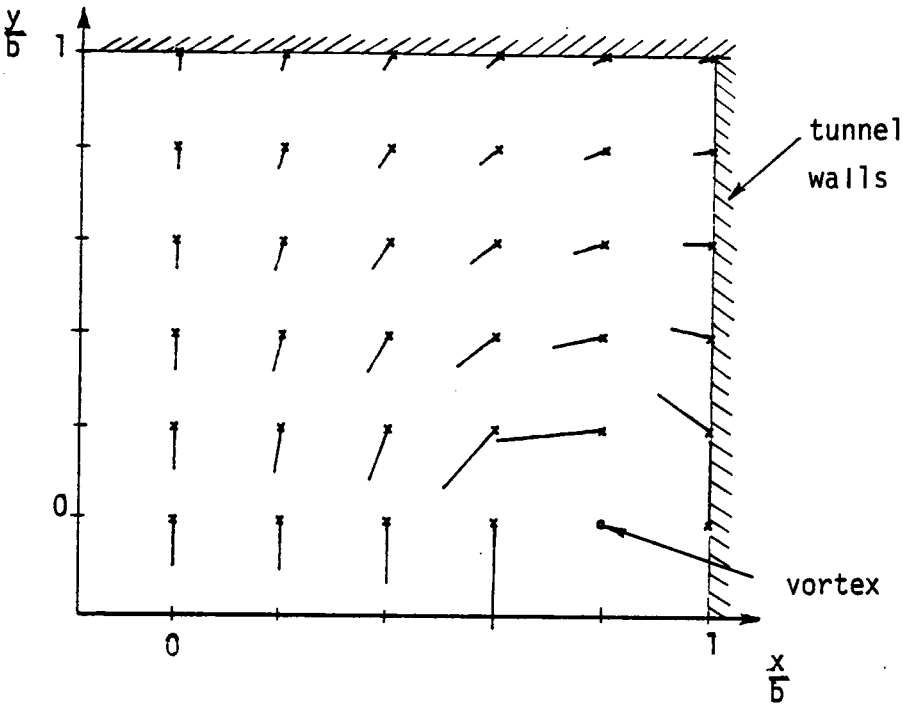

Fig. 2.7 Induced velocities in plane of bound vortex for a pair of trailing vortex filaments

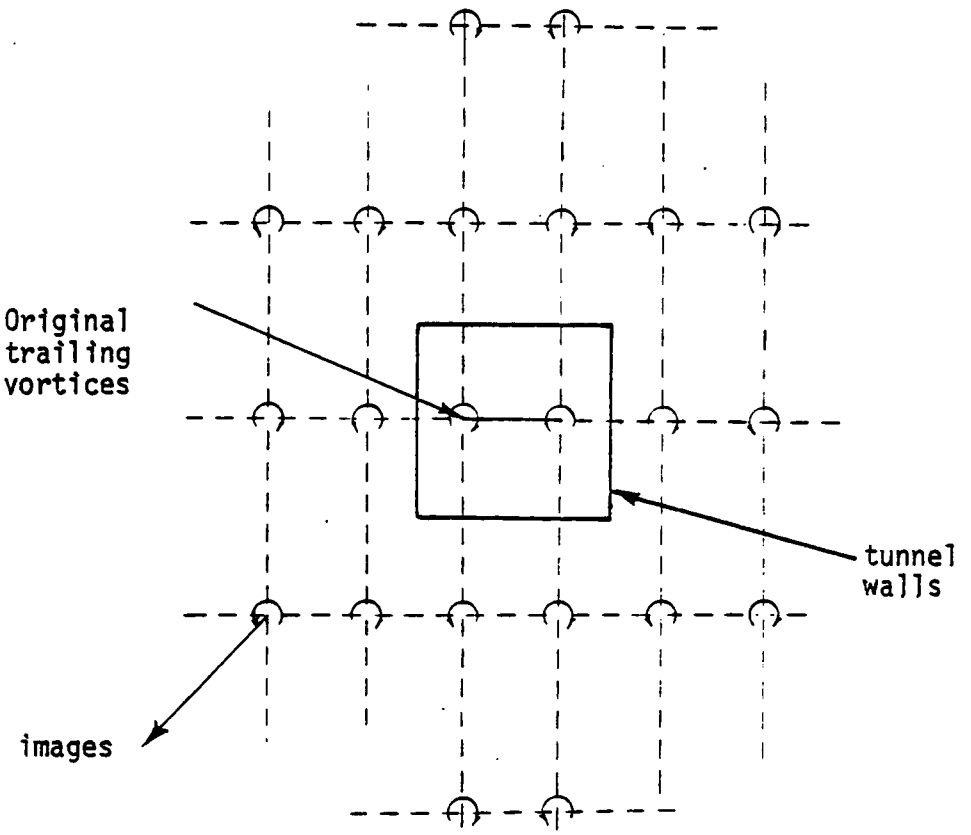

Fig. 2.8 Image vortex system

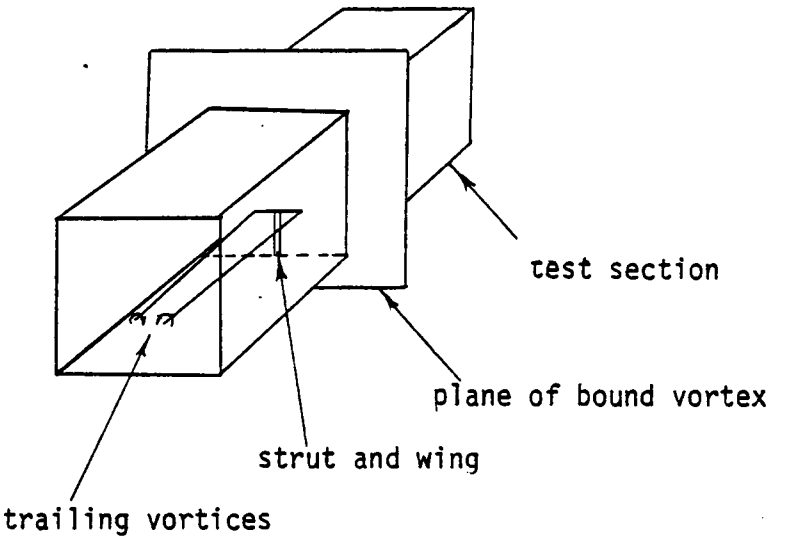

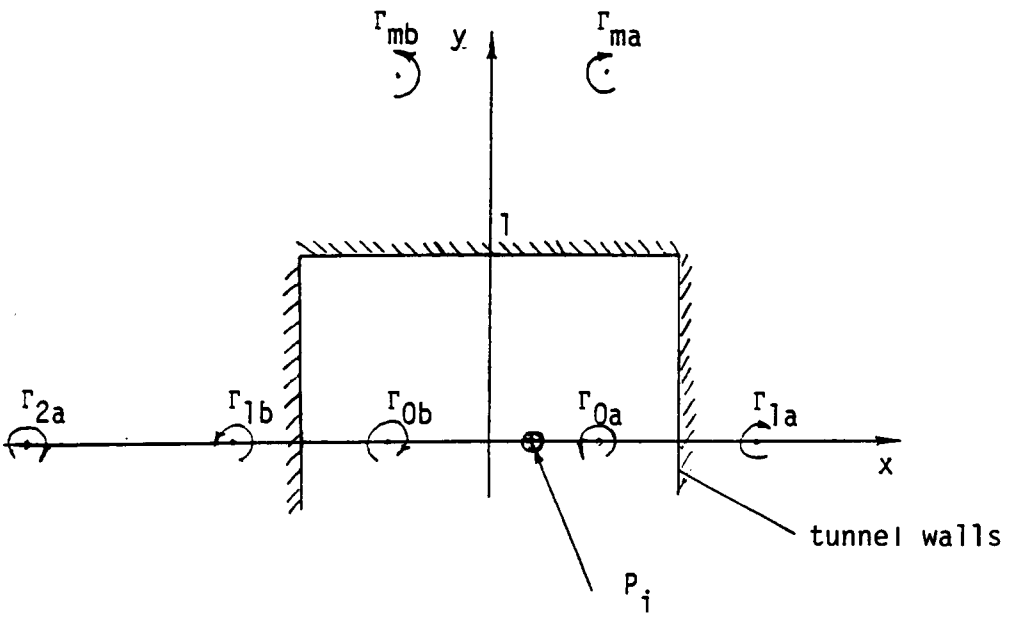

Fig. 2.9 Geometry used for computation

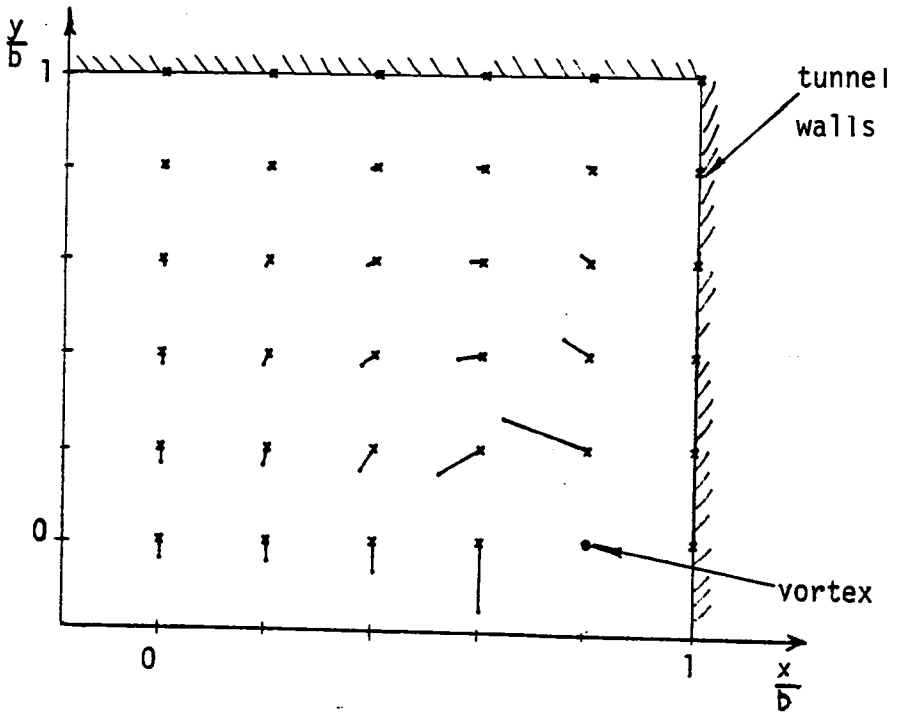

Fig. 2.10 Induced velocities in plane of bound vortex for trailing vortices and image vortices

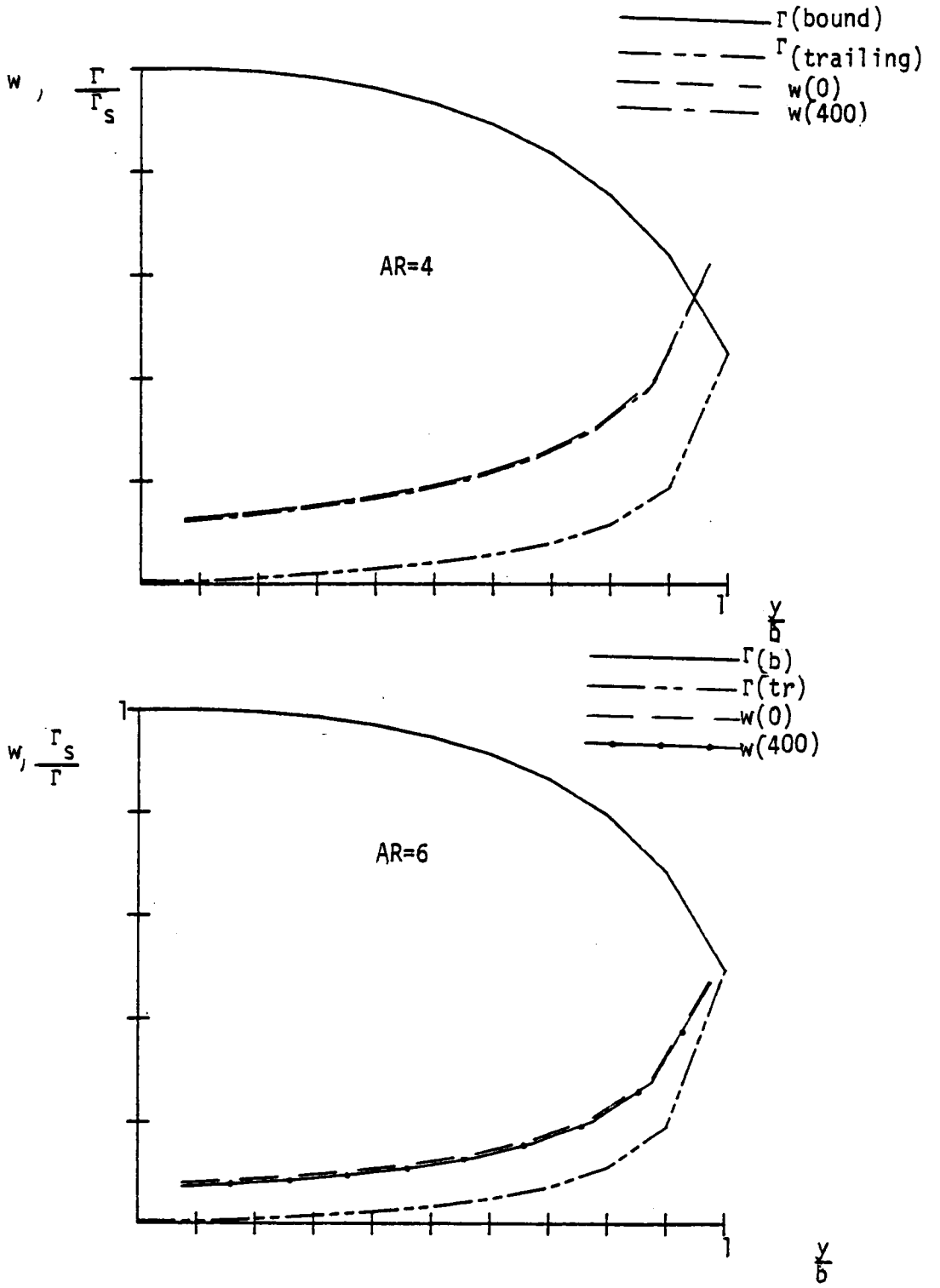

Fig. 2.11 Distribution of Circulation, trailing filament strength and downwash with and without image vortices

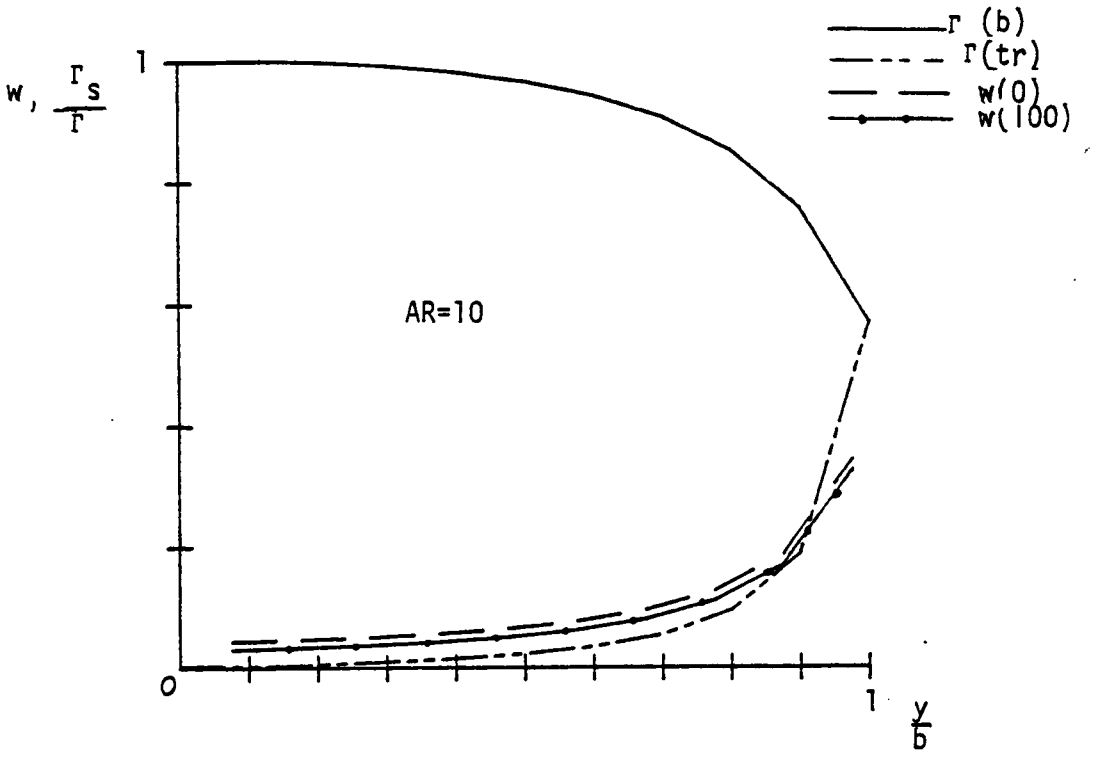

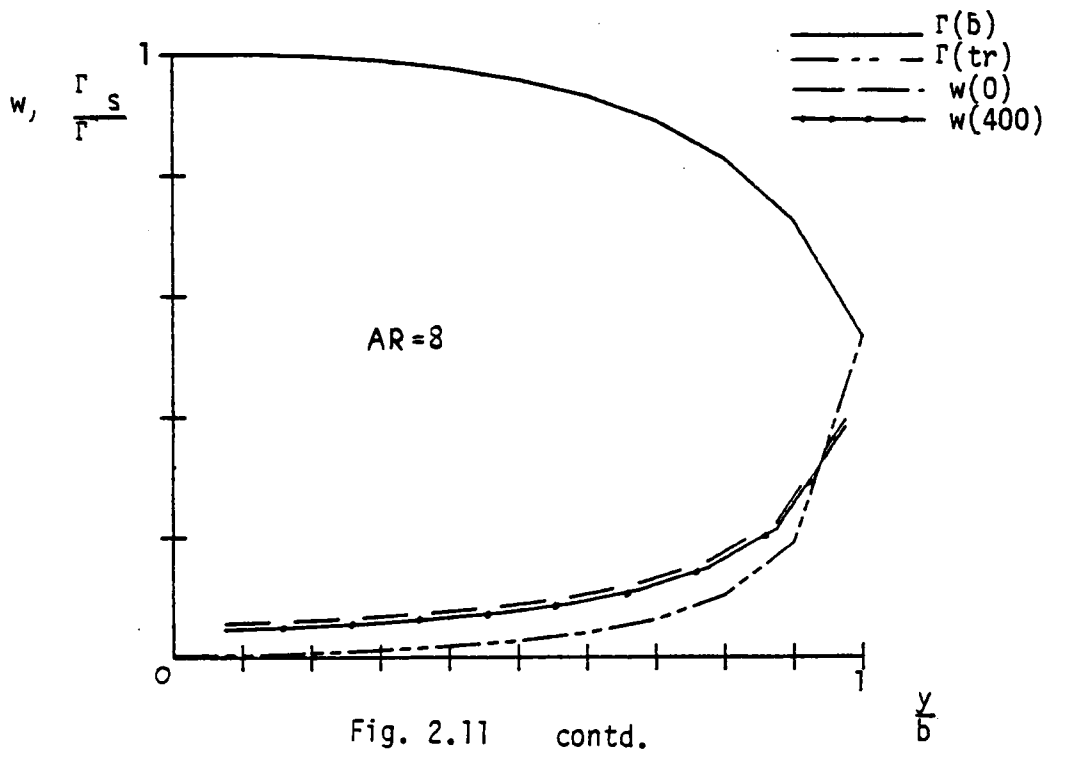

Fig. 2.11 contd.

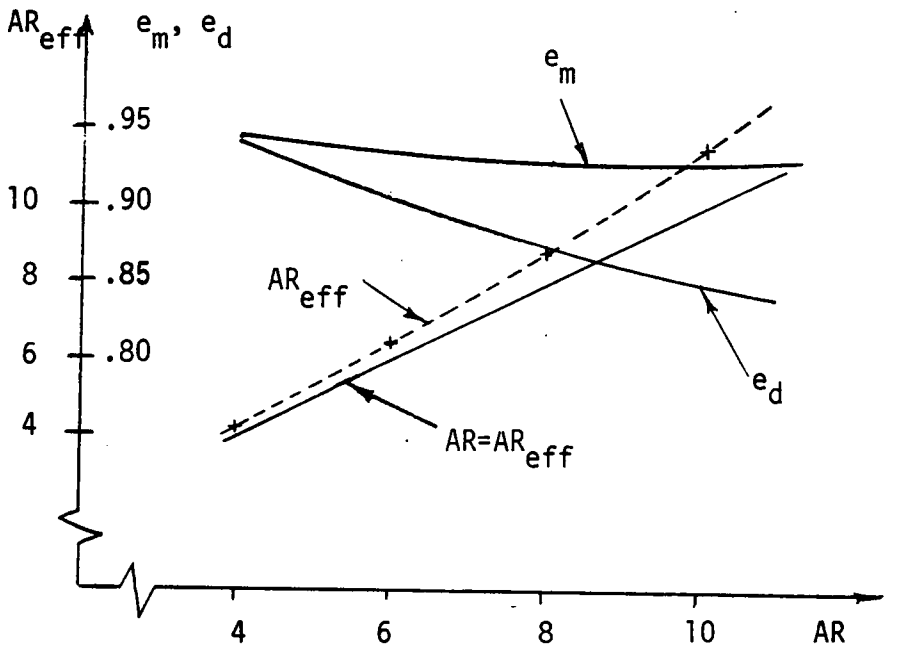

Fig. 2.12 Summary of results from lifting line calculations

3.) DESCRIPTION OF THE EXPERIMENTS

3.1) Description of the Model

The model used for this study was made with the contour of a FX-63-137-ESM airfoil. The FX-63-137 airfoil contour was developed by F.X. Wortmann of the University of Stuttgart to operate at the comparatively low Reynolds number of 500,000 which is a typical value for light glider aircraft. Later Eppler, also of the University of Stuttgart modified the coordinates for this airfoil slightly to give a rounder leading edge contour and to facilitate computation. The new shape was designated FX-63-137-ESM. Fig. 3.1 shows the contour of the FX-63-137-ESM airfoil. Also a list of the coordinates used to produce this model is given in appendix A.

The tests were performed with rectangular wing models with a physical aspect ratio of 4,6,8, and 10. At first several models were constructed using laminated wood, and a styrofoam core covered with thin plywood. These techniques for model building however proved to be too inaccurate to yield a model of sufficient quality both as far as reproduction of the coordinates and surface smoothness is concerned for this study. Thus it was decided to machine the models

out of solid blocks of aluminum.

The milling machine available in the shop of the Aerospace & Ocean Engineering Department at Virginia Tech unfortunately did not have enough travel to make it possible to machine a complete model with a span of several feet so that sections of 10 and 20 inch lengths were machined. After fastening the block of aluminum to the bench, the contour of the airfoil was projected into the block in the span-wise direction. To accomodate the variable slope of the wing surface, the machining head was tilted to the same angle as the local slope and the surface was then cut with the end of the cutter.

Since the tunnel test section is 6 feet wide it was decided that the span of the wing should not be more than 50 inches. For the largest aspect ratio (10) this dictated a chord of 5 inches.

One 20 inch section was machined to form the main piece. In this piece 4 holes were drilled and tapped after a 1" by 1" flat mounting area was machined to adapt it to the srut used. Also in the tips holes were drilled to accomodate the rods used for assembly and alignment of more pieces. Finally a channel in the middle of this piece was constructed to house the

pressure tubing to the outboard sections of the wing.

Two 10 inch and two 5 inch sections were then machined to complete the set of pieces for the model. Each of these pieces was provided with a hole through the center for the assembly rods. Fig. 3.2 shows a sketch of one side of the aspect ratio 8 model assembled. With these five sections it was possible to assemble any of the four different aspect ratios in a short time.

The two 10 inch pieces were also provided with a set of small holes near the upper and lower surfaces for the pressure experiments. Plastic tubing could be plugged into these holes later and to provide surface taps it was only necessary to drill a small hole from the surface to the span-wise hole. Fig. 3.3 shows a sketch of the technique used here. The advantage of this approach was that experiments could be done with only part of the pressure taps present. Thus by drilling more and more pressure taps from the surface to the respective channels the influence of the presence of pressure taps on the results could be observed.

After each aspect ratio assembly was complete it was necessary to assure that there was no seam or gap where the pieces were joined. This was done with the

use of a small amount of paint and careful finishing of the entire wing after each assembly was complete.

To facilitate flow visualization the entire model was painted red or yellow, whichever provided more contrast for the experiment at hand. Also, to protect it from the harsh chemicals used during some of the flow visualization experiments a thin coat of epoxy was applied to the surface of the wing.

For some of the experiments it was desired to have essentially 2-D flow over the wing so that it was necessary to construct endplates for the wing. These endplates could simply be added during assembly by adding them to the sections. Fig.3.4 shows the dimensions of the endplates and the way they were assembled into the model.

Two other models were used in order to supplement the data obtained for this study. One was a wooden model with a Clark-Y profile and the other a flat plate.

The Clark-Y model was constructed from laminated wood and covered with epoxy to assure surface smoothness.

The flat plate was cut out of 1/8 " thick aluminum plate with a chord of 5 inches and an aspect ratio of 6

3.2) The Wind Tunnel Facilities

All the experimental work conducted for this study was done in the Virginia Tech Stabilty Wind Tunnel.

This wind tunnel is a closed jet single return subsonic facility with a 6'x 6'x 22' test section. Originally this tunnel was built and used by NACA at Langley Field.

The drive of the tunnel consists of a 600 hp DC motor driving a 14' propeller and a motor generator as a power source. The maximum speed attainable in this tunnel is approximately 240 fps.

The controls and instrumentation are located in a airtight room surrounding the test section and accessible through an airlock. This design provides for the convenience of having the entire control room at the same static pressure as the test section during operation. Since pressures in the test section and the control room are equal the construction of the test section can be kept simple thus allowing easy access and modifications. Also connections made to and from models to the control and instrumentation area do not have to be airtight. Fig. 3.5 shows a sketch of the layout of the tunnel.

The control room houses both pertinent speed control instrumentation, and all the data acquisition

equipment.

The quality of the flow is of major importance for the type of experiments done in this study. Since transition to turbulence in the boundary layer influences the results, the presence of any type of disturbances in the free stream can influence the outcome of the experiments. It is imperative that the amount of disturbances in the free stream be kept to a minimum.

The present facility has free stream turbulence levels of the order of 0.02% and is acoustically exceptionally quiet. Free stream turbulence levels were measured by Saric et. al. (32) using hot wire anemometers. Also during this study turbulence levels were measured using the same technique.

During some of the experiments increased turbulence and noise were artificially introduced and proved to be of major consequence as far as the outcome of the experiments at these Reynolds numbers was concerned. Sumantran et. al. (20) showed in some detail what effect the free stream environment has on the performance of wings in this Reynolds number regime. Thus the Virginia Tech Stability Wind Tunnel seems particularly suited to conduct experiments at low

Reynolds numbers.

The low turbulence levels in the test section can be attributed to the fact that several anti-turbulence screens are located just upstream of the contraction in front of the test section. Also an air exchange tower located between the propeller and test section replaces the boundary layer continuously and thus reduces the total portion of turbulent flow in the tunnel. Finally also the air exchange tower isolates the test section from fan pressure pulse effects.

3.3) Description of the Data Acquisition Equipment

The data acqisition equipment currently in use at the Virginia Tech Stabilty Wind Tunnel is a Hewlett-Packard 3052 Automatic Data Acquisition System with a Hewlett-Packard 9836 Desktop Computer.

The HP 9836 computer is an extremely useful tool for high speed data acquisition. It has up to 1 megabyte of internal memory and two flexible disk drives. The computer language used during the entire time of these experiments was HP Basic Version 2.0. This language is very similar to Fortran but has built in additional capabilities that make the process of interaction with the various peripheral devices easier. The computer has the capabilty to communicate with externals both through a RS-232 serial interface and a HPIB 8 Bit parallel interface (IEEE 488 Protocol). Since all the instruments used here are HP supplied only the HPIB interface had to be used. For a detailed description of the language used here and the interfacing techniques the interested reader can consult reference 18.

In order for the computer to be able to process the information that is presented in the form of analog voltages, a Hewlett-Packard 3455A Digital Voltmeter was used. This device has the capability to measure

voltages (both DC and AC) at an optimum resolution of 0.5 microvolts. Up to 200 measurements can be made each second. Since the device does not have any internal memory all measurements must be immediately transferred to the host computer. This voltmeter also has the ability to perform periodic self-calibrations and accuracy-checks. This feature was used at all times during these experiments.

The input to the DVM is switched by a Hewlett-Packard 3495A Scanner. This scanner connects one or more of its 40 input channels to the input of the DVM at the host computers request. Thus the computer can select to measure any one of 40 inputs. The first 9 channels are hardwired to preset inputs at this facilty. Appendix B gives a table containing the channel assignments for these channels.

Finally, in order to enable the computer to actuate external devices, a Hewlett-Packard 59306A Relay Box was used. This device contains six individually controllable Potter Brumfield Relays. Through commands passed to the bus decoder on the HPIB each of the relays can be closed or opened by the computer.

For more detailed information on the operation of

the various components of the data aquisition system the reader is referred to reference 19.

The most important component of the equipment is probably the strain gauge strut and the associated bridge amplifiers. The system used here was originally designed and built by NASA-Langley and has been regauged for VPI by Dynamic Engineering Inc. of Newport News, Virginia. The voltage output is one millivolt per 22 lb. The noise generated in the amplifier and other components of the system causes fluctuations of +- 1 microvolt so that the forces applied to the strut can be measured to within an accuracy of +- .022 lb. This accuracy is sufficient for the purposes of this experiment except in the cases were Reynolds numbers below 70,000 were used. Here the data had to be fitted with a least squares curve to approximate the actual value.

The entire strut / model mount assembly was shrouded to preclude any drag other than the actual wing drag to be measured.

Tunnel conditions were measured through 3 different instruments. For static pressure a Validyne D899 electronic barometer was used. This unit measured the pressure in inches of mercury. The tunnel temperature was measured through a thermistor located

near the model about 3" from the tunnel wall. The thermistor was mounted on a wooden fixture to preclude contamination of the readings from heat conducted to it from the tunnel control room. The electronics associated with the thermistor gave a reading of the air temperature inside the tunnel in degrees farenheit. Finally the dynamic pressure in the test section was measured by a pitot static tube located near the model and through the use of a Datametrix 1173 Electronic manometer. The output from this manometer was in inches of water.

The angle of attack of the model had to be adjusted from the outside of the test section during operation of the tunnel. To accomplish this an actuator was designed to mount on the top of the strut. The strut itself was high enough only to extend 30" into the test section so in order to bring the model exactly to the middle of the test section the actuator was designed to raise the model by 6". On the bottom of the actuator the necessary fixture was included to mount the actuator to the strut. The drive motor and rotational to linear motion converter was also located here. On top of this a strut was provided to carry the load of the wing. On top of this strut a small hinged

platform enabled the model to be mounted firmly yet the angle of attack to change. This hinged platform was connected by a steel rod to the linear motion drive. Also on this device an electronic inclinometer was included to enable the computer to both monitor the actual angle of attack of the model and set it to a pre-determined value. Fig. 3.6 is a photograph of the angle of attack actuator. The drive motor was connected to the relay box mentioned above through a special interfacing box that provided both the power and shielding of the expensive relay box from overloads due to unexpected events.

The surface pressure measurements on the model were made using a scanivalve system. The scanivalve system provides for selective connecting of one of 48 input ports to the output port. In this experiment the surface pressure taps were connected to the scanivalve by means of plastic tubing. Then the output port was connected to a Druck +- 1 psi pressure transducer. The scanivalve port selection was accomplished by the computer through the relay box and another special interfacing box. This interfacing box also contained the amplifier that made the reading of the strain gauge type transducer possible for the computer.

Thus with the instrumentation described above the

computer could execute entire experiments almost automatically. This reduced the time required for the experiments tremendously and also eliminated the possibility of human errors. The software neccessary to execute experiments automatically will be described in the section pertaining to each of the experiments.

3.3) Strain Gauge Force Measurements

The primary method used in this study for collection of data on the various aspect ratio wings was that of global force measurements via the strain gauge method. The reasons for this being the main method are twofold. First the speed at which a complete set of force data at a given set of angles of attack can be collected with this method is unsurpassed. This is due to the fact that the forces are directly measured through the deformation they cause in the strut. The second reason that this is the primary method for this investigation is the fact that this method provides all three components of force : lift, drag, and pitching moment at once; and furthermore, all the parts that contribute to each of these components are present. This means that both pressure forces and viscous forces are included.

Fig. 3.7 illustrates the setup used for all these experiments. The scanner selectively connects one of the 7 transducers to the DVM. The eight transducers consist of the three tunnel conditions transducers (temperature, free stream static pressure, and dynamic pressure) an angle of attack transducer (the inclinometer described earlier) and the force transducer (strain gauges) It should be noted that

there are three different force transducers of interest here (lift, drag, and pitching moment). The DVM feeds the current reading into the computer for immediate processing. The computer also can increase or decrease the angle of attack through the previously described interfacing boxes.

The flowchart for an entire experiment is given in Fig. 3.8. A computer program for this flowchart was written in BASIC to semiautomatically execute the entire experiment.

As can be seen from the flowchart, initially all the model and instrumentation data are read in. This includes calibration data for the angle of attack actuator. These calibration data were periodically checked to ensure the accuracy of the angle of attack readings. After this a tare reading is taken to account for the weight of the model and any residual voltages that may be present in the amplifier. This tare reading was assumed not to change significantly as angle of attack was changed since the center of gravity of the model was located exactly over the moment balance center. Also since the weight of the model doesn't change tare readings for lift do not change with angle of attack. In order to ensure that the drift in

residual voltages is not significant, several runs were made with no free stream velocity over a period of time. The results for lift, drag, and pitching moment throughout remained close to zero thus, justifiying the technique used here.

After the tare reading the computer would enter the angle of attack set mode. Here the current value of the angle of attack was compared with the desired value and adjustments made accordingly. Once the desired angle was reached the computer would once again measure the angle of attack with increased accuracy and then use the latest angle of attack measurement for the following datapoint. After this the outputs for tunnel conditions and all forces were measured 50 times each and averaged. Now the computer would perform the output activities (print, file) and finally return to select the next angle of attack. This cycle would continue until the preset range of angles of attack were completed. At this time the program would return to take a new set of tares and begin another experiment.

The voltages from the various transducers were converted into the respective physical value and then printed out and filed in that form.

3.5) The Momentum Deficit Method

The drag readings from the strain gauge method unfortunately were so small at Reynolds numbers below 100,000 that the accuracy was insufficient to give great confidence in these data. Thus, it was decided to perform a check of the drag data obtained with the strain gauge method by using the somewhat more sensitive momentum deficit method.

Here the velocity in the wake of the model is measured and then the momentum loss integrated to give the net drag force on the wing. This method is two-dimensional in the form it was used here. It would be possible to measure and integrate the momentum loss in the entire wake, however, this would take entirely too much time. Sweeps in the vertical direction would have to be made at multiple span-wise stations just to find the drag at one single angle of attack. Thus here only one sweep was performed in the vertical direction at a span-wise location of 0.2 b outboard from the centerline.

Two techniques were tested and eventually one selected for this part of the experiments. Traditionally the momentum deficit method was implemented through the use of a "wake rake". This is a series of pitot tubes located along a line. This rake

would be held into the wake and then measurements of the dynamic pressure at each pitot tube would give the local velocity in the wake. The "wake rake" available at the VPI Stabilty Tunnel however does not have a sufficient number of pitot tubes to provide good accuracy with the model used here. Thus a single pitot tube was used and moved at 5 mm increments through the wake. This technique however still provides discrete datapoints and allows only few points in the wake.

In order to alleviate these problems and to increase the speed of the experiments a new method was developed. With this method the single pitot tube is continuously moved through the wake of the wing and during the entire time momentum data are taken. Knowing the speed at which the pitot tube travels one can then integrate the momentum deficit. Calling f the force per unit span we can write:

$$f = \rho \int (U^2-U(z)^2)dz \qquad 3.1$$

Since this is again not suitable for computing the integral is approximated by a sum and we obtain

$$f = \rho\, a\, \Sigma\, (U^2-U(z)^2)\Delta t \qquad 3.2$$

where also the relation between speed of the pitot tube

a distance s and time t (ds=a*dt). The time intervals chosen were 0.005 seconds so that the maximum reading capacity of the DVM (200 readings per second) was fully utilized.

The drag readings found by the use of this method and the ones found by the discrete sampling method agreed exactly so that this method did not present any improvement in accuracy however it did give improvement as far as speed of the experiments is concerned and it could possibly improve results in very small wakes.

The general setup used for the implementation of the continuous sweep momentum deficit method is given in Fig. 3.9 and Fig. 3.10 contains the flowchart used for the automatic experiment execution program. The flowchart demonstrates the fact that most components i.e. angle of attack adjustment and tunnel conditions measurements could be directly adapted from the strain gauge program.

3.6) Pressure Measurement

Chordwise pressure measurements around the wing were done for two reasons. First another check of the strain gauge and momentum deficit tests could be obtained. Second, knowledge of the surface pressure distributions can give tremendous information about the flowfield. One can determine if and where regions of separated flow are located. In the case of this study the location and extent of the bubble can be determined. Also if there is turbulent separation at the trailing edge this can be observed.

There was some controversy over the effect of pressure taps themselves on the flow near the pressure tap area. Some researchers had not observed the hysteresis loop in stall using the surface pressure integration technique whereas it was observed using direct force measurement techniques. There had never been measurements using both techniques on the same model and in the same tunnel. Thus it was decided to investigate the effects of pressure taps on the flow over an airfoil at low Reynolds numbers by making surface pressure measurements with several taps not present.

The general setup used for these experiments is

shown in Fig. 3.11. Again most parts could be directly taken from the previous experiments (angle of attack actuation and tunnel data acqusition). The software to drive the scanivalve to the selected port had to be added. It was decided to only record pressures and then later to integrate these to obtain the forces on the wing. Fig. 3.12 shows the flowchart for this experiment execution program.

The pressure taps were staggered in the way shown in Fig. 3.13 to lessen the effect of upstream taps on the following ones. This was done after some preliminary flow visualization experiments had shown that behind even slight surface disturbances there is a turbulent wedge of approximately 5% semiangle. As the experiment progressed more and more pressure taps were opened until all 39 were open. In this configuration a full set of runs was made.

Since the pressure taps provide information only along one line on the airfoil this method gives only 2-D information. The pressure taps were located such that the ones at the leading edge were 0.255 b from the centerline. In order to make the flow more closely resemble the 2-D case the endplates were added for the pressure experiments. Then in order to find the total force on the wing it was assumed that the value at

0.255 b was the average for the entire wing. The results obtained from these experiments compare quite well with the results obtained from the strain gauge data thus it can be said that the endplates do cause the flow to be almost 2-D.

3.7) Flow Visualization Techniques

In order to gain some information about the state of the flow on the airfoil, and especially about 3-D effects, some flow visualization experiments were done. These consisted of 2 parts.

First an evaporative film technique was used. This technique provides information on the state of the boundary layer by visualizing mass transfer rates at the surface. These mass transfer rates are analogous to the momentum transfer rates and therefore can give information about the state of the boundary layer.

The technique was implemented by spraying a solution of naphthalene in trichloroethane on the wing. In order to avoid surface irregularities due to grains of naphthalene thrown on the surface a high quality spray gun had to be acquired. The wing was painted red for these experiments.

Since the solution is clear initially the wing appears dark. When the flow is started the evaporation process begins. Initially the trichloroethane, which is highly volatile, evaporates and the wing becomes white from the film of naphthalene. If there is an area where there is no surface flow (separation) the trichloroethane might linger for a rather long time,

long enough for even the naphthalene to sublimate in other areas of the wing. Of course in areas of high mass transfer the naphtalene sublimates and leaves the wing dark again.

This technique has the advantage of introducing almost no disturbances on the surface of the wing. The film of liquid and, after evaporation of the solvent, the film of naphthalene, do not increase surface roughness or introduce surface irregularities (bumps). Thus the character of the flow is not changed.

The disadvantage of the evaporative film technique however is the fact that the direction of the flow near the surface cannot be determined. A regime of separation on the airfoil will only show up as a line of extremely low mass tranfer rate. There is no indication of the extent of a laminar separation bubble if present. The picture at the wingtips is also incomplete since here significant span-wise flow is present.

To overcome the difficulties with the evaporative film technique another method of flow visualization was also used. Small oil droplets were placed on the surface of the wing. These droplets were colored black with graphite powder and the wing was painted bright yellow to increase contrast. These oil droplets will

follow the direction of the surface shear stress such that the local direction of the flow near the surface can be determined. Also the length of the distance that the droplet is pushed gives some indication of the magnitude of the shear stress and with this some indication of the character of the boundary layer.

Initially, it seems that this technique is more powerful then the evaporative film technique, but one has to keep in mind that the oil droplets are small "bumps" on the surface of the wing and therefore disturb the flow. These disturbances can cause, and in these experiments clearly did cause, a substantial change in boundary layer characteristics. Thus the oil droplets must be placed far apart and never behind each other. They must be staggered in a way similar to the one used for the pressure taps. Information can then only be extracted in a small portion of the wing. Figs. 3.14 a)and b) show examples of photograph taken using both techniques. Using them in conjunction made it possible to obtain a fairly accurate picture of the flowfield and the boundary layer characteristics.

Fig. 3.1 FX-63-137-ESM Airfoil contour

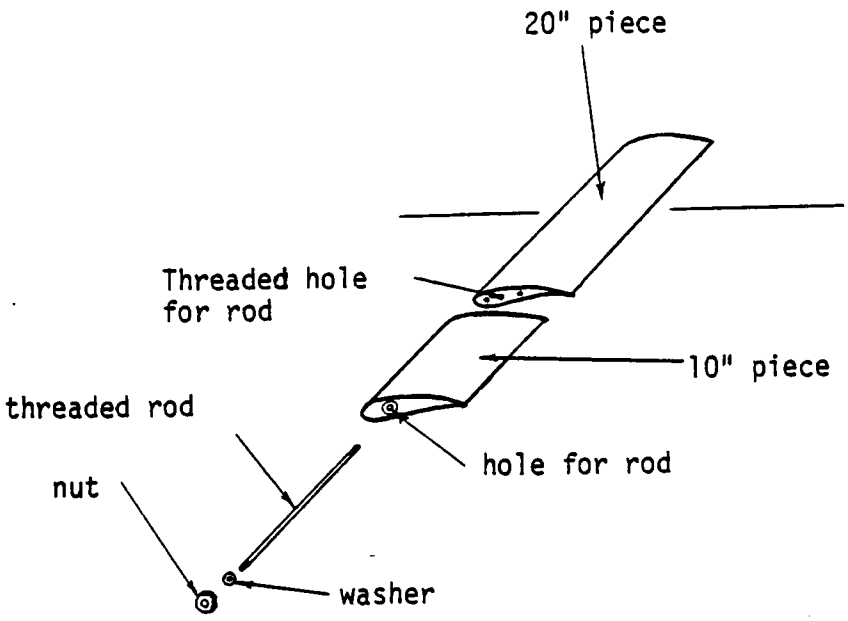

Fig. 3.2 Assembly method for AR=8 wing

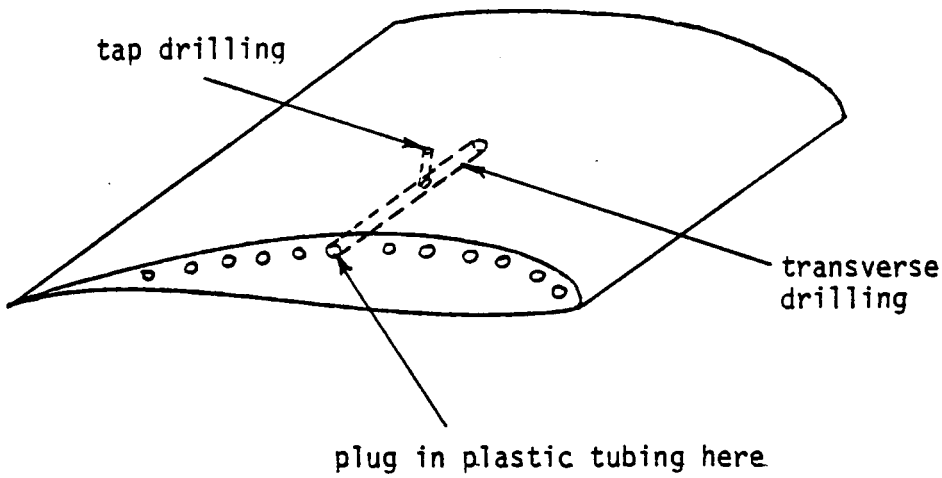

Fig. 3.3 Sketch of pressure taps

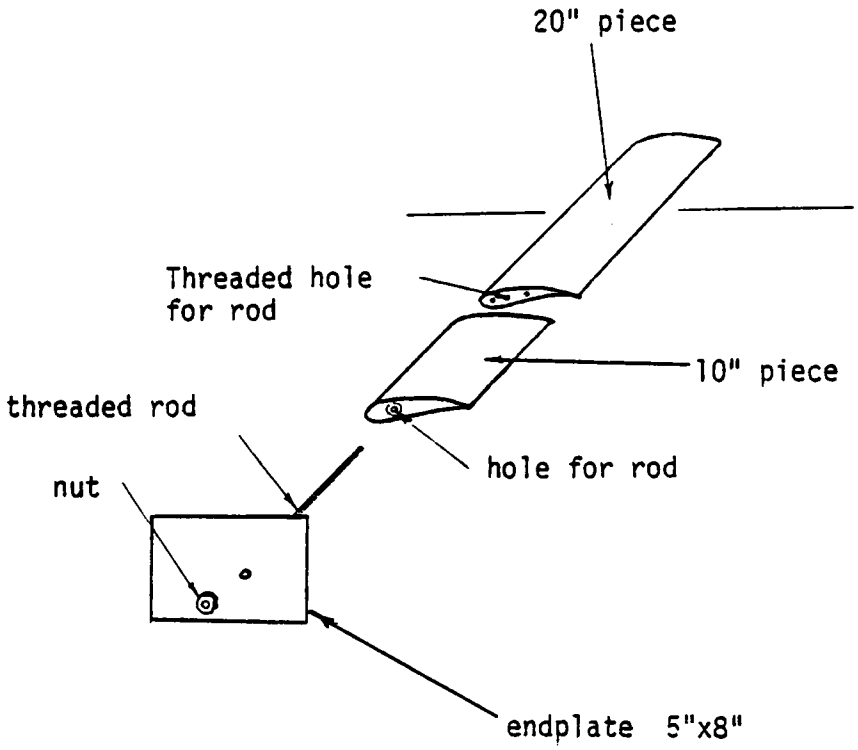

Fig. 3.4 Assembly method for AR=8 wing with endplates

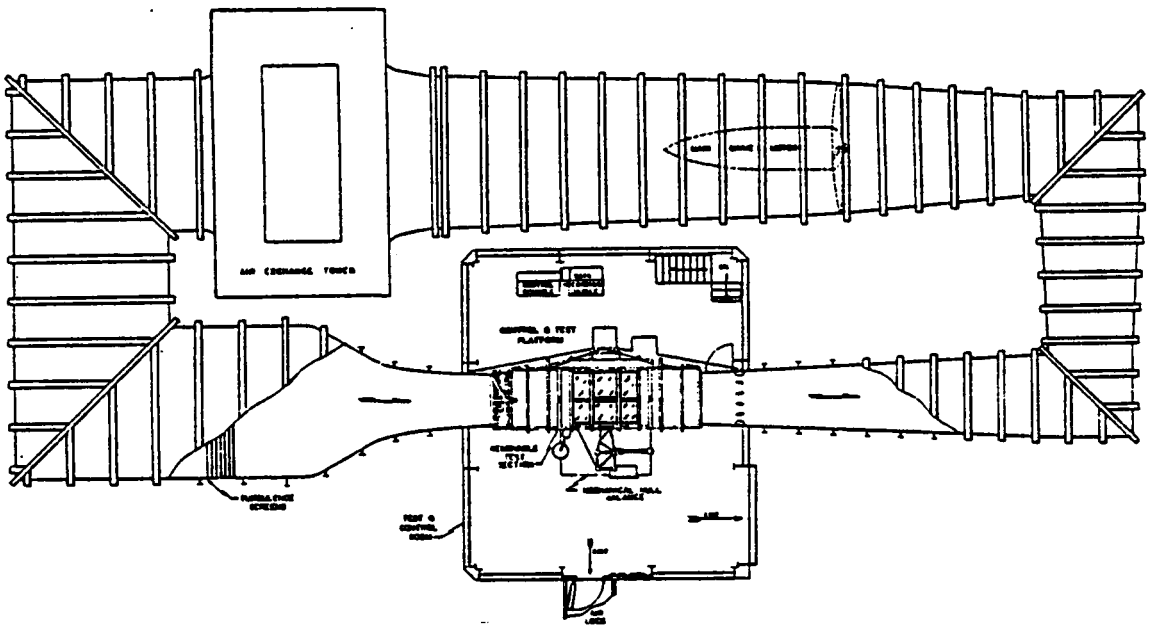

Fig. 3.5 Virginia Tech Stability Wind tunnel

Fig. 3.6 Wing mount and angle of attack actuator assembly

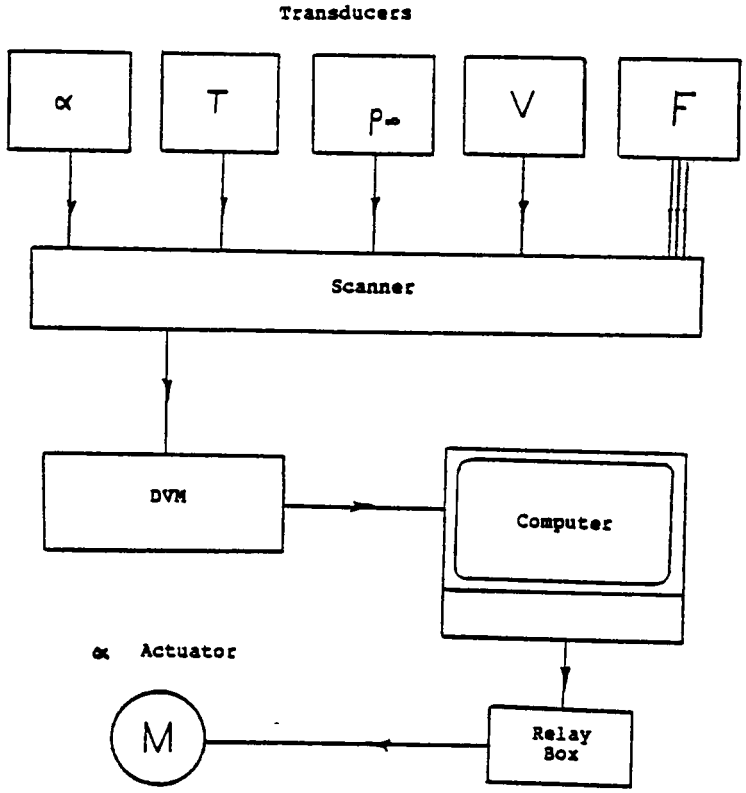

Fig. 3.7 Setup for Force Experiments

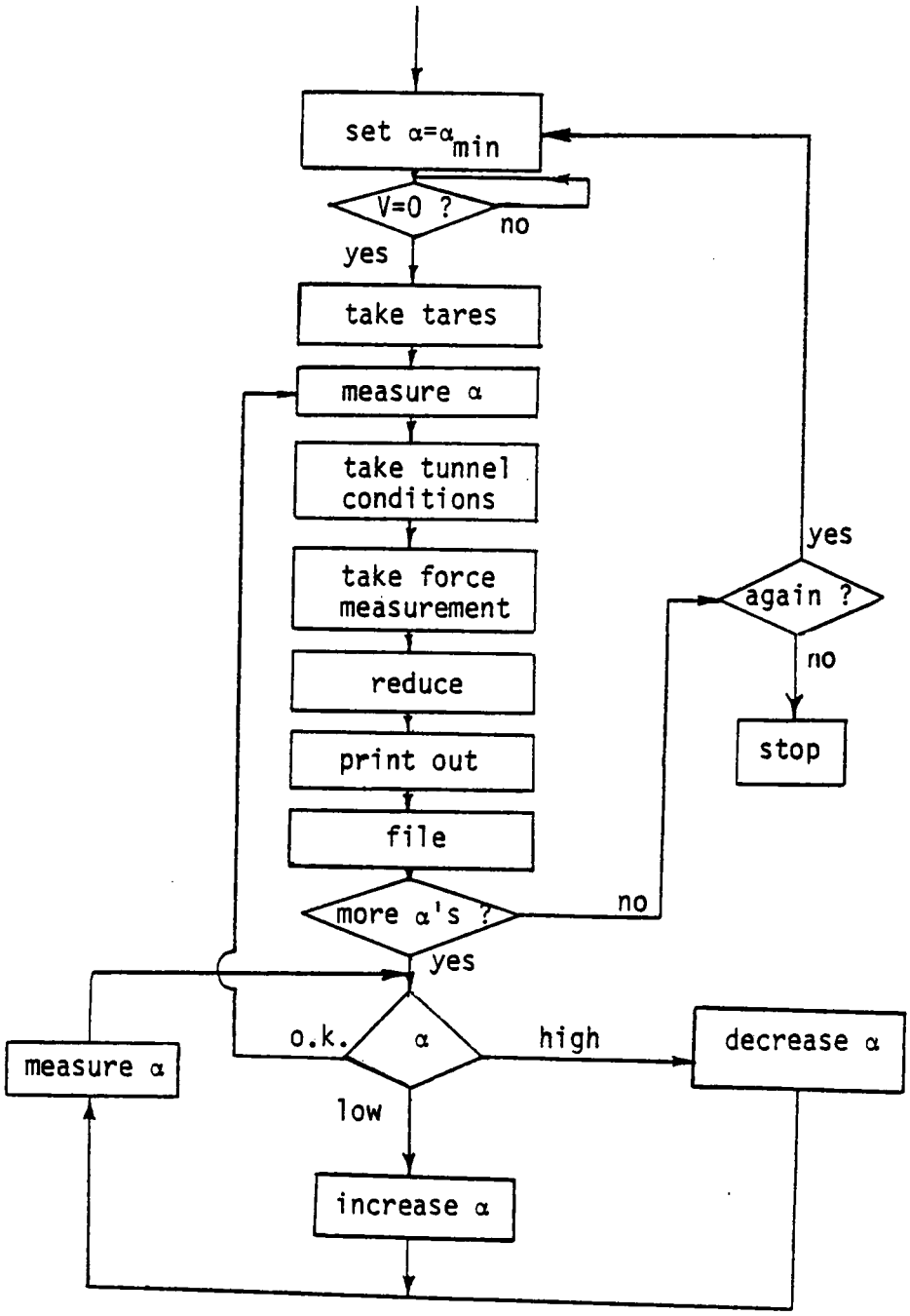

Fig. 3.8 Flowchart for force experiments

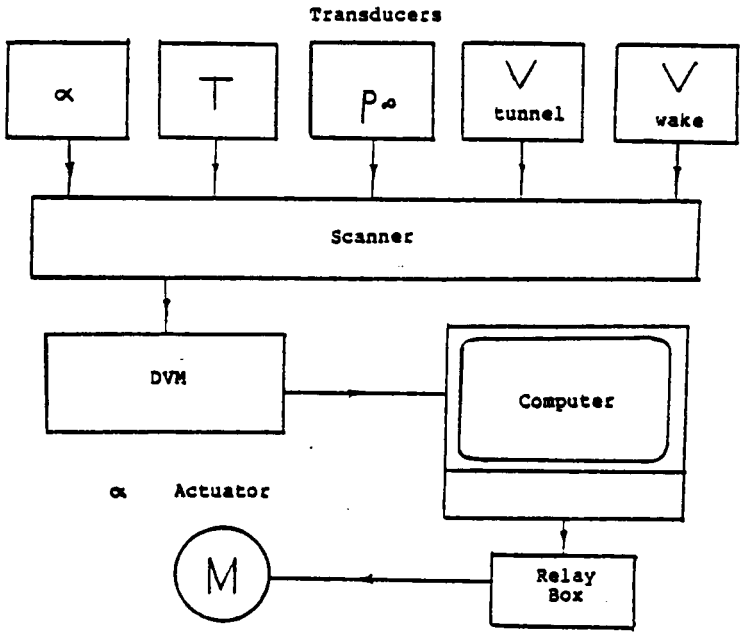

Fig. 3.9 Setup for momentum deficit experiments

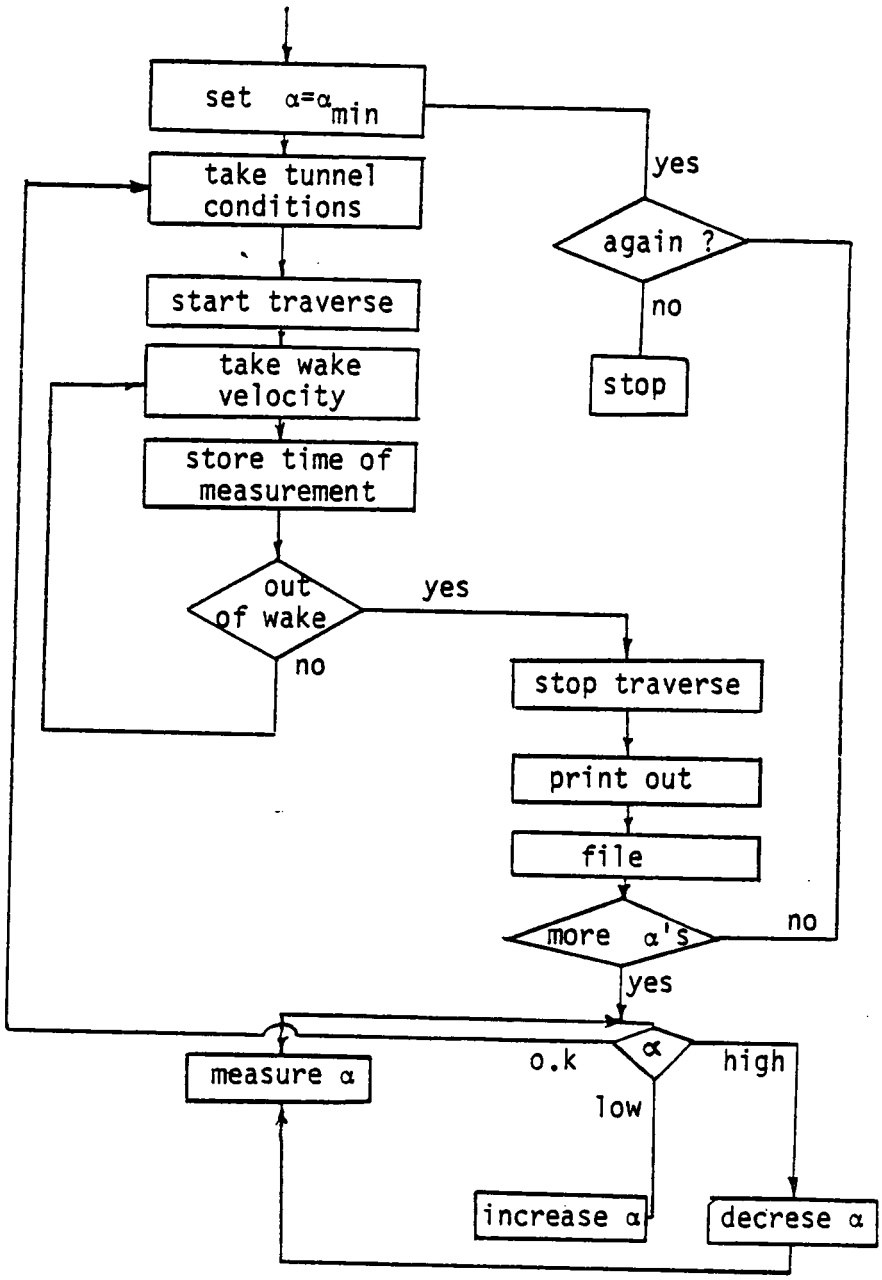

Fig. 3.10 Flowchart for momentum deficit experiments

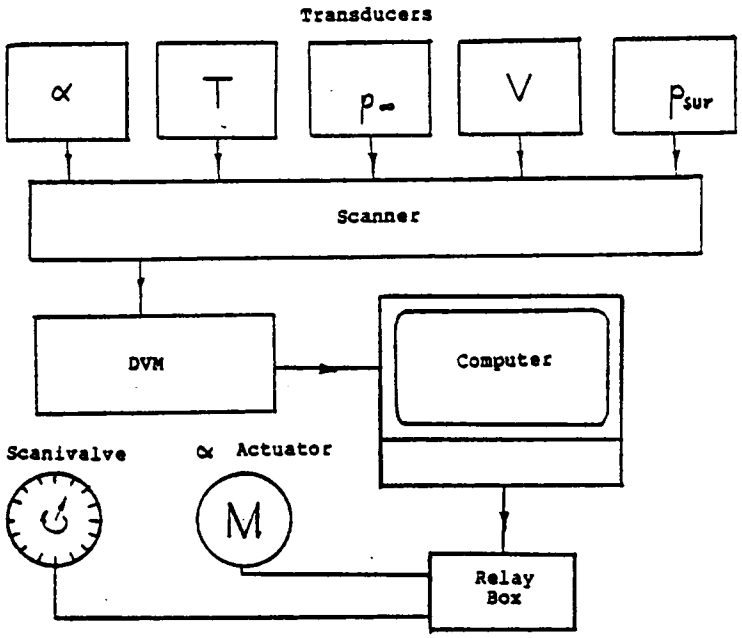

Fig. 3.11 Setup for surface pressure experiments

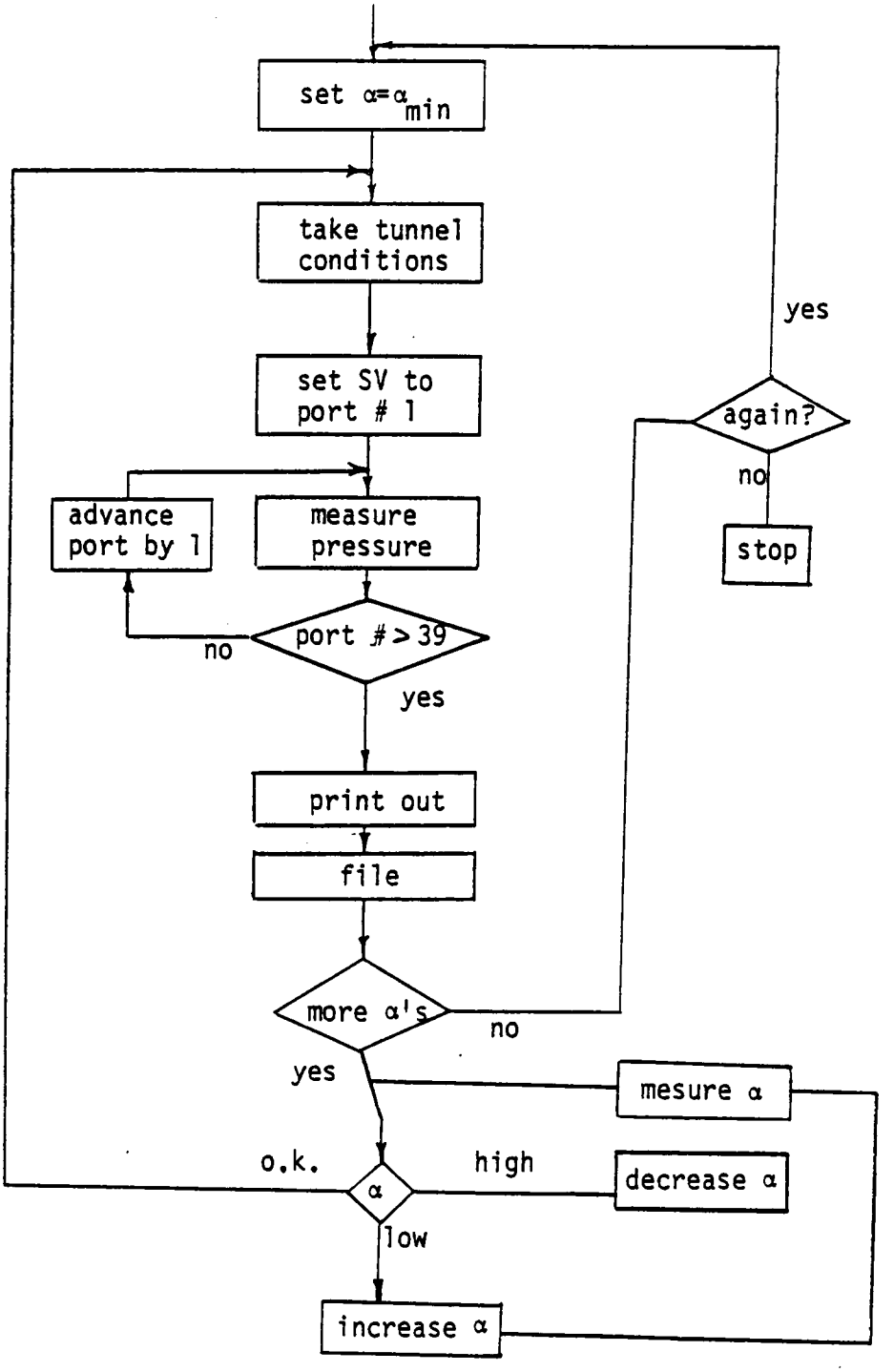

Fig. 3.12 Flowchart for surface pressure experiments

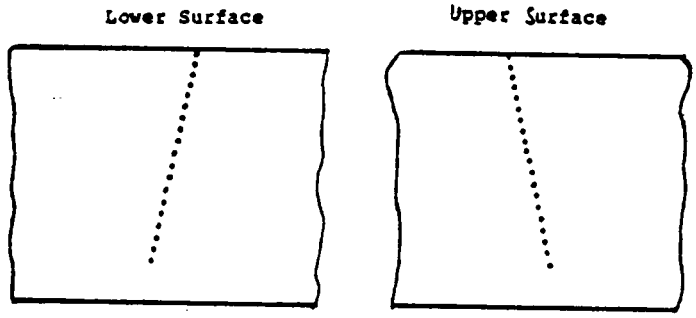

Fig. 3.13 Sketch on the arrangement of the pressure taps

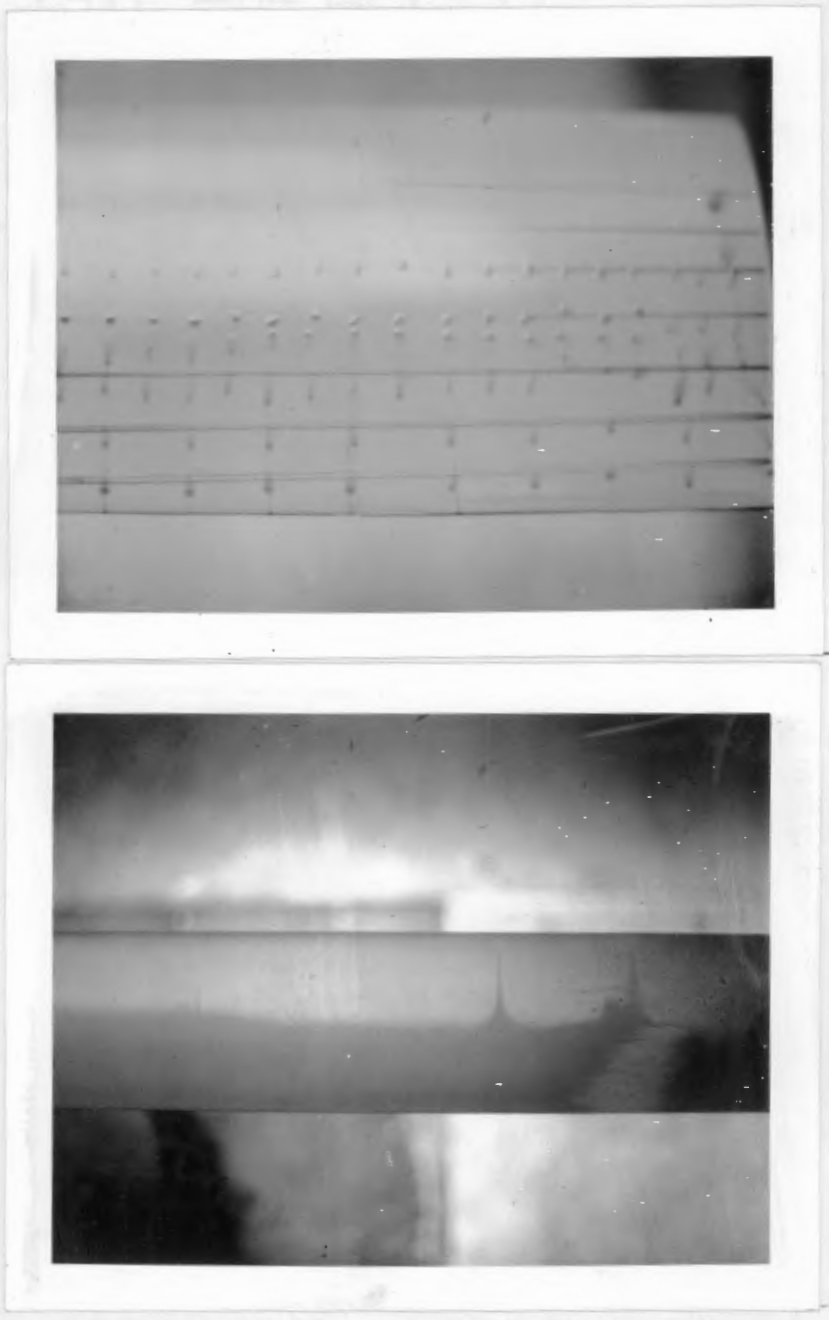

Fig. 3.14 Photographs to illustrate the two flow visualization techniques

4.) EXPRIMENTAL RESULTS AND DISCUSSION

Since the major measurement technique in this study was the force balance technique the results of these experiments will be discussed first. The experiments that were done with the strain gauge strut consisted of seven parts. Initially the four different aspect ratio cases of 10, 8, 6, and 4 were run. These four parts were devoted entirely to running the wings without endplates or pressure taps and under natural wind tunnel conditions; i.e. no noise or turbulence was introduced. The Reynolds number was varied in the range of 50,000 to 500,000.

The fifth part of the strain gauge experiments involved runs with the aspect ratio 8 wing with endplates. These experiments were conducted at the same time as the pressure measurements. It turned out that endplates influence the force data significantly, so that in order to compare the results of the strain gauge measurements with those of the integrated pressure experiments it was necessary to obtain strain gauge data with endplates too. Since these data approximate, at least as far as the lift is concerned, the infinite aspect ratio, they are quite relevant to our examination of aspect ratio effects. Also since

most previous experiments were conducted on 2-D models, data with endplates can give some comparison to results obtained in other facilities.

The sixth part of the experiments involved several runs with a thin flat plate of aspect ratio 6 and some experiments with a model that had a Clark-Y section. These made possible a comparison between the behavior of the FX-63-137-ESM section and the wings mentioned above. The flat plate experiments and some runs with the wing mounted upside down gave the necessary correction factors for strut influence on flow angle of attack. These corrections are necessary since the angle of attack was always measured relative to the surface of the earth. Therefore, it was necessary to obtain some idea of the angle of the flow in the test section relative to the earth.

The seventh part of the strain gauge experiments involved some preliminary tests regarding the influence of the wind tunnel environment (free stream turbulence and ambient noise) on the performance of the wing at low Reynolds numbers.

The discussion of the first four parts of the strain gauge experiments should be started by looking at the effects of Reynolds numbers at each of the four aspect ratios. Fig. 4.1 shows a plot of C_l versus angle

of attack for the aspect ratio 4 case and for Reynolds numbers of 70,000 , 100,000 , 200,000 , and 300,000. The first Reynolds number (70,000) shows a significantly different behavior from the other 3 cases. The lift curve for this case follows the others quite closely until an angle of attack of 3 degrees is reached. At this point it breaks away and the lift coefficient stays at about .75 until an angle of attack of 13 degrees is reached. Beyond an α of 13 degrees the lift curve flattens out. This behavior is clearly equivalent to that of a flat plate and the stalling pattern is that of "thin airfoil stall". In section 2 a detailed description of the flow phenomena occuring during a "thin airfoil stall" was discussed. Clearly the flow remains attached over a major portion of the airfoil until an angle of attack of about 5 degrees is reached and the laminar bubble is of the short type, since the lift values here agree almost exactly with those obtained at higher Reynolds numbers. At 5 degrees however, the laminar separation bubble bursts, and at this point the lift starts to deviate from the higher Reynolds number cases. Notably there is no hysteresis loop since the short bubble bursts into its long state early enough to be able to "unburst" to its short state

if the angle of attack is reduced back beyond 3 degrees. At a Reynolds number of 100,000, though the bubble bursts later at an angle of almost 15 degrees. As is to be expected, the value of the lift coefficient after the bubble has burst agrees quite closely with that of the Re=70,000 case since in both cases the flow is separated over the upper surface of the wing. The cause of the significant increase in the angle of attack at which the bubble bursts is the different condition of the boundary layer flow in general and an increase in the local Re throughout the surface.

The major difference seen at Re=100,000 is the fact that here a hysteresis loop is observed. This means that once the laminar separation bubble bursts it cannot "unburst" until the angle of attack is reduced below 12 degrees. At this point, the lift returns to its high value and one can assume that the laminar separation bubble has returned to its short state.

Fig 4.2 shows plots of the lift coefficient versus angle of attack at the Reynolds numbers of 73,000 , 75,000 and 80,000. Here the transition from what could be called the flat plate behavior to airfoil like behavior can be observed. While in the case of Re=73,000 the lift does not increase beyond the 0.85

level at a Reynolds number of 75,000 there is already evidence of a hysteresis loop, and the maximum lift coefficient reaches a value of about 1.2. This is a dramatic improvement in airfoil performance for a rather modest change in speed. A further increase of Re will yield a C_{lmax} of about 1.4.

If the Reynolds number is increased beyond a value of 100,000 to 200,000 two major changes in airfoil behavior occur. One is the change in the two angles at which transition from the one branch of the hysteresis loop to the other takes place. The bursting of the bubble occured at an incidence of 17 degrees for the case of Re=100,000 but at a Reynolds number of 200,000 this change takes place at an angle of attack of 23 degrees. This is a significant change in the stalling angle and a further improvement of airfoil performance relative to the Re=100,000 case. Also the value for the maximum lift coefficient increased significantly and reached 1.5 versus only 1.45.

The second change in the characteristics of the wing is due to the appearance of some trailing edge turbulent separation before laminar bubble bursting can take place. The manifestation of this separation of the turbulent boundary layer at the trailing edge is the

decrease in lift slope beginning at about 15 degrees and eventally even a loss of lift. Thus in this case C_{lmax} does not occur at the same angle as laminar separation but prior to full separation. In the case of Re=100,000 this rounding of the lift curve was not observed. Thus the stalling pattern there was that of "leading edge stall" without prior trailing edge separation, where at Re=200,000 the stall was a leading edge stall with some prior trailing edge separation. Some runs at Reynolds numbers between 100,000 and 200,000 showed that the first appearance of some trailing edge separation is at a Re of 130,000. At an Re= of about 150,000, (Fig. 4.3) the lift showed an slight decrease before falling abruptly due to leading edge separation. This implies that an increase in C_{lmax} with Reynolds number cannot be expected beyond a Reynolds number of 150,000 since here the trailing edge separation becomes the limiting factor before the leading edge separation can become effective. One can see in Fig. 4.1 that the value of C_{lmax} does not increase any more after a Re of 150,000 is reached. This was found to be true up to Re's of 300,000.

Fig. 4.4 shows the coefficient of drag versus angle of attack for an aspect ratio of 4 and Reynolds numbers of 70,000 , 100,000 , 200,000 , and 300,000.

This is a graph of the drag data corresponding to the lift data of Fig. 4.1. Clearly, the drag is highest for the lowest Reynolds number as is to be expected. The drag for the Re=100,000 case is at an intermediate level and the drag for the two higher Re cases is lowest. The latter two cases show only insignificant differences. This again suggests a fundamental difference in the flow characteristics at high and low Reynolds numbers. At the lower Re (70,000) the relative size of the laminar separation bubble is larger and correspondingly the effect it has on the aerodynamic loads is more pronounced. The laminar separation bubble is known to have a more significant effect on drag than on lift and therefore it can be seen that before stall the lift is close to the lift for higher Re but the drag is higher.

The drag at the higher angles of attack in the case of a Reynolds number of 70,000 and the lower branch of the hysteresis loop at the higher Reynolds number cases is quite close. This means, that once the wing is operating in a state corresponding to the lower branch of the hysteresis loop there is only a slight dependence of the forces on Reynolds number. This shows as was the case with the lift data that the state of

the flow on the lower branch of the hysteresis loop is equivalent to that at a Reynolds number of 70,000. Thus it can be said that at a Reynolds number of 70,000 the wing never reaches the upper branch of the hysteresis loop and always must remain on the lower branch.

In the cases of Re's of more then 150,000 the results obtained here indicate the onset of stall as a trailing edge stall and then before the trailing edge stall can become complete the laminar separation bubble bursts and then stall becomes a leading edge stall. The angles at which the transition from one branch of the hysteresis loop to the other takes place for the drag data is the same as for the lift data. This must indeed be so since the sudden changes in drag are due to the same phenomena on the wing that caused the sudden changes in lift.

As can be seen in Fig. 4.1 no hysteresis loop was observed for a Reynolds number of 350,000. From the general development of the stalling angle as a function of Reynolds number one could conclude that as the Reynolds number increases the laminar separation bubble becomes less prone to bursting and therefore there is more and more trailing edge stall before the bubble bursts. It could be assumed that when the laminar separation bubble has become stable enough so that the

trailing edge separation reaches it before it bursts, the hysteresis loop ceases to exist. This claim will be substantiated when the pressure experiments are discussed. However, some more detailed measurements are necessary to obtain more insight into mechanisms of reattachment before one could predict accurately the Reynolds number at which hysteresis ceases to exist.

The same effects that are present for the lift and drag data also can be seen for the pitching moment data. Fig.4.5 shows a plot of the pitching moment coefficient versus the angle of attack. In the case of a Reynolds number of 70,000 the pitching moment coefficient steadily increases throughout the range of angles of attack.

At a Reynolds number of 100,000, and for angles of attack below 15 degrees the pitching moment coefficient decreases. Then, a sudden increase in pitching moment occurs. This is due to the fact that as before the laminar separation bubble bursts at this angle of attack. This bursting causes the pressure over the upper surface and close to the leading edge to increase sharply (become less negative). The wing looses part of its tendency to pitch up and the pitching moment coefficients become less negative. At higher angles of

attack pitching moment coefficients increase with angle of attack as was the case for a Reynolds number of 70,000.

The effects of Reynolds number on the wings of other aspect ratio are all parallel. Basically low Reynolds numbers have the same effect at all aspect ratios in that below a certain value of Re the upper (as far as lift is concerned) branch of the hysteresis loop is never reached. An increase in Re will cause a certain amount of trailing edge stall to precede total separation at the leading edge.

Qualitatively the effects of Reynolds number are the same for all the aspect ratios tested . There are a few differences however if one takes a closer look. The Reynolds number at which the transition from flat plate behavior to airfoil like behavior takes place is one of the differences. Figs. 4.6 a) and b) show plots of lift coefficient versus angle of attack in the Re range were the change takes place for the aspect ratios of 6 and 10. For the aspect ratio case of 6 the transition occurs between a Reynolds number of 82,000 and 83,000. For the aspect ratio 10 case the change takes place at a Re between 90,000 and 95,000. In the case of AR=10 the transition did take place in a somewhat different manner. At the lower aspect ratios there was a clear

distinction between the two types of behavior, and the wing changed its behavior in an extremely narrow Re band. However, at AR=10 the behavior at 92,000 was somewhat erratic in that the lift would jump between the two branches for a small angle range.

Clearly, however the effect of increased aspect ratio is an increase in the Reynolds number at which transition from flat plate behavior to airfoil behavior takes place. This is not surprising since the smaller aspect ratio wings show more influence of the wingtip vortices on the flow.

The effect of the wingtip vortices is confined, even at low Reynolds numbers to a small region close to the wingtips. Some researchers have suggested that this was not the case (21) however flow visualization experiments done here clearly show that the effect of wingtip vortices is confined to a relatively small region at at the wingtip. Fig. 4.7 is a photograph of the condition of the boundary layer close to the wingtip. Clearly the flow pattern does not vary greatly in the span wise direction until a position close to the wingtip is reached. The presence of the wingtips however does influence the performance of the wing through the downwash induced at the wing due to the

trailing vortex sheet. This downwash tends to decrease the true angle of attack and this effect gets stronger towards the wingtips (see Fig. 2.11 for the downwash distribution). For the aspect ratio of 10 there is a large region in the middle of the wing where the downwash velocity is small and correspondingly the true angle of attack is almost equal to the geometric angle of attack. In this region the laminar separation bubble is less able to reattach and thus a higher Reynolds number is necessary to promote reattachment. At the lower aspect ratios the downwash is larger, and correspondingly the bubble can reattach easier. This explains the change in transition Reynolds number.

This effect can also be looked at in a different manner. Fig. 4.8 shows a plot of C_l versus α for a Reynolds number of 100,000 and the two aspect ratios of 4 and 10. The angle at which abrupt stall occurs is clearly lower for the aspect ratio 10 case. In the previous section it was shown that a decrease in Re will yield a decrease in this abrupt stalling angle. If we imagine what a decrease in Reynolds number will cause to happen to the plot in Fig. 4.8 it becomes clear that leading edge stall will always first occur on the aspect ratio 10 case. On the other hand, this decrease in stalling angle cannot continue indefinitely

and it will stop when the critical Reynolds number for thin airfoil behavior is reached. The aspect ratio 10 wing will reach this stage first.

This leads to the discussion of the main subject of this text, which is the effect of aspect ratio at low Reynolds numbers. Fig. 4.8 is a good example of the aspect ratio effect. Initially, it should be said that there seems to be no effect of aspect ratio on the type of stall that does occur at this Reynolds number. In this case the stall can be classified as a pure leading edge stall for both aspect ratios.

There is a change in lift slope as is to be expected from the predictions of lifting line theory. In Fig. 4.9 the the lift curve of the AR=4 case is adjusted to aspect ratio of 10 by changing the lift slope to the value that the theoretical predictions of section 2 give. It can be seen now that the slope of the lift curve for the AR=4 (corrected) case agrees quite well with that of the AR=10 case. Thus, the predictions of the lifting line theory as far as changes of lift slope are concerned are found to be very accurate. However, there is an additional effect that is not predicted by the theory and this is a shift in the zero lift angle. According to the lifting line

theory there should be only a change of the lift slope, i.e. the lines in Fig. 4.8 should pivot around the point where they intersect the angle of attack axis. The fact that there is a change in the zero lift angle of attack suggests that there is a change in the effective camber of the airfoil. Fig. 4.10 shows that this effect is present at higher Reynolds numbers (300,000) too. However it is known that it is not present at higher Reynolds numbers (Re>2,000,000). Unfortunately this wing could not be run at speeds that high because of tunnel limitations and structural strength of the model.

The upper surface of the airfoil definitely has attached flow at low angles of attack so that the effective change in camber must stem from something on the lower surface. If we look at Fig. 3.1 (airfoil contour) we can see that separation on the lower surface could produce the same effect as a change in camber, where the farther ahead the separation point moves the less effective camber is present. This means that at the lower aspect ratios where the zero lift angle of attack is lower the amount of separated flow on the lower surface must be less. This could possibly be due to the tip region constituting a larger portion of the entire wing but in order to understand this

phenomenon better studies will have to be done examining the flow on the lower surface. Traditionally this is rarely done since the point of interest and usually the more critical point for aircraft performance is the stalling angle.

It should be pointed out here that the zero lift angle for this airfoil has been subject to some debate since almost every facility that has performed tests on this airfoil has obtained different results. Fig. 4.11 a) and b) shows the data obtained for this airfoil in two different wind tunnels with the same model, and clearly there is a discrepancy in zero lift angle of attack. Also other data obtained by Mueller (22) show a different zero lift angle. This somewhat puzzling question has not been resolved yet. The studies done in conjunction with this work show clearly that a reduction in aspect ratio will decrease the zero lift angle of attack.

Figs. 4.12 , 4.13 , 4.14 , 4.15 and 4.16 show a complete set of lift curves at the four Reynolds numbers of 100,000 , 150,000 , 200,000 , 250,000 and 300,000. The effects of aspect ratio on the lift slope and the zero lift angle are as described earlier. In order to clarify the effect of aspect ratio on the

extent of the hysteresis loop Figs. 4.17 and 4.18 were prepared. Fig. 4.17 shows the extent of the hysteresis loop for the two aspect ratios of 4 and 10. No clear trend can be seen as far as changes due to aspect ratio are concerned. In both cases the angle for leading edge stall and the angle for return from the lower branch of the hysteresis loop to the upper branch increase with Reynolds number. It seems that the appearance of thin airfoil stall cannot be attributed to the meeting of the L.E. stall and return angle lines as might be expected. The same holds for the point where the hysteresis loop stops to exist.

Fig. 4.18 shows the dependence of the leading edge stalling angle and the return angle on aspect ratio.

Fig. 4.19 gives a more detailed view of the range of Reynolds numbers where hysteresis stops due to the appearance of thin airfoil stall. It seems that the angle of attack for leading edge stall suddenly drops sharply close to the transition Reynolds number but measurements between the Reynolds number of 73,000 and 75,000 showed that the lift jumps randomly between what seems to be the upper and lower branches such that the behavior in this region could be termed unstable.

Finally, Fig. 4.20 shows the dependence of the transtion Reynolds number from leading edge stall to

thin airfoil stall.

The maximum lift coefficient for the wings at the four different aspect ratios is depicted in Fig. 4.21 in addition to data for the NACA 0009 airfoil. Clearly this airfoil has much better performance at lower Reynolds numbers. The maximum lift depends strongly on the Reynolds number for Re<150,000 since here leading edge stall is the limiting factor. After this trailing edge stall becomes the limiting factor and the dependence becomes much weaker.

The level of lift on the lower branch of the hysteresis loop is influenced by the aspect ratio. The prediction of this influence by theoretical means as was done to some extent for the straight portion of the lift curve is not possible since the lifting line theory cannot in any way be applied to the fully separated flow that exists here. The lift on the lower branch generally decreases with aspect ratio. It seems that the decrease in aspect ratio pivots the entire lift curve including the hysteresis loop around the pivoting point. Fig. 4.9 shows the result of applying the lifting line theory as described in section 2 to the plot in Fig. 4.8. In addition to the change in lift slope the fact was used that the zero lift angle of

attack changes too (the slope of the curves was corrected to infinite aspect ratio and they were pivoted as a whole around the pivoting point of α=-.5 degrees and Cl=.42). The prediction of the level of the lift on the lower branch of the hysteresis loop as well as in the portion where trailing edge stall is present is not in complete agreement with experiment as expected since the theory is not applicable here.

For the Reynolds number of 70,000 the lifting line theory fails as well. Here again the flow is separated and therefore an inviscid theory naturally can not be applied. Fig. 4.22 shows the lift curves for the four aspect ratios at a Reynolds number of 70,000. All cases display the same overall characteristics.

The effect of aspect ratio on wing drag can be said to be parallel to the effects on lift. At angles of attack above the pivoting point the drag is clearly higher for the lower aspect ratios. This can be seen in Fig. 4.23 which is a plot of drag coefficient versus angle of attack at a Reynolds number of 200,000 and for all four different aspect ratio cases.

The transition angles for the change from one branch of the hysteresis loop to the other are the same as those for the lift were however the upper branch of the drag curve corresponds to the lower branch of the

lift curve as here the flow is separated. The strong increase in drag as leading edge stall takes place is easily explained by the collapse of the suction in the leading edge region which provides some forward force to cancel the rearward pressure forces on the rear of the airfoil. The collapse of this leading edge suction is due to the bursting of the laminar separation bubble. Evidence of this will be shown later in the discussion of the pressure experiments.

The lift value for conditions of a burst bubble showed some effect due to the aspect ratio. This effect can be seen for the drag as well. A lower aspect ratio will yield a higher drag in the separated condition.

During operation with attached flow and when the angle of attack is greater than the pivoting angle of attack as was said before the drag increases with decreasing aspect ratio. This is correctly predicted by the lifting line theory. Fig. 4.24 shows a drag coefficient plot for the two aspect ratios of 4 and 10 corrected to reflect only the profile drag (the induced drag as predicted by lifting line theory subtracted out). The predictions of the theory are seen to be not as good as in the lift case but still quite adequate as long as one stays above zero angle of attack. Returning

to Fig. 4.23 we can see that below zero angle of attack the character of the curve changes (i.e. a drag bucket is very pronounced in one case and not in another) with aspect ratio. These changes are due to differences in profile drag and therefore the lifting line theory is unable to collapse all curves into one here. The theory predicts that the drag always increases with decrasing aspect ratio except at the zero lift point where it is equal to the profile drag. The fact that there is a shift of the zero lift angle complicated the issue here somewhat and as can be seen the drag for an aspect ratio of 4 is lower at negative angles of attack than at aspect ratio 10. This is surprising since here the lift of the aspect ratio 4 wing is also higher and therefore the induced drag is higher. The increased drag for higher aspect ratios that is observed at the low Reynolds numbers and with this airfoil shape must then be the result of some phenomenon occuring on the lower surface.

It is interesting to look at the drag data obtained at a lower Reynolds number of 100,000. Fig. 4.25 shows the drag coefficient for all four cases of aspect ratio at this Reynolds number. The drag is found

to be higher fo the lower aspect ratio as is expected. Unfortunately, at this Reynolds number there is already some scatter in the data such that the curves drawn here must be used with caution. Still there is hysteresis as was present in lift and the transition angles agree.

Fig. 4.26 shows a graph of the pitching moment coefficient versus angle of attack at a Reynolds number of 200,000 and for all four aspect ratio cases. At negative angles of attack the slope of all four of the pitching moment curves is negative as is the value of the coefficients is negative too. Above this angle a hysteresis loop is visible in all four cases. The angles of transition from one branch of the loop to the other are the same as in the case of lift and drag data at this Re. This is again to be expected since the transition is a manifestation of the same phenomenon (bursting of the bubble or reattachment). The same kind of data for a Reynolds number of 100,000 is presented in Fig. 4.27. The picture that presents itself here is quite similar to that seen for the previous Reynolds number except that here the most negative pitching moment is observed for the lowest aspect ratio case and the least negative pitching moment coefficient is observed for the highest aspect

ratio. This is the exact opposite trend of the higher Reynolds number case.

Fig. 4.28 shows the effect of aspect ratio on drag at a Reynolds number of 250,000. Drag behavior is essentially identical at this Reynolds number to what was observed at a Re of 200,000 as far as aspect ratio effects are concerned. It should be noted that the drag curves corresponding to low angles of attack and to the attached flow branch of the hysteresis loop look quite similar to the classical drag curves observed on "normal" airfoils at high Reynolds numbers.

The moment data for Re=250,000 are presented in Fig. 4.29. Again the aspect ratio effects are identical to those observed at the Re of 200,000. The lowest aspect ratio case has the least negative pitching moment coefficients.

Figs. 4.30 and 4.31 are plots of the drag and pitching moment data obtained at a Reynolds number of 300,000. There are no significant differences between the effects of aspect ratio at Re=300,000 and the lower cases discussed previously.

The above discussion treated the first four parts of the strain gauge strut experiments which was done mainly to find the aspect ratio effects. The fifth part

of these strain gauge experiments consisted of several runs using the wing with endplates. This was done to approximate a purely 2-D flow. Fig. 4.32 shows a lift curve plot for the same wing with and without endplates. The change in lift slope due to the endplates is evident and the theoretical value of 2π is almost reached. The zero lift angle of attack for the case with endplates is -4 degrees. For the aspect ratio 4 case it was as low as -9.5 degrees. This means that the change of the flow from nearly infinite aspect ratio to aspect ratio 4 causes a change of the zero lift angle by 5.5 degrees which is quite significant. For the case with endplates the entire curve including the hysteresis loop seems to be rotated around a pivoting point of $\alpha=0$ degrees and $C_l=.60$. This identical effect was observed when the aspect ratio effects were examined previously. Thus the experiments with the endplates confirm the validity and accuracy of the lifting line theory at low Reynolds numbers except that a shift in the zero lift angle must be incorporated for this airfoil.

Fig. 4.33 shows a drag plot for the previous two cases. The additional drag due to friction on the endplates shows up quite clearly here. Thus it would not be advantageous for aircraft to use endplates to

decrease induced drag since the drag caused by the endplates by far overpowers the induced drag.

The sixth part of the strain gauge experiments was concerned with the measurement of the performance of a flat plate and a different airfoil (Clark Y). The lift data obtained for these cases are plotted in Fig. 4.34. The flat plate behavior clearly indicates thin airfoil stall and thus is equvalent to what was seen on the FX-63-137-ESM at Reynolds numbers of about 70,000. This confirms the fact that there is completely separated flow over the entire upper surface of the airfoil at these Reynolds numbers. The Clark Y shows a very small hysteresis loop and a maximum lift coefficient of about 1. Therefore clearly the FX-63-137-ESM has a tremendous advantage over the Clark Y as far as aerodynamic performance is concerned. Unfortunately, the complicated shape is much more difficult to manufacture than the flat-bottom Clark Y.

The flat plate does show a zero lift angle of attack of 0 degrees as expected. The original wing was mounted upside down to determine the effect of the strut and shroud and if the flow has a non zero angle relative to the surface of the earth. This gave the correction factor of 2.5 degrees which was then applied

across the board.

The seventh and final part of the strain gauge experiments was concerned with some preliminary testing of turbulence and noise effects on airfoil performance. Noise was introduced by placing a speaker behind the wing on the tunnel floor and to increase turbulence 1 inch strips of material were fixed to the anti turbulence screen at 1 foot intervals. The noise intensity was measured at 110 db and the turbulence intensity at .27 % at the wing. Figs. 4.35 and 4.36 show the effects of noise and turbulence. The upper branch of the hysteresis loop and the linear portion of the lift curve are not altered significantly however the lower branch and the return angle are strongly affected.

It became clear in the beginning of the experiments that the measurements of drag at low Reynolds numbers would be difficult because of the forces involved being extremely low. This is especially the case for lower aspect ratios. Thus, it was necessary to validate the drag data obtained by the strain gauge method using some other more sensitive technique. The technique chosen was the momentum deficit method. Fig. 4.37 shows drag curves for data obtained through both methods. Obviously there is very

good agreement between the two as long as there is no significant flow separation. When flow separation does occur however usually drag forces are high enough to allow good confidence in the data obtained by the strain gauge method. In fact, due to the limitations of the momentum deficit method that were discussed earlier the strain gauge data are more relevant here.

In the range of angles of attack where no significant flow separation is present, the momentum deficit data are more reliable but, agree with the strain gauge data and thus the strain gauge data can be used with good confidence.

It should be noted that the strain gauge data have been corrected by use of the induced drag formulas given in section 2 since the momentum deficit data are 2-D. The overprediction of drag by the momentum deficit method at angles of attack where separation exists is due to the fact that here significant amounts of angular momentum are present in the wake. This angular momentum is undetected by the pitot static tube and therefore the momentum transfer to the model is taken to be larger than it really is.

The final series of experiments was concerned with pressure measurements around the airfoil. Since the

pressure taps were located only on one span-wise location of the wing, data in this case are essentially 2-D and aspect ratio effects could not be observed. In order to make sure that the flow is as two dimensional as possible these experiments were run with the endplates in place.

Initially, the effects that pressure taps have on other pressure taps and the flow on the wing in general were observed. To do this, the pressure taps were opened in groups of 8 starting at the rear of the upper surface.

Fig. 4.38 shows the effect of opening the 8 holes in the middle section of the airfoil on the measurements obtained at the rear of the wing. Initially, the wing was run with only 8 holes open in the rear. Then 8 more holes were opened and the wing was run at the same angle of attack. Obviously at this angle of attack there is absolutely no effect on pressure measurements due to the presence of pressure taps. Fig. 4.39 shows the same type of comparison only this time it is done between 16 taps open and all taps open. Again there is absolutely no effect due to the presence of the pressure taps. Fig. 4.40 is the equivalent of Fig. 4.39 except for a higher angle of attack. The fact that the angle of attack is increasing

implies that the wing is operating with a laminar separation bubble on the upper branch of the hysteresis loop. Again no significant effect due to the pressure taps is observed. The location of the laminar separation bubble is clearly visible at .2c. Reattachment is seen to be at approximately .27c.

Fig. 4.41 shows the pressure data obtained for the cases of 8 holes open and 16 holes open at an angle of attack of 12 degrees and corresponding to the upper branch of the hysteresis loop. In addition to the fact that the pressure taps do not have any effect, again the laminar separation bubble can be seen quite clearly. Fig. 4.42 shows a flow visualization photograph taken under the same conditions as in Fig. 4.41. The location of the laminar separation line is seen to correspond quite closely to that point on the pressure plot where the pressure distribution flattens out.

Fig. 4.43 is a plot of all three cases (8,16, and all taps open) for an angle of attack of 14 degrees and corresponding to the upper branch of the hysteresis loop. Again it seems that the pressure taps have no significant influence on the flow. Fig. 4.44 shows the case of all holes open at an angle of attack of 14

degrees but this time one of the lines corresponds to the upper branch of the hysteresis loop and the other corresponds to the lower. In spite of the fact that the force data obtained through the strain gauge method show a clear distinction between the two cases the pressure data do not show this distinction. It seems that as far as the pressure data are concerned there is only a very small difference between the upper and lower branches of the hysteresis loop. Fig. 4.45 shows a plot of lift versus angle of attack for the data obtained through strain gauge measurements and the ones obtained through integration of the pressures around the airfoil. Even though the conditions are exactly equal and in fact the two runs were done back to back the results are somewhat different the main difference being a different return angle.

Figs. 4.46 and 4.47 give some insight into why there is such a difference. In Fig. 4.46 we see the condition of the flow as fully separated (the pressure plot is flat behind .2c) and no tap effects are present. Fig. 4.47 shows the pressures obtained with the three tap configurations at an angle of attack of 12 degrees and operating on the lower branch of the hysteresis loop. The angle of 12 degrees is very close to the return angle. This fact causes there to be a

difference between the pressure data and the strain gauge data. In the case where 8 holes are open clearly the rear portion of the wing has separated flow. However when the next 8 holes are opened the flow separation disappears. This means that the taps in the region of the laminar separation bubble influence the flow in such a way that pressure measurements become completely incorrect. Flow visualization pictures show that the separated flow that should be present when the wing is operating on the lower branch of the hysteresis loop is still present over most of the wing and in fact the pressure taps have no global effect on the boundary layer (Fig. 4.48). Also a comparison of strain gauge data obtained with the pressure taps closed and open shows no effect at all. The only inaccurate data then are the ones obtained on the lower branch of the hysteresis loop with pressure taps in the forward portion of the airfoil.

Fig. 4.49 shows a pressure plot at a different Re to demonstrate the effect on the bubble. Clearly here the bubble is much longer and situated more aft on the airfoil.

It is appropriate to describe some of the flow visualization results obtained by the oil droplet

method here. Up to now the effects of the laminar separation bubble have been described in detail but there has been no proof that there is laminar separation and reattachement. Fig. 4.50 shows an oil droplet picture at an angle of attack of 10 degrees and a Reynolds number of 200,000. It can be seen that the droplets in the middle (0.5 c) of the airfoil are pushed forward. This proves that in this region there is backflow. The photograph in Fig. 4.51 shows an evaporative film photograph at the angle of attack and Reynolds number. Here the same region where in the previous figure the oil droplets were pushed forward has remained dark due to the fact that here the solvent has not evaporated yet when the naphthaline has already vanished in the turbulent boundary layer region.

In the oilflow picture one can also see the effects of the turbulent boundary layer since here the high shear stress at the wall has pushed the oil droplets very far back.

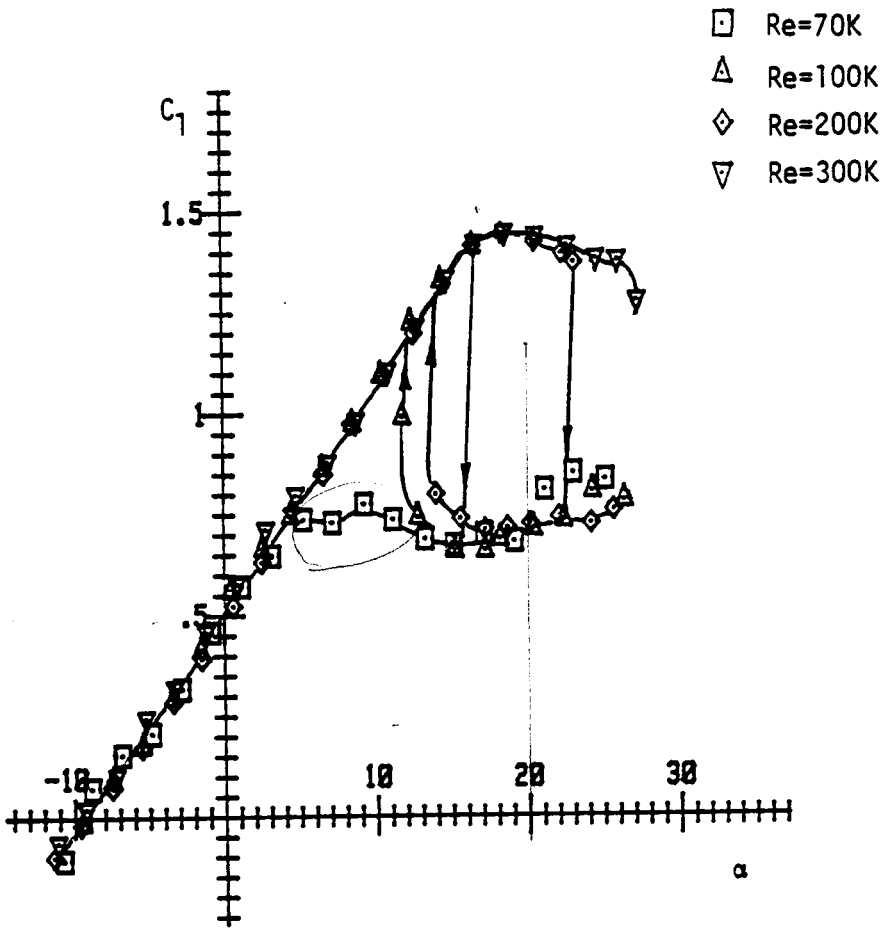

Fig. 4.1 $C_l \rightarrow \alpha$ for AR=4

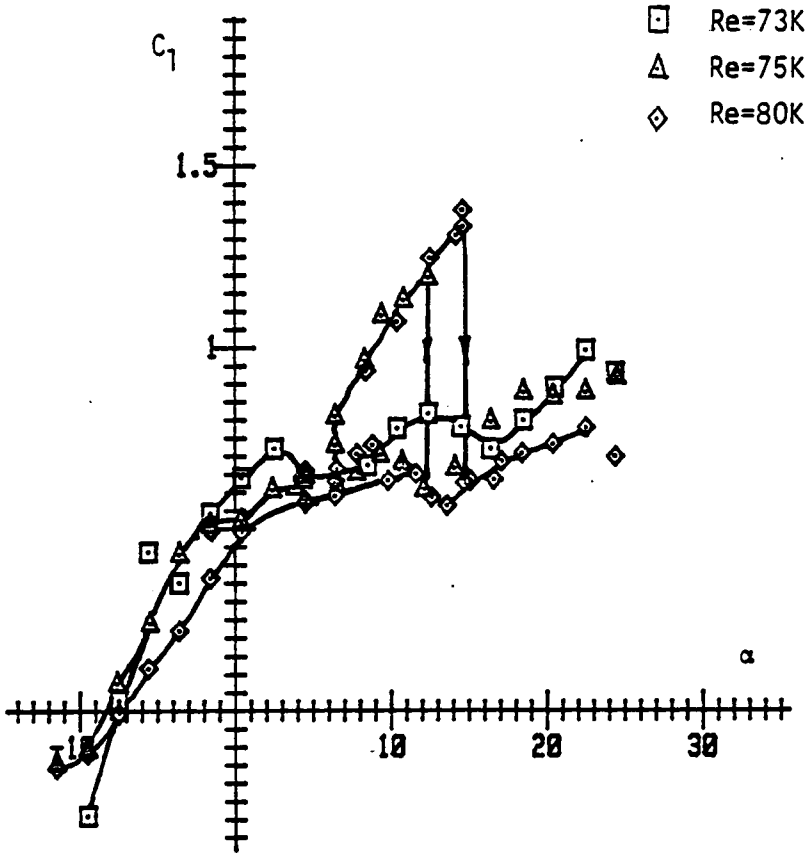

Fig. 4.2 $C_l \rightarrow \alpha$ for AR=4

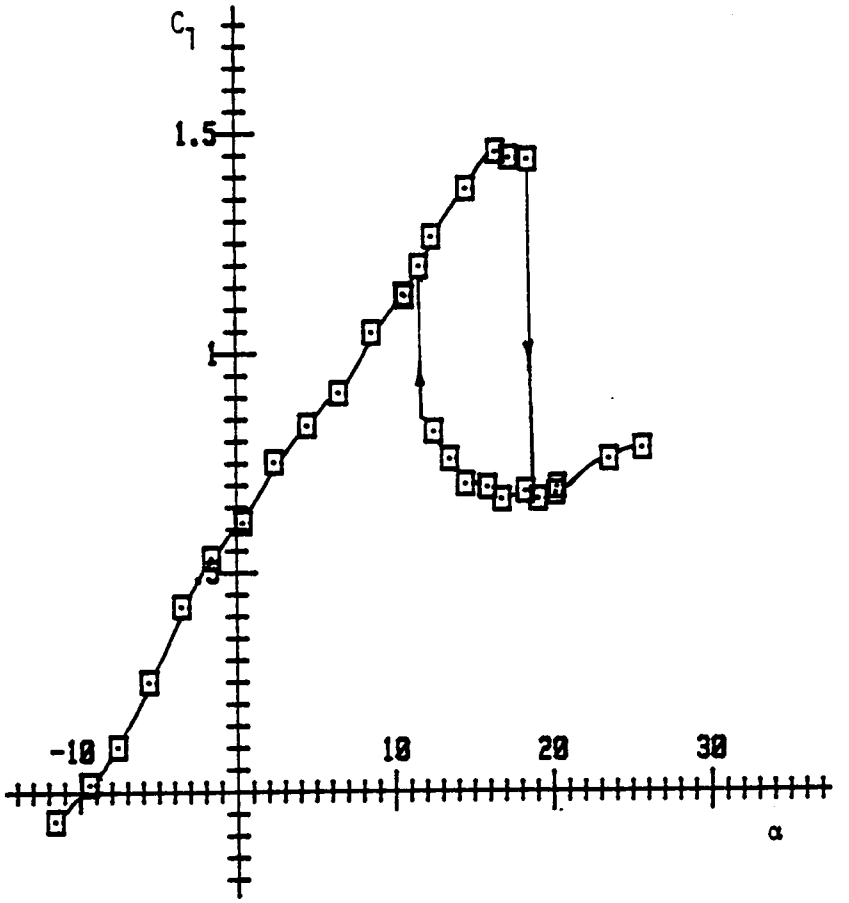

Fig. 4.3 $C_l \rightarrow \alpha$ for Re=150K and AR=4

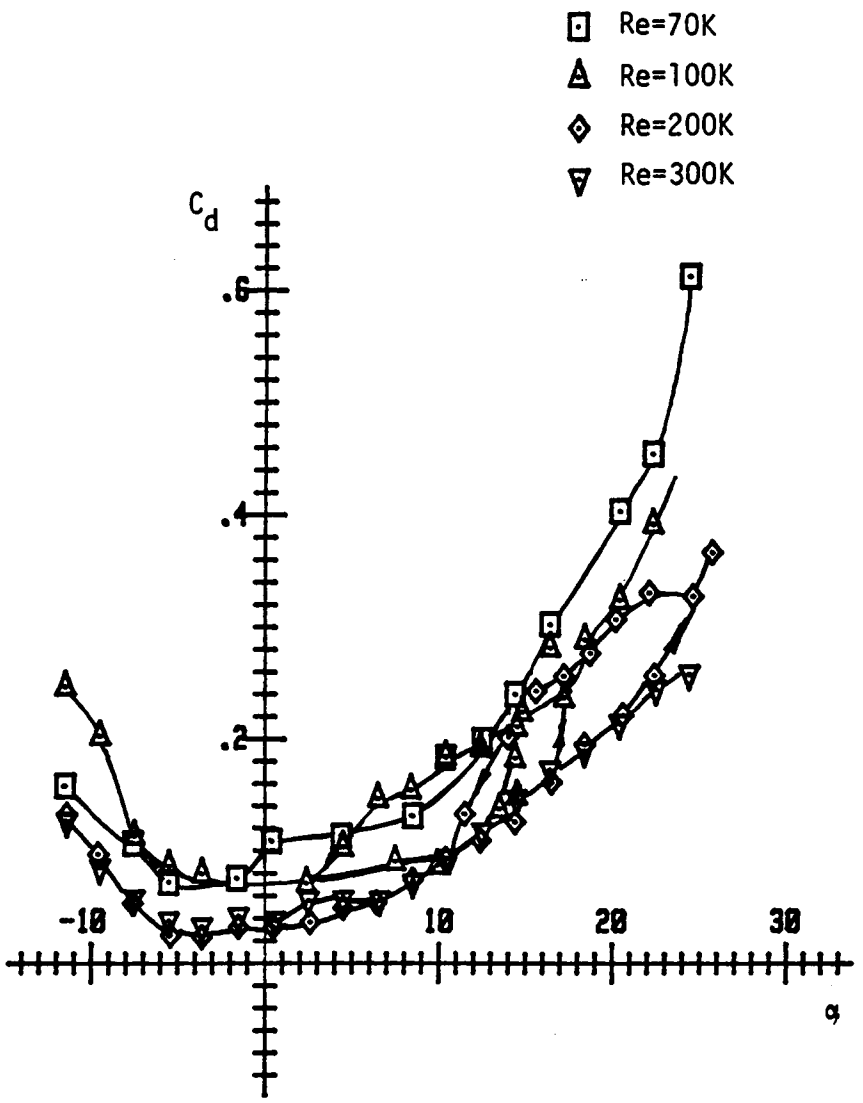

Fig. 4.4 $C_d \rightarrow \alpha$ for AR=4

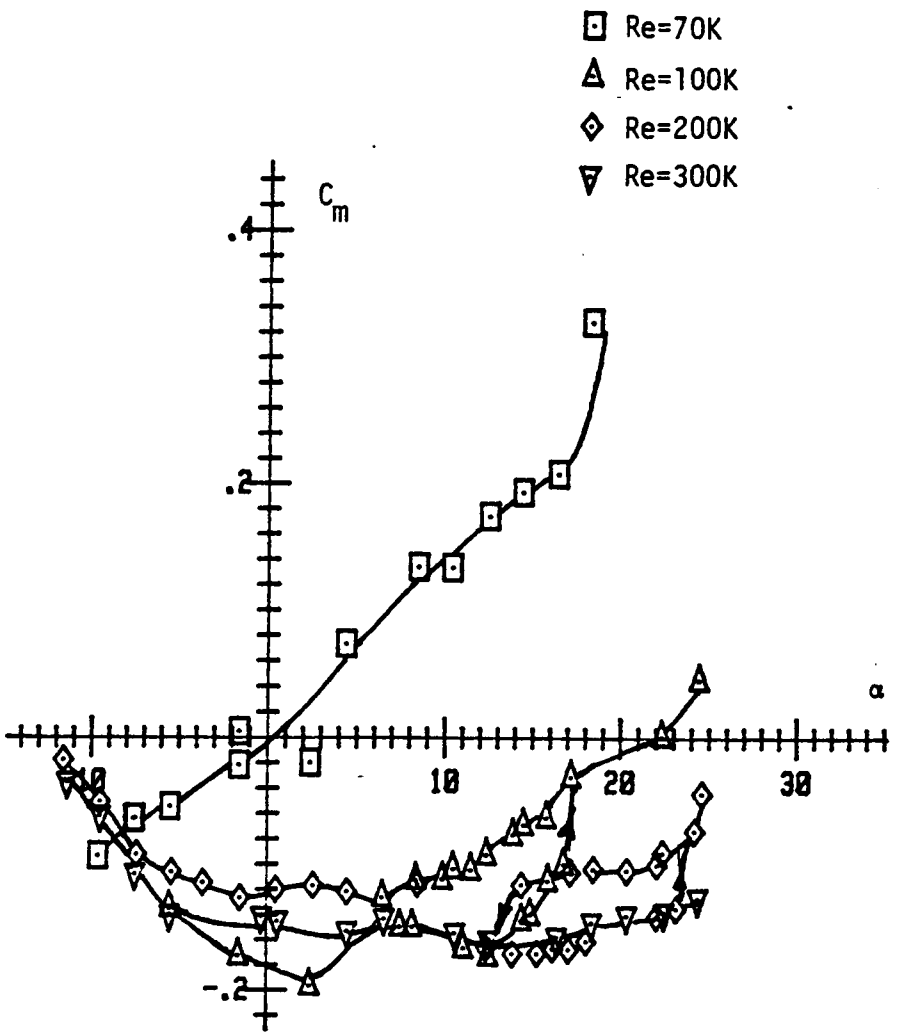

Fig. 4.5 $C_m \rightarrow \alpha$ for AR=4

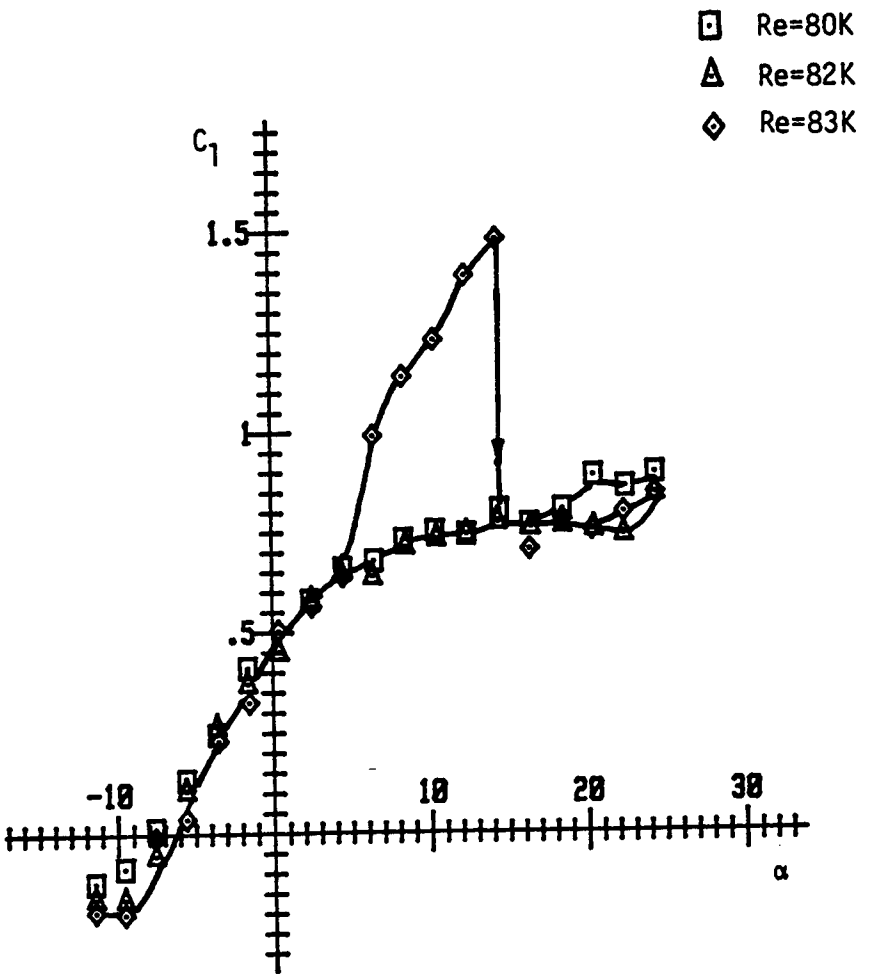

Fig. 4.6 a) $C_l \rightarrow \alpha$ for AR=6

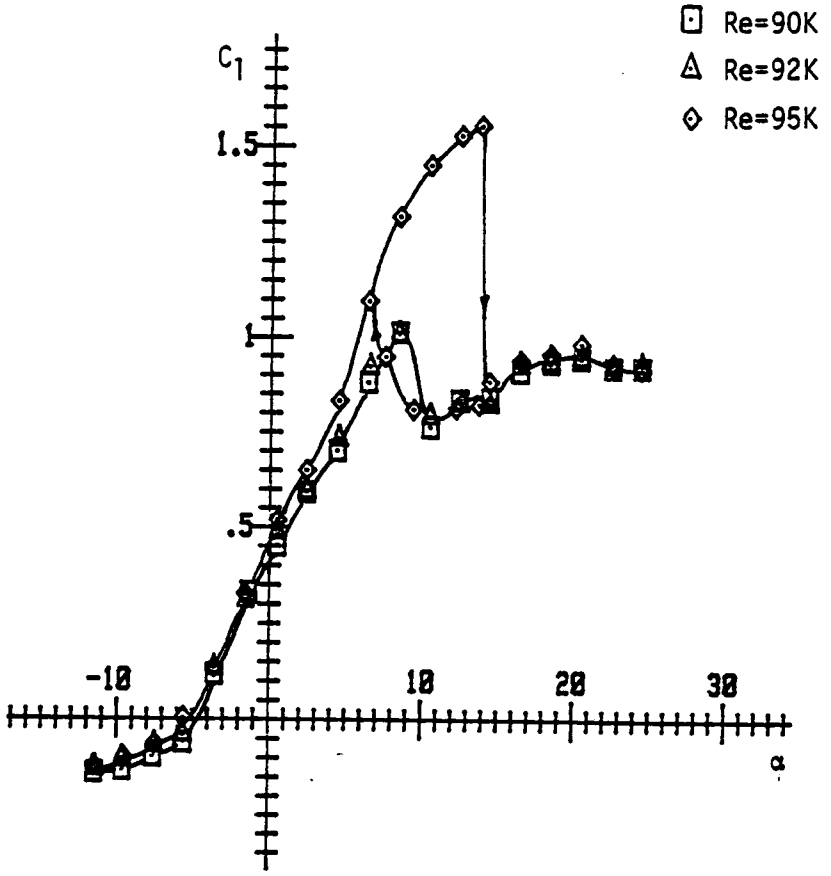

Fig. 4.6 b) $C_l \rightarrow \alpha$ for AR=10

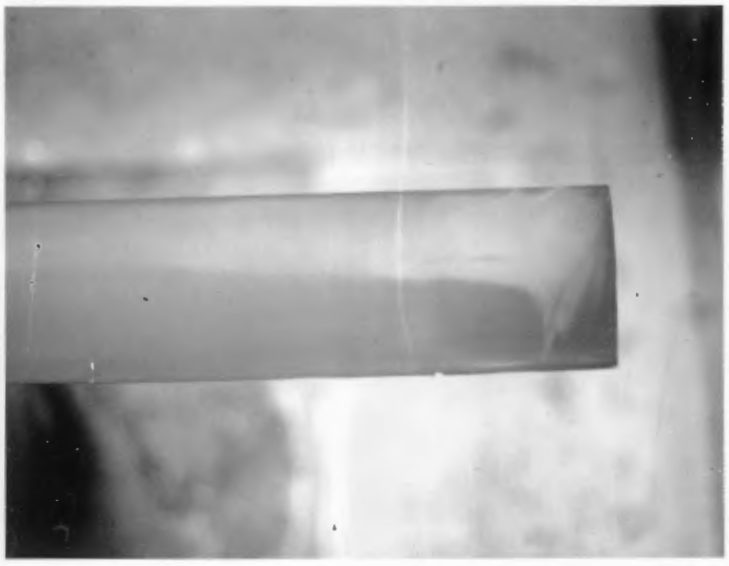

Fig. 4.7 Evaporative film photograph of wingtip effects

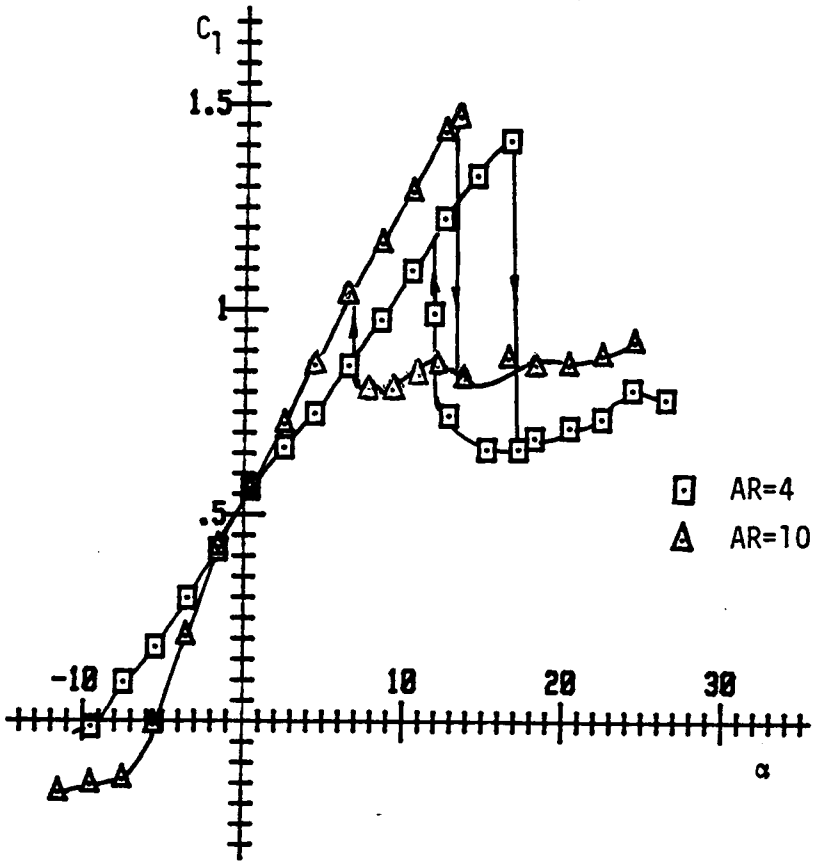

Fig. 4.8 $C_l \rightarrow \alpha$ for Re=100K

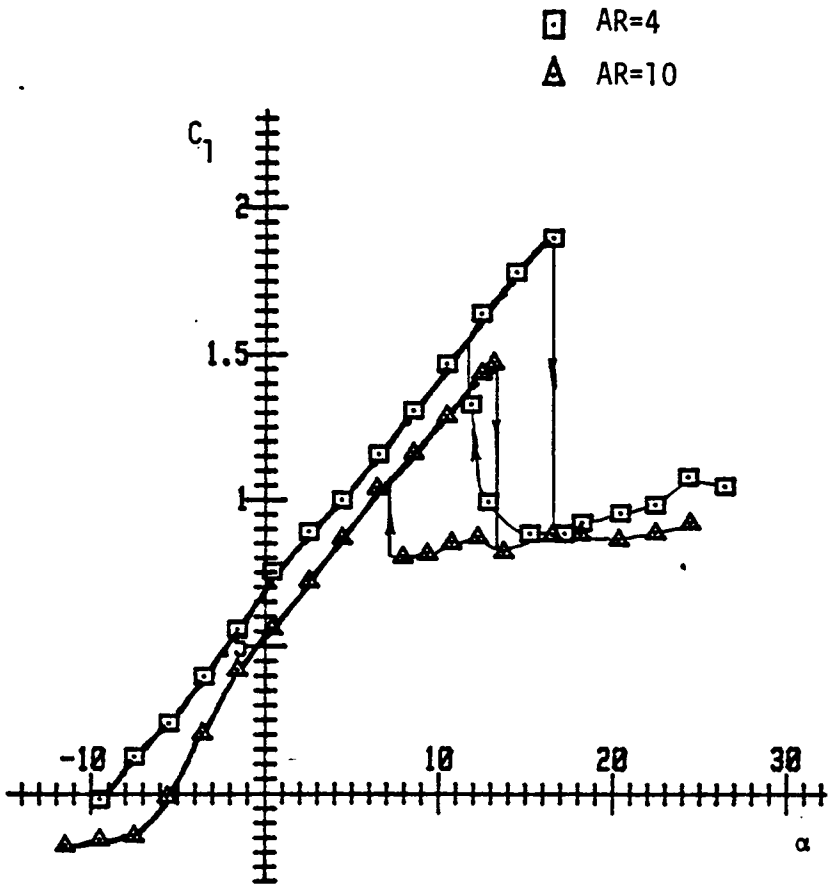

Fig. 4.9 $C_l \rightarrow \alpha$ for Re=100K corrected to AR=10

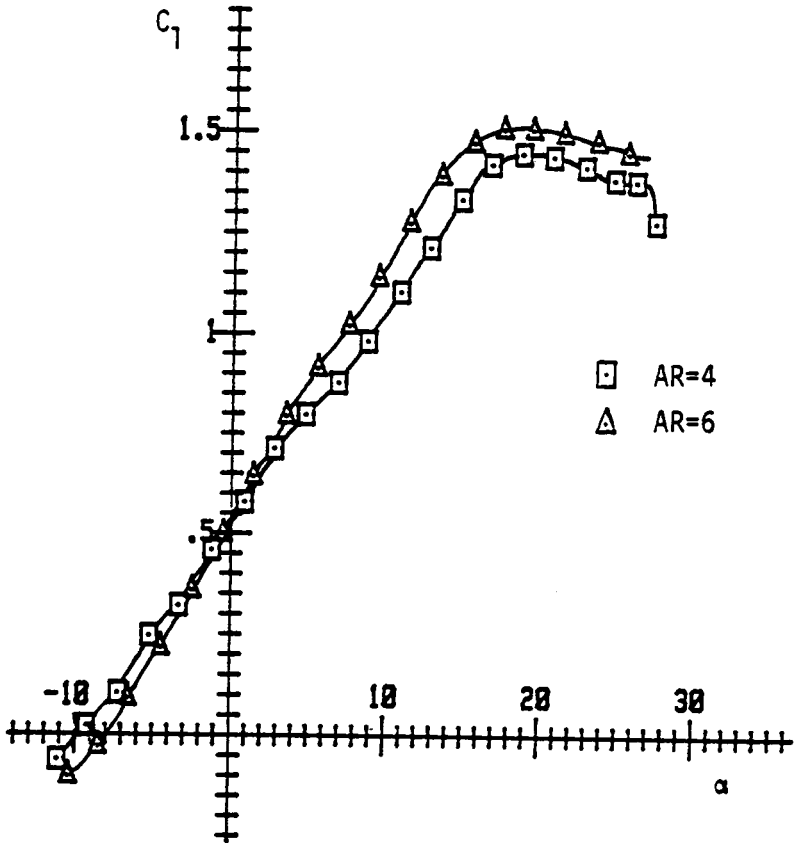

Fig. 4.10 $C_l \rightarrow \alpha$ for Re=300K

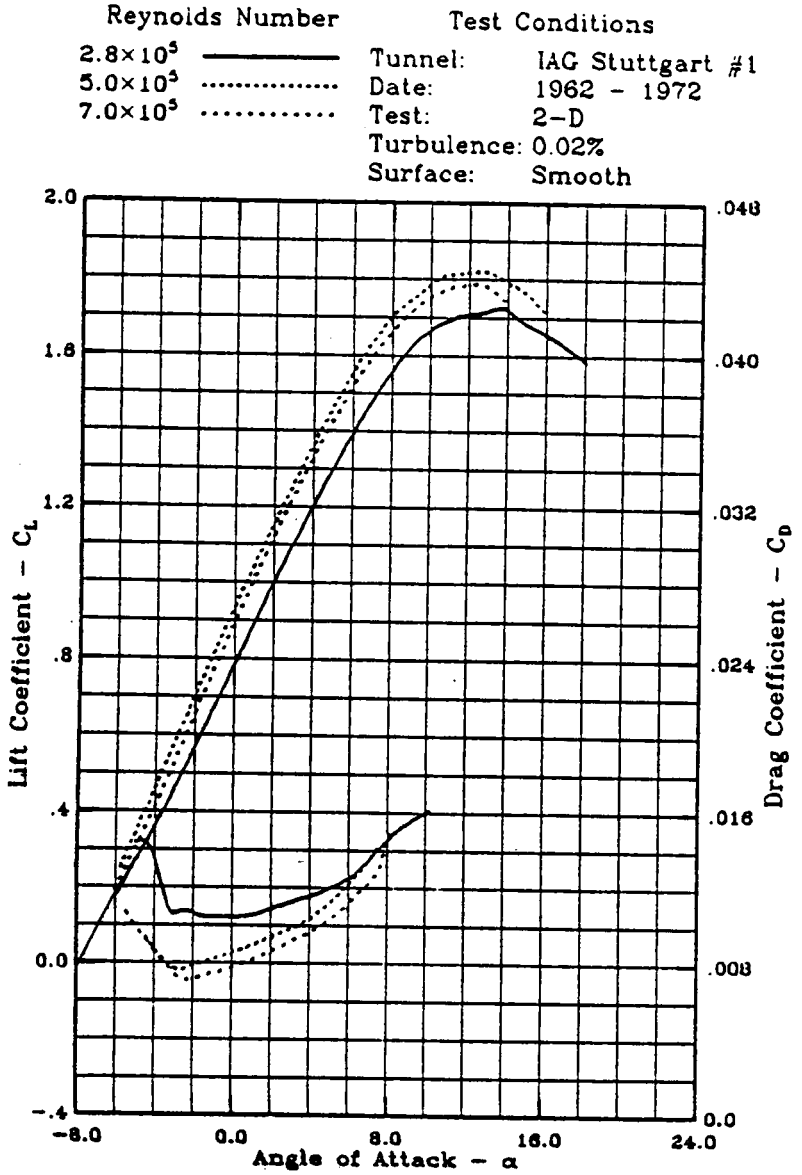

Fig. 4.11 a) $C_l \rightarrow \alpha$ obtained in Stuttgart #1 wind tunnel

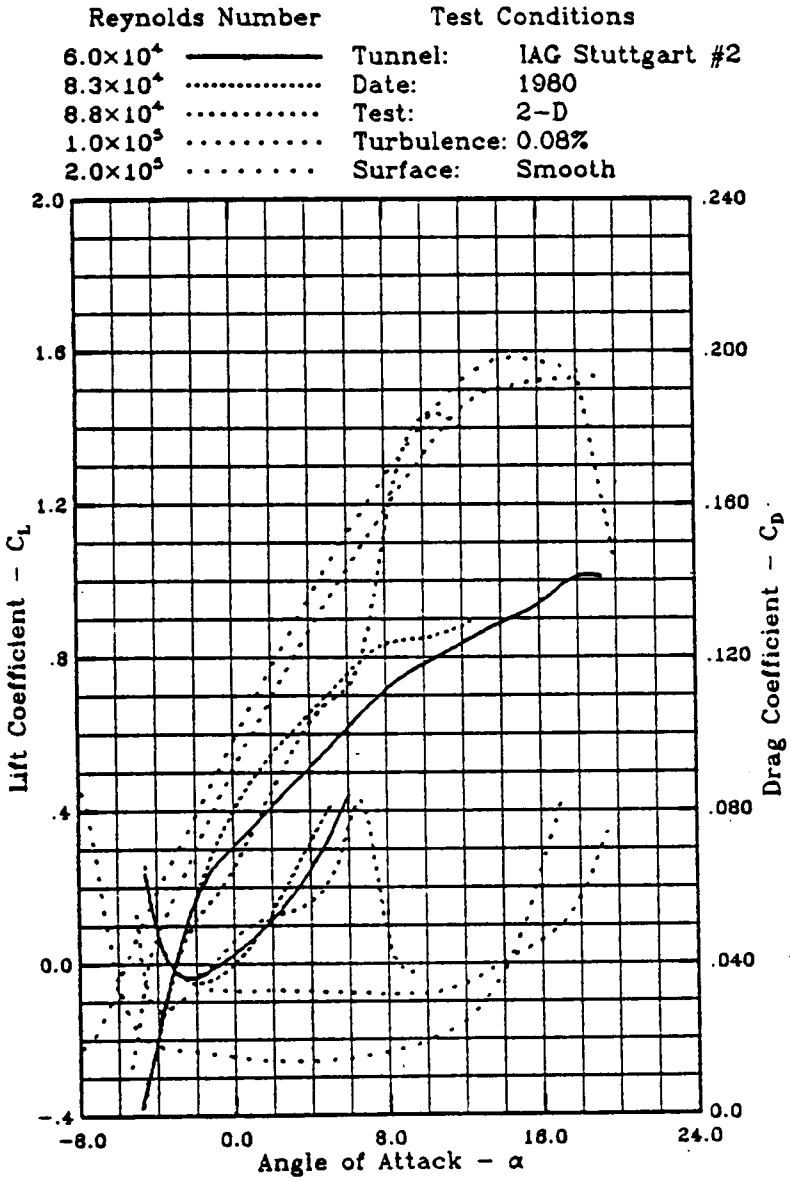

Fig. 4.11 b) $C_l \rightarrow \alpha$ obtained in Stuttgart #2 wind tunnel

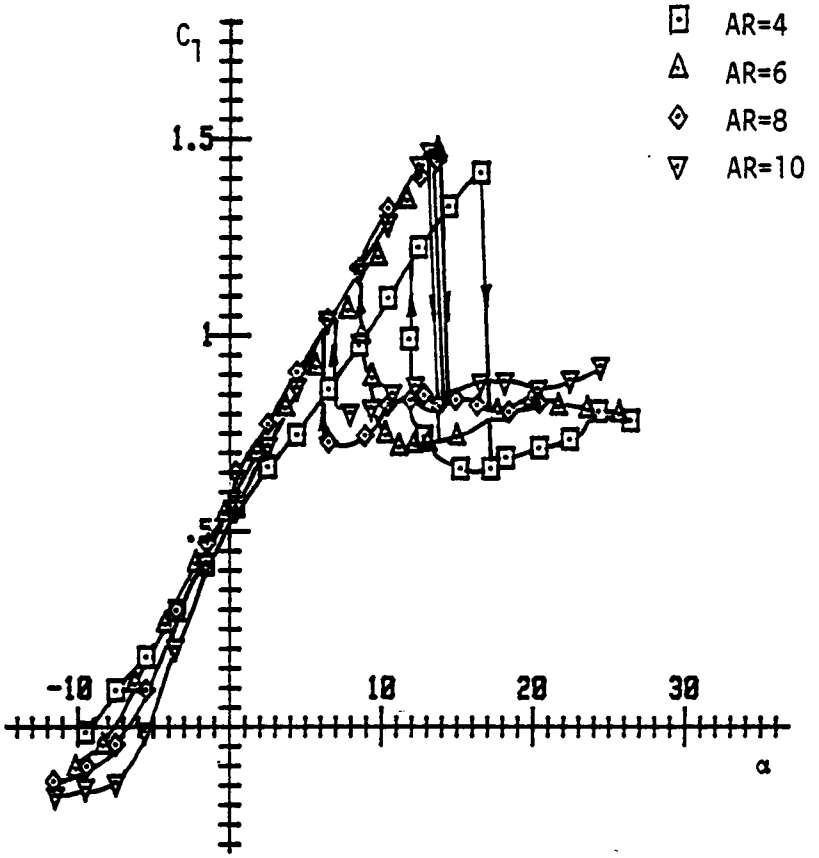

Fig. 4.12 $C_l \rightarrow \alpha$ for Re=100K

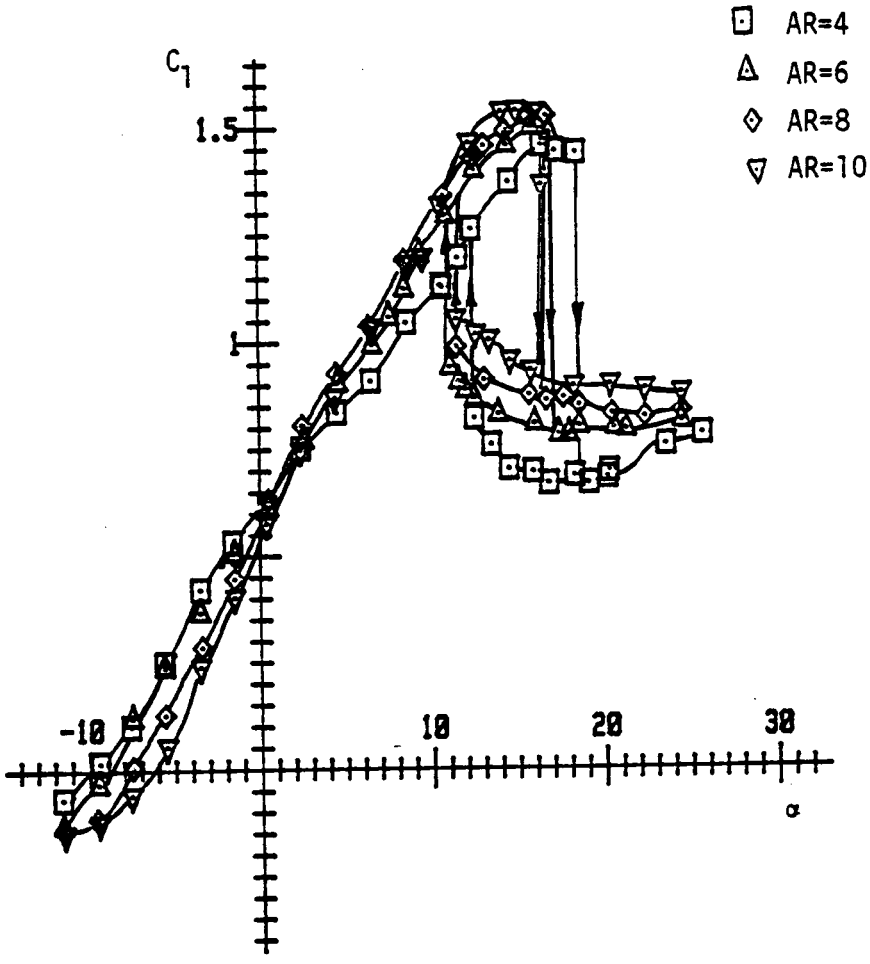

Fig. 4.13 $C_l \rightarrow \alpha$ for Re=150K

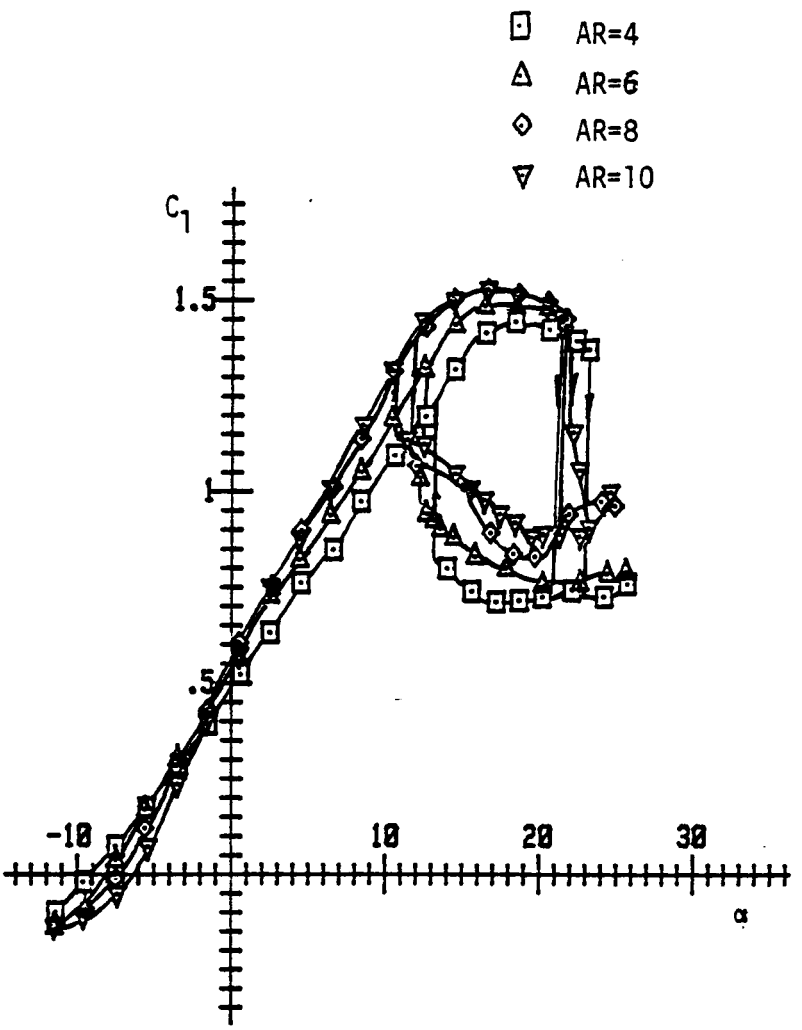

Fig. 4.14 $C_l \rightarrow \alpha$ for Re=200K

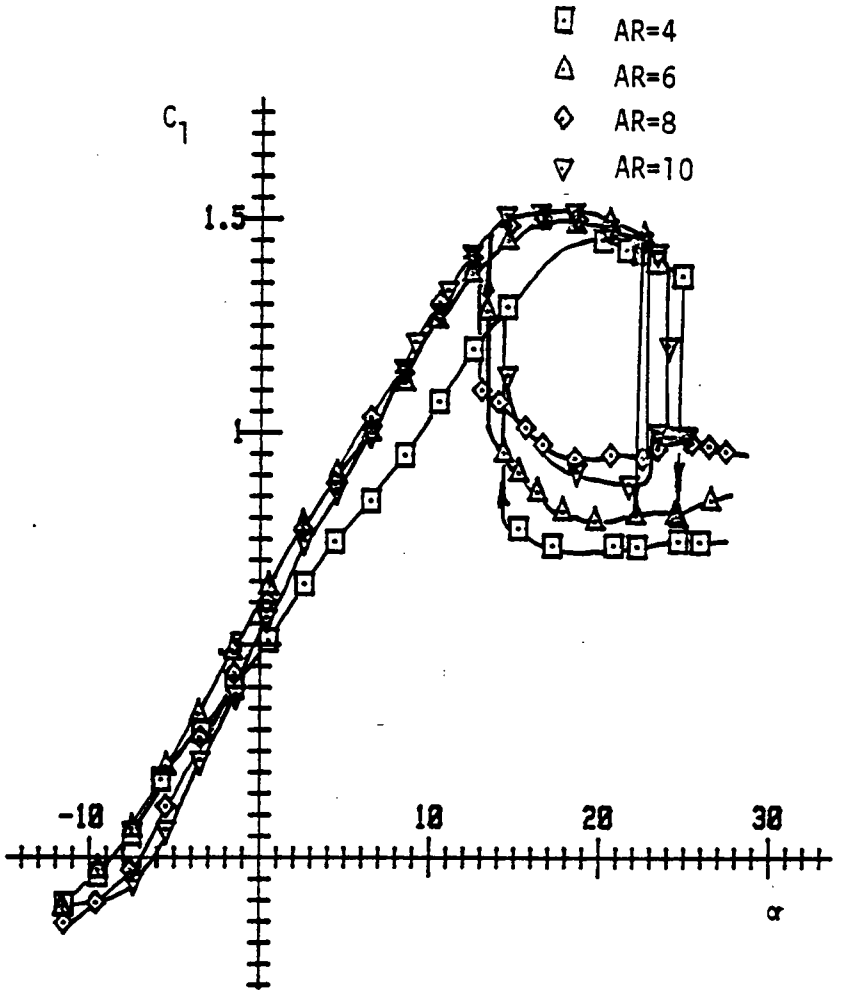

Fig. 4.15 $C_l \rightarrow \alpha$ for Re=250K

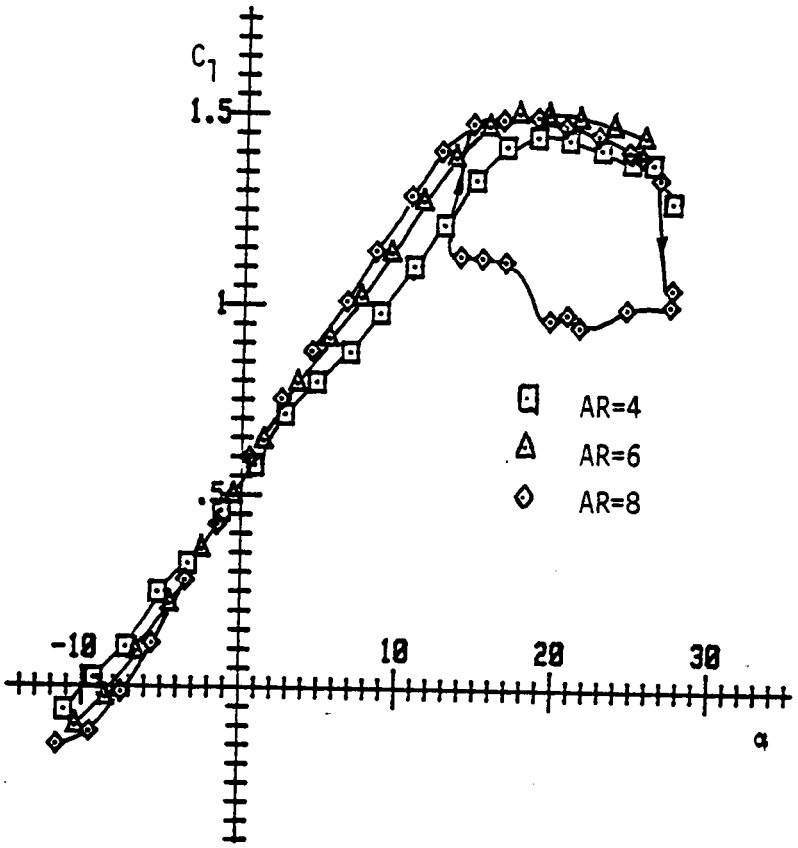

Fig. 4.16 $C_l \rightarrow \alpha$ for Re=300K

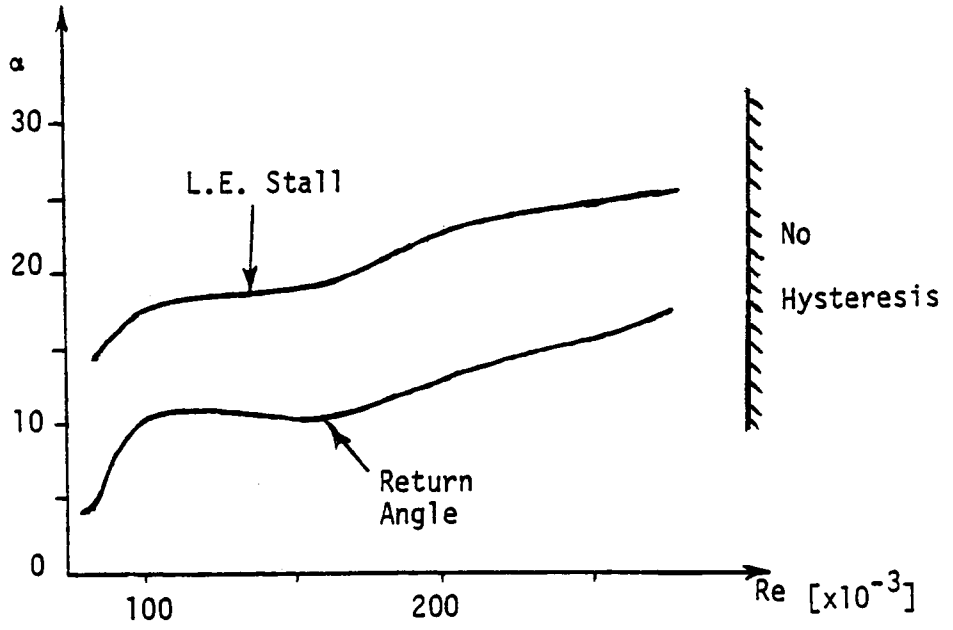

Fig. 4.17 a) Transition angles for hysteresis loop AR=4

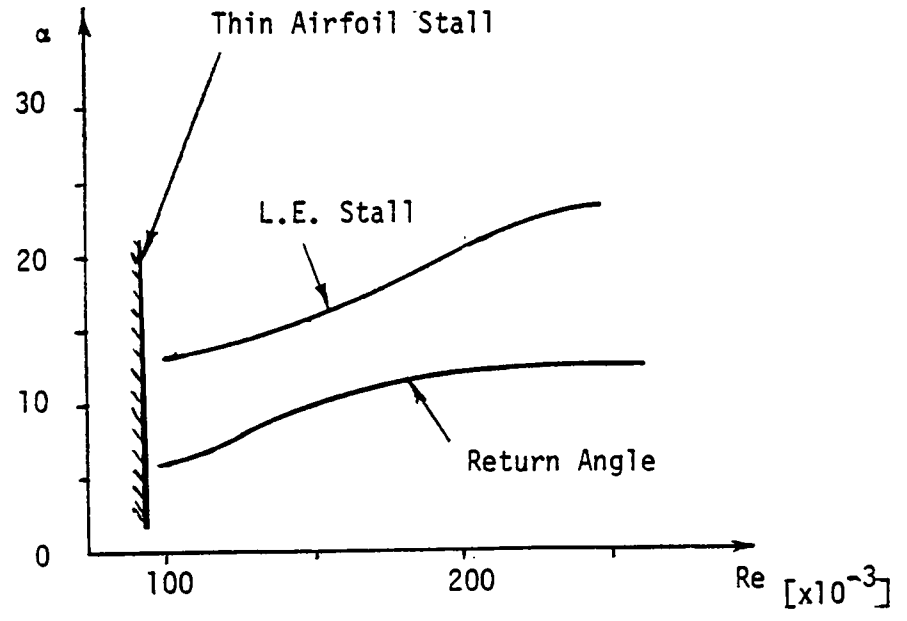

Fig. 4.17 b) Transition angles for hysteresis loop AR=10

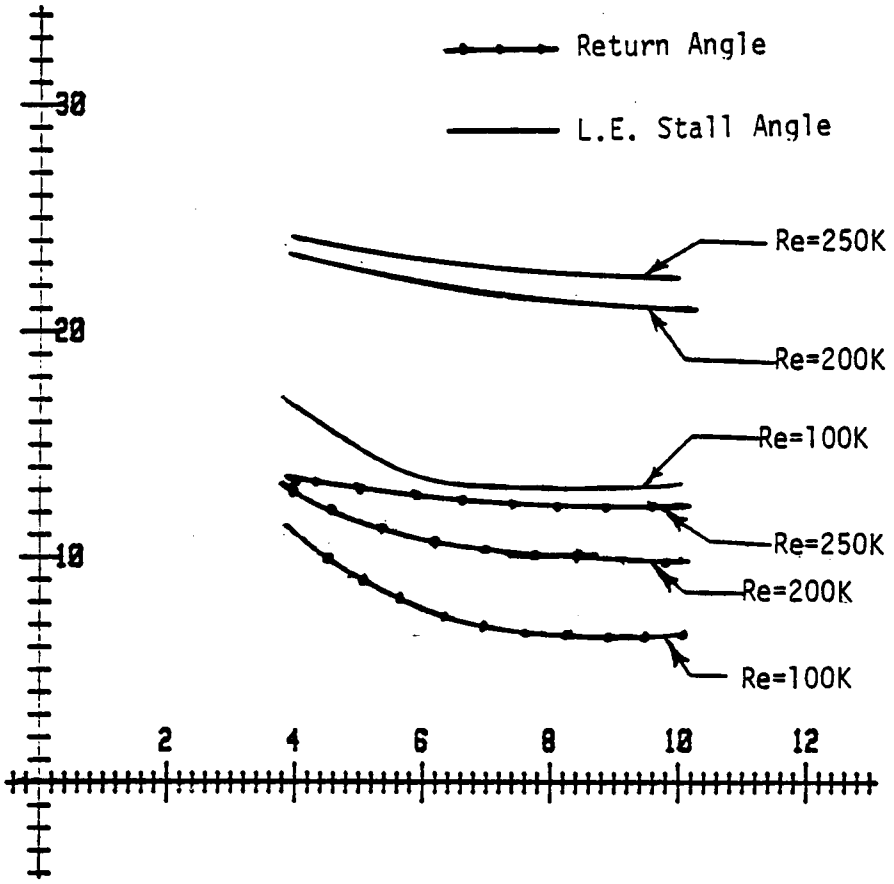

Fig. 4.18 Transition angles for hysteresis loop vs. AR

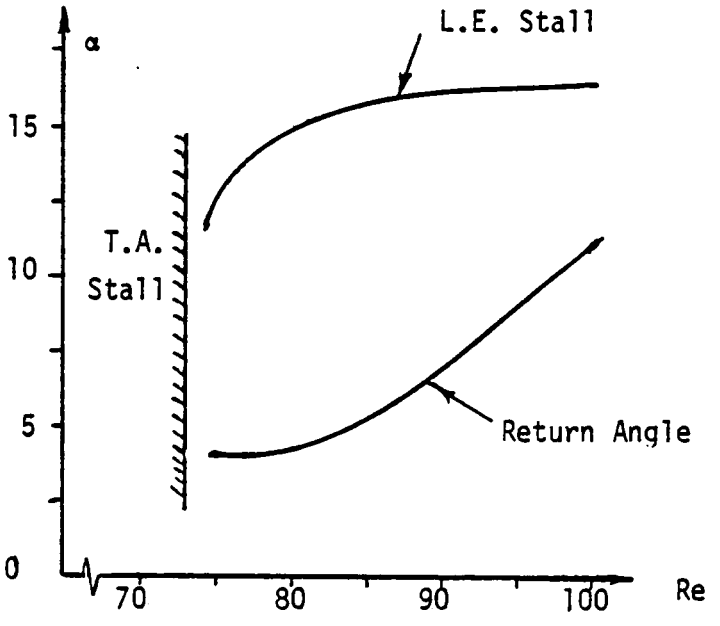

Fig. 4.19 Transition angles for hysteresis loop and onset of thin airfoil stall AR=4

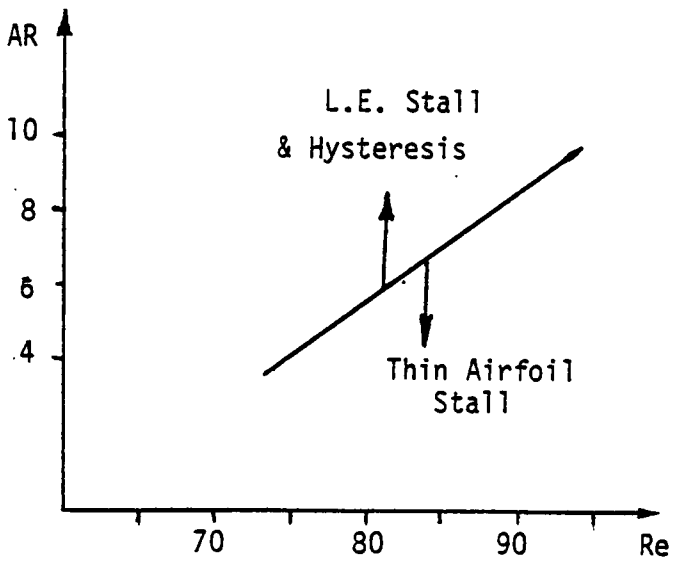

Fig. 4.20 Onset of thin airfoil stall vs. Re

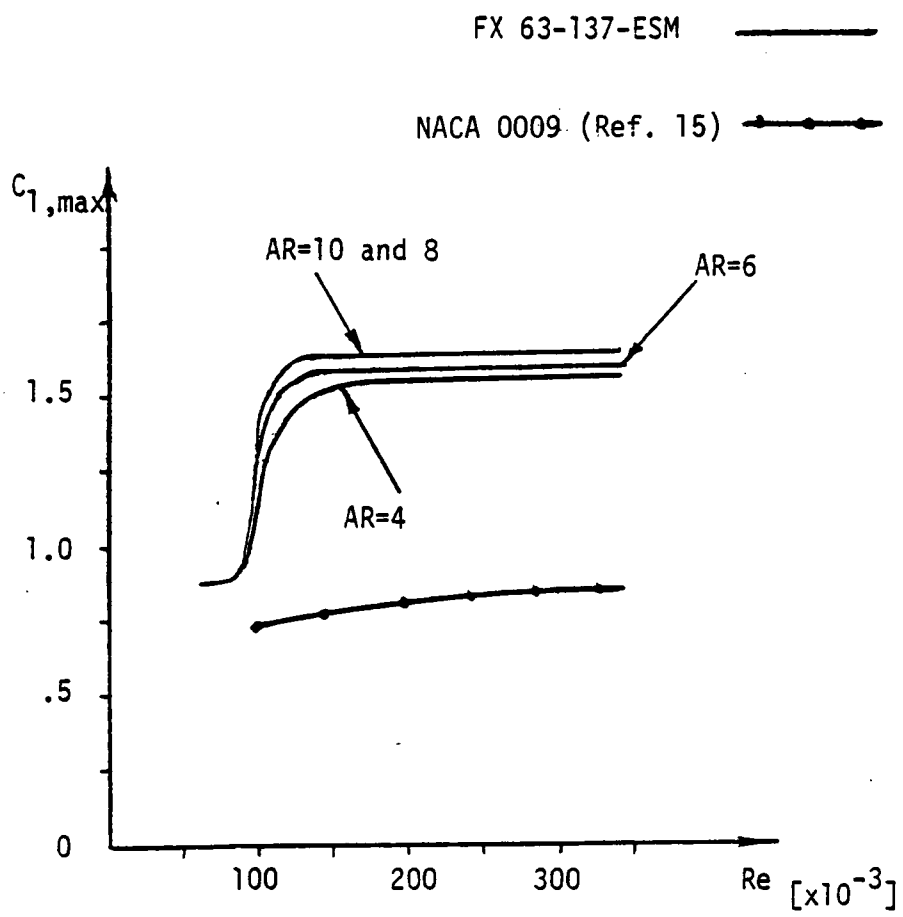

Fig. 4.21 C_{lmax}→Re for FX-63-137-ESM and NACA 0009

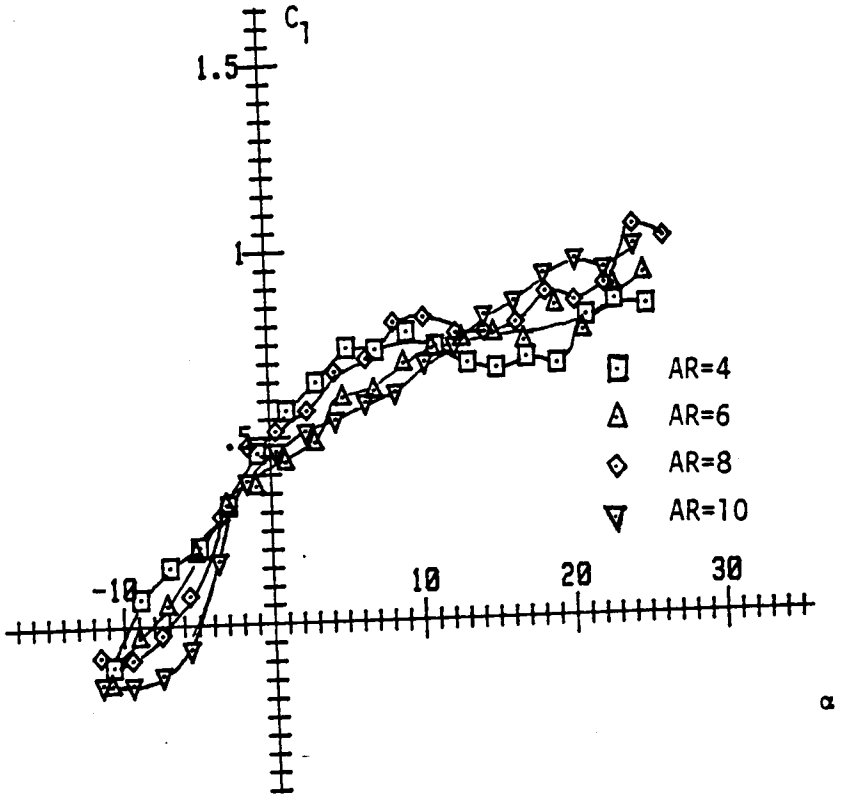

Fig. 4.22 $C_l \rightarrow \alpha$ for Re=70K

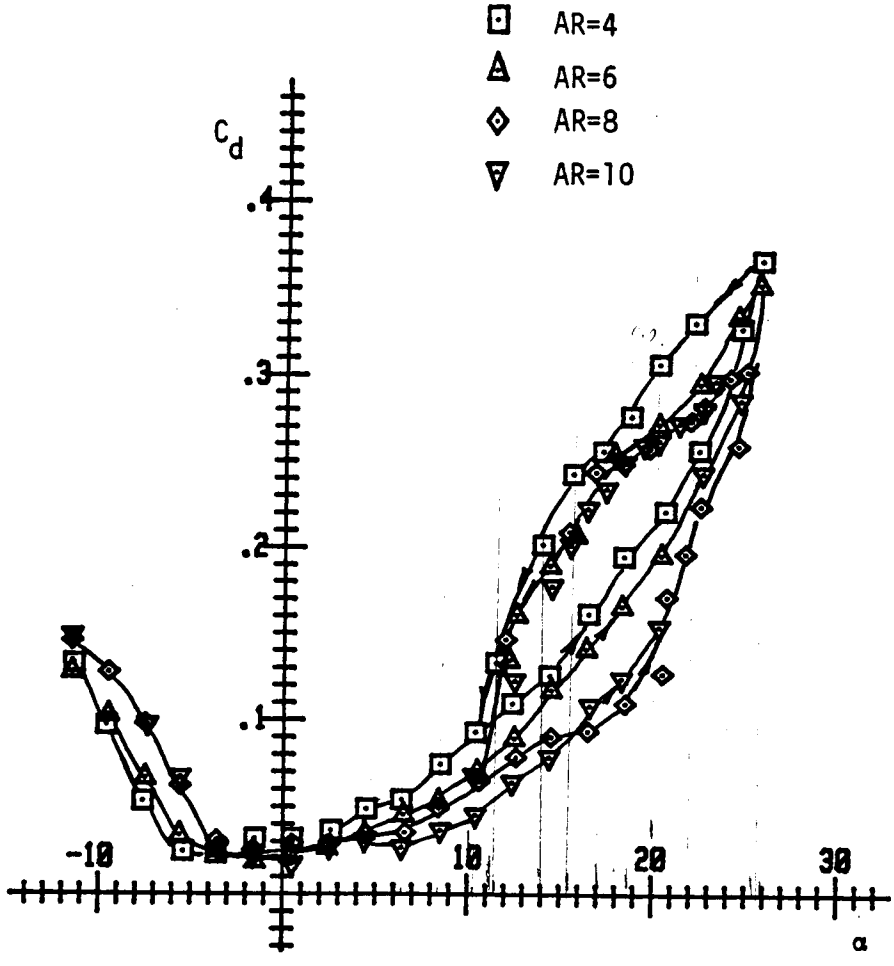

Fig. 4.23 $C_d \rightarrow \alpha$ for Re=200K

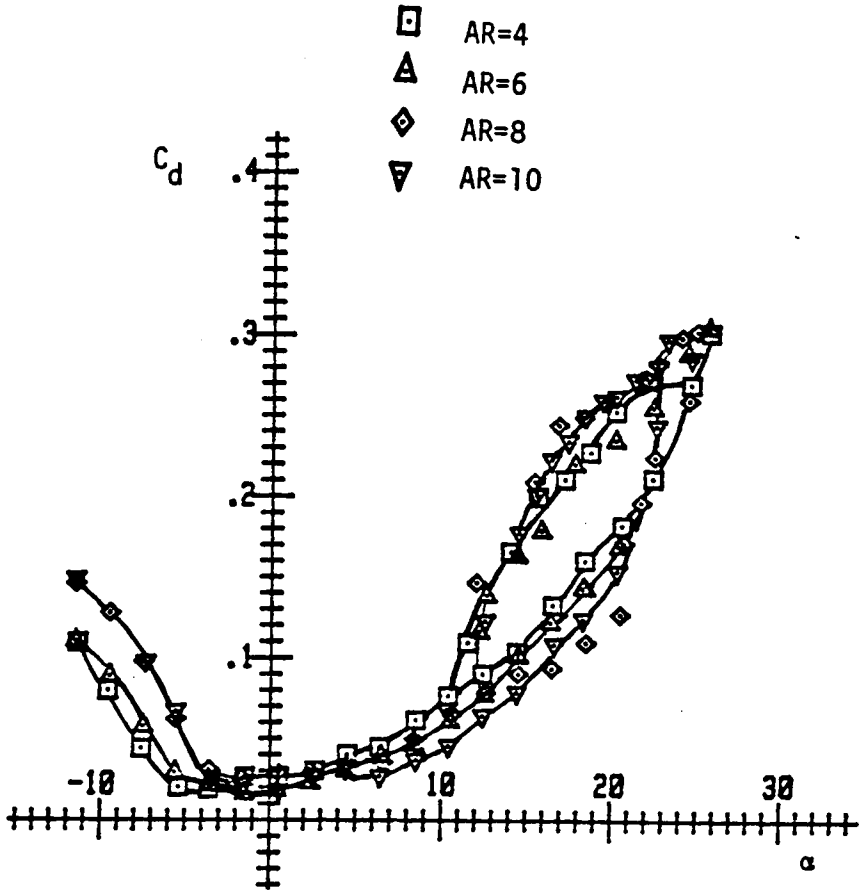

Fig. 4.24 $C_{d\to\alpha}$ for Re=200K profile drag only

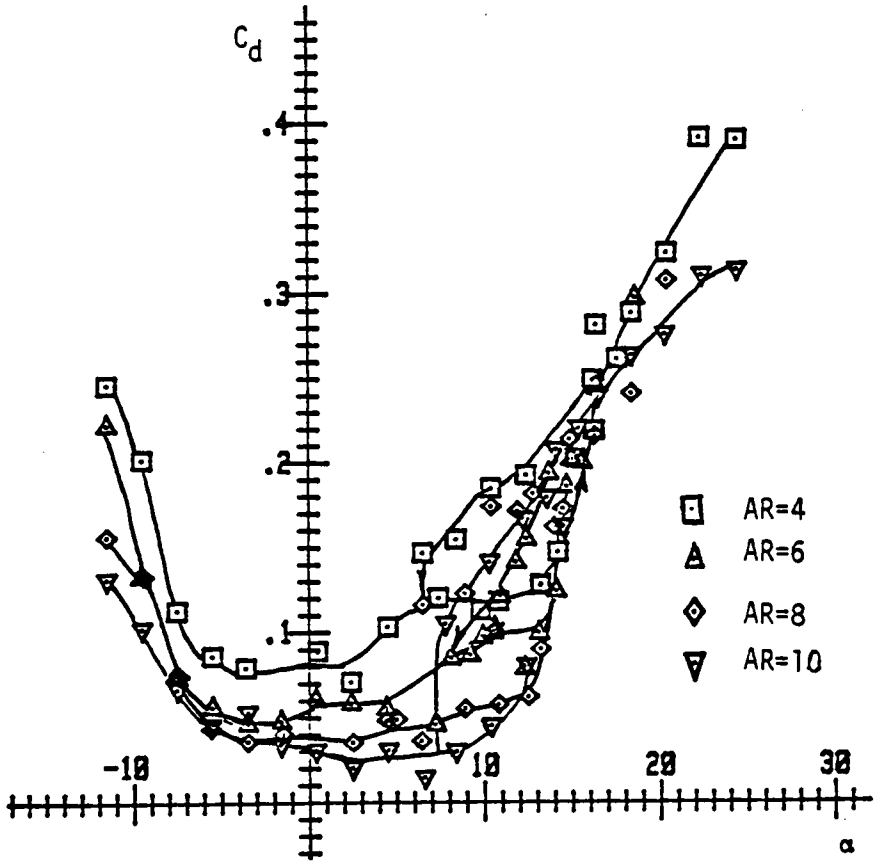

Fig. 4.25 C_d-α for Re=100K

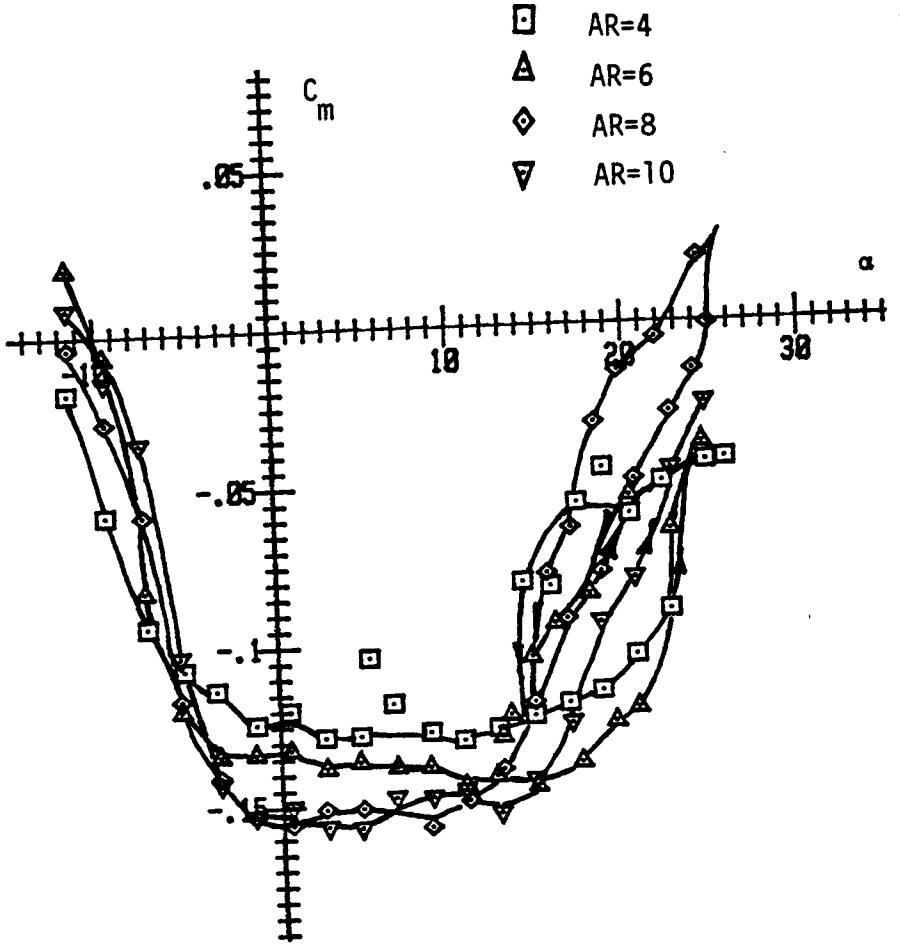

Fig. 4.26 $C_m \rightarrow \alpha$ for Re=200K

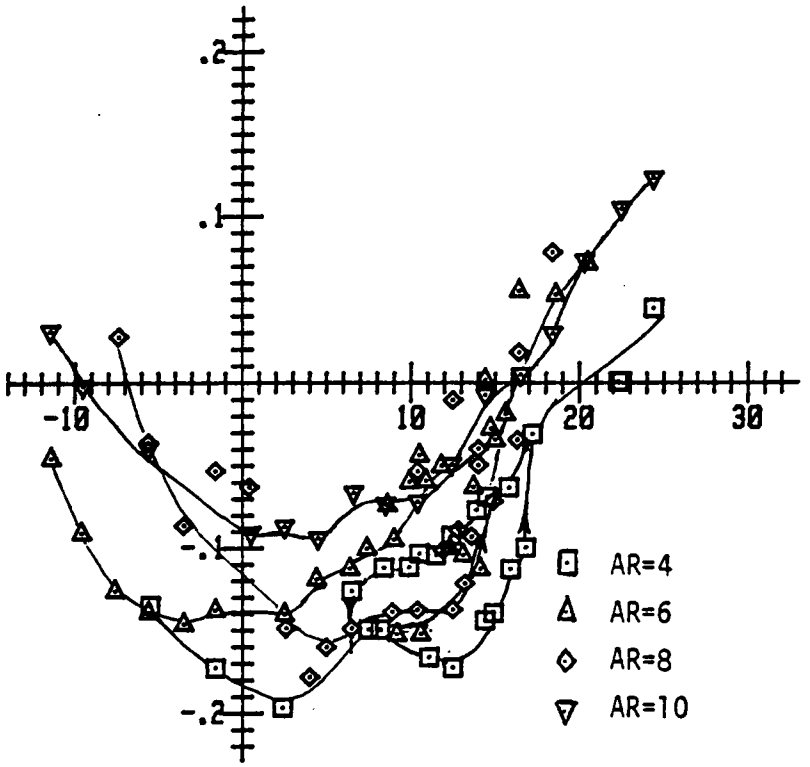

Fig. 4.27 $C_m \rightarrow \alpha$ for Re=100K

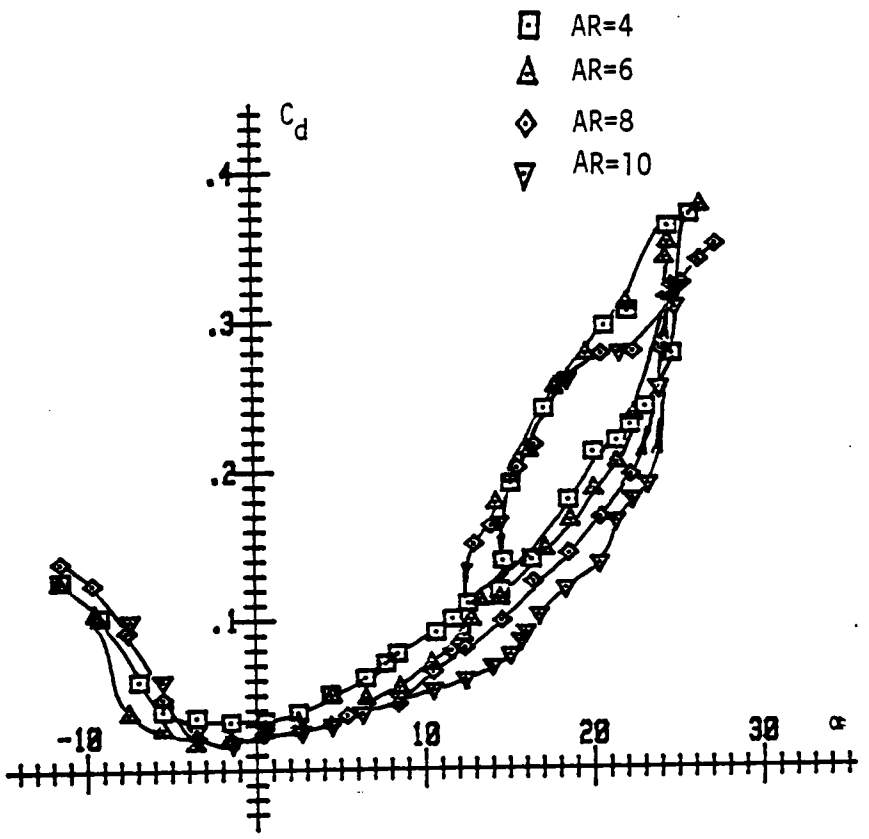

Fig. 4.28 $C_d \rightarrow \alpha$ for Re=250K

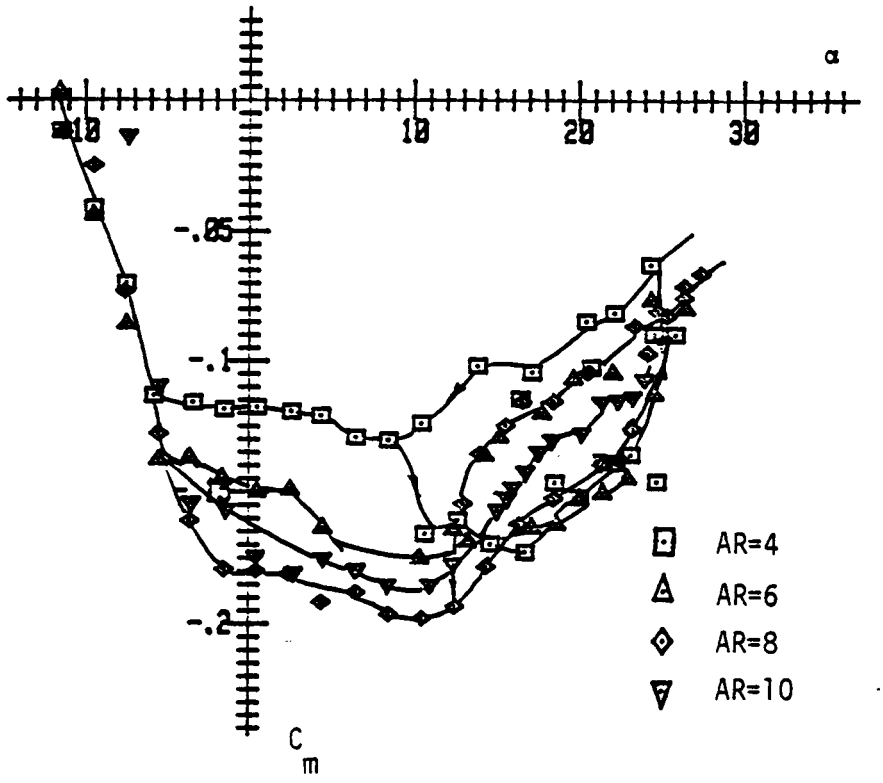

Fig. 4.29 $C_m \rightarrow \alpha$ for Re=250K

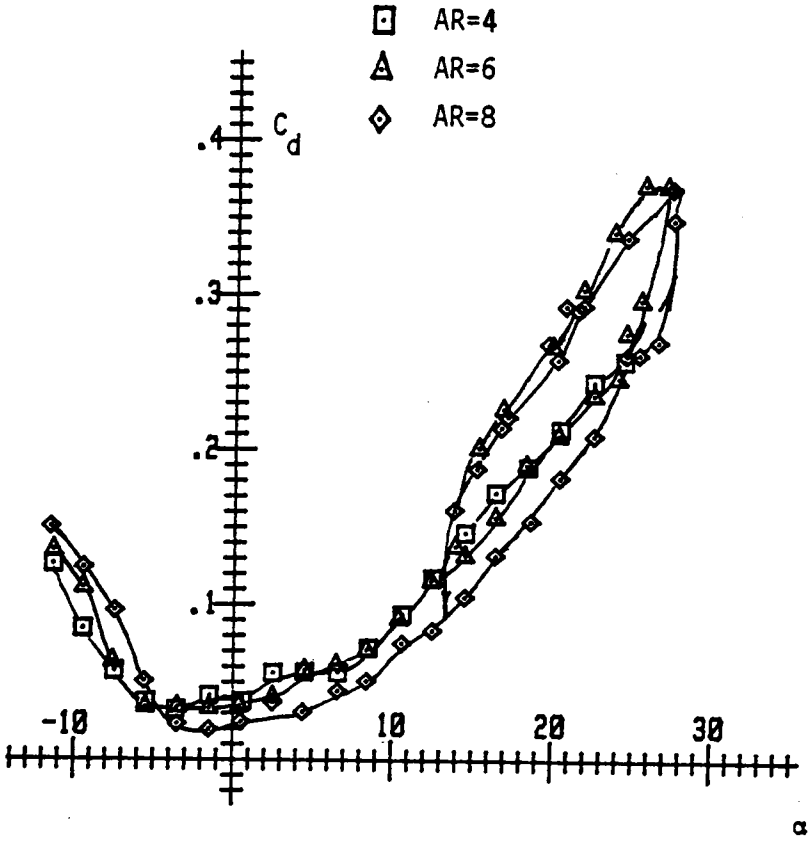

Fig. 4.30 $C_d \rightarrow \alpha$ for Re=300K

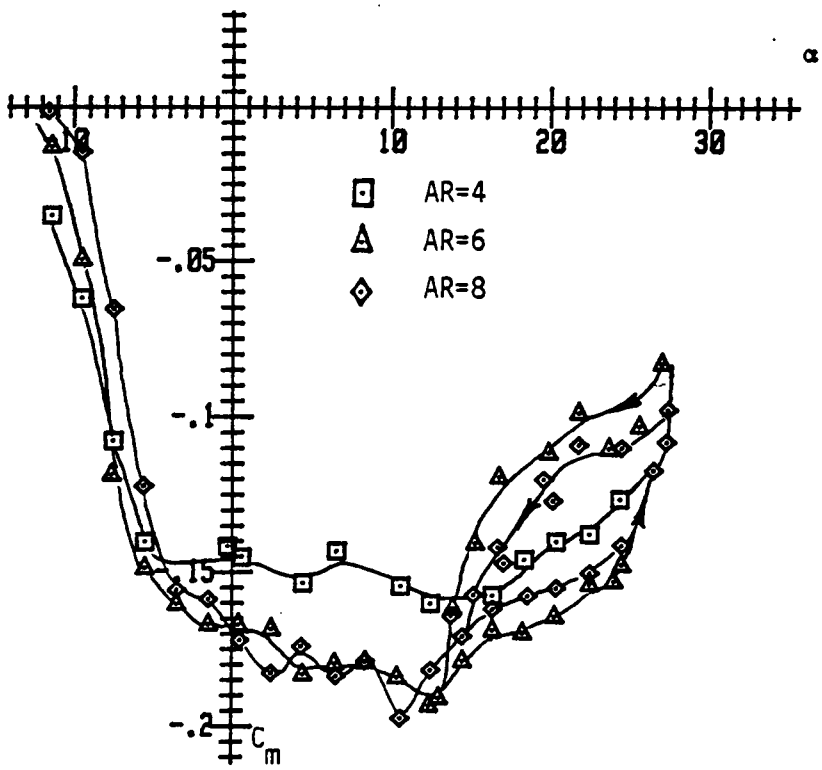

Fig. 4.31 $C_m \rightarrow \alpha$ for Re=300K

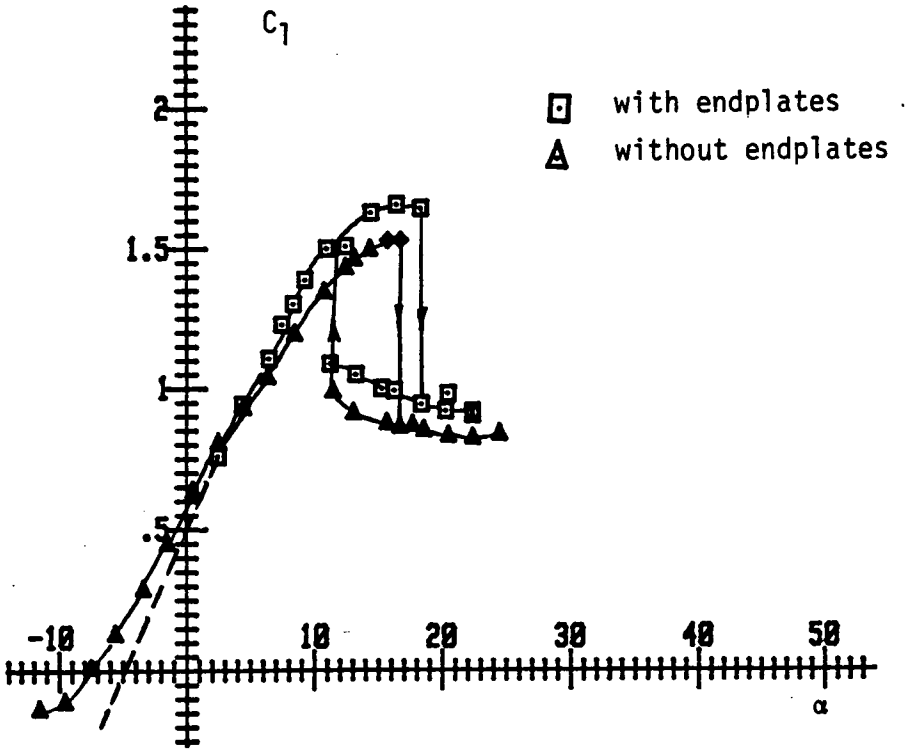

Fig. 4.32 $C_l \rightarrow \alpha$ comparison of cases with and without endplates AR=8 Re=200,000

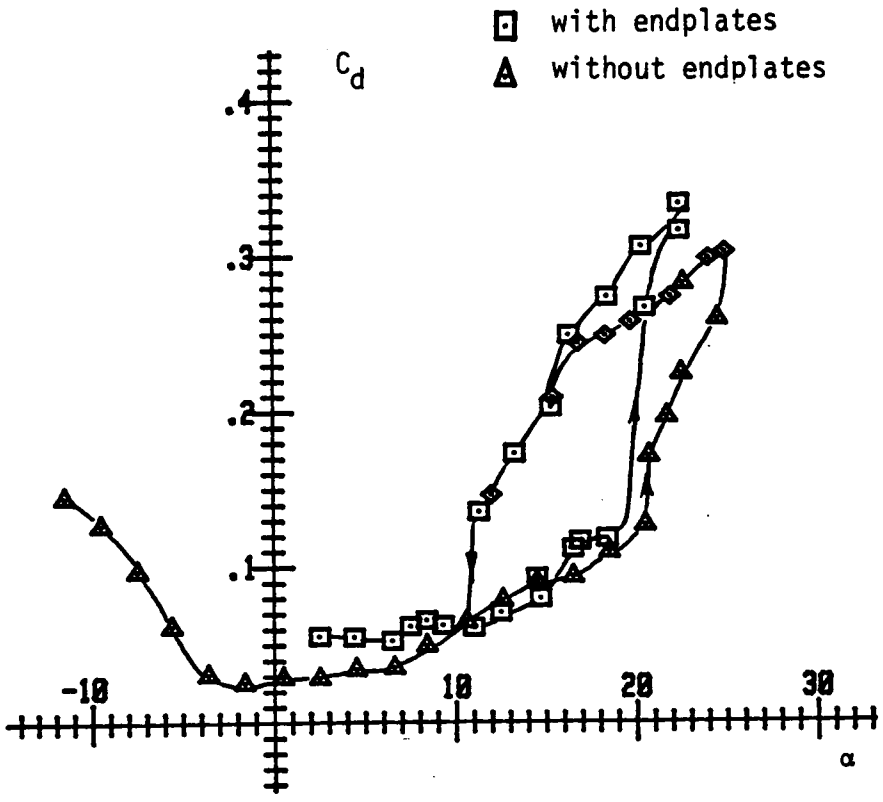

Fig. 4.33 $C_d \rightarrow \alpha$ comparison of cases with and without endplates AR=8 Re=200,000

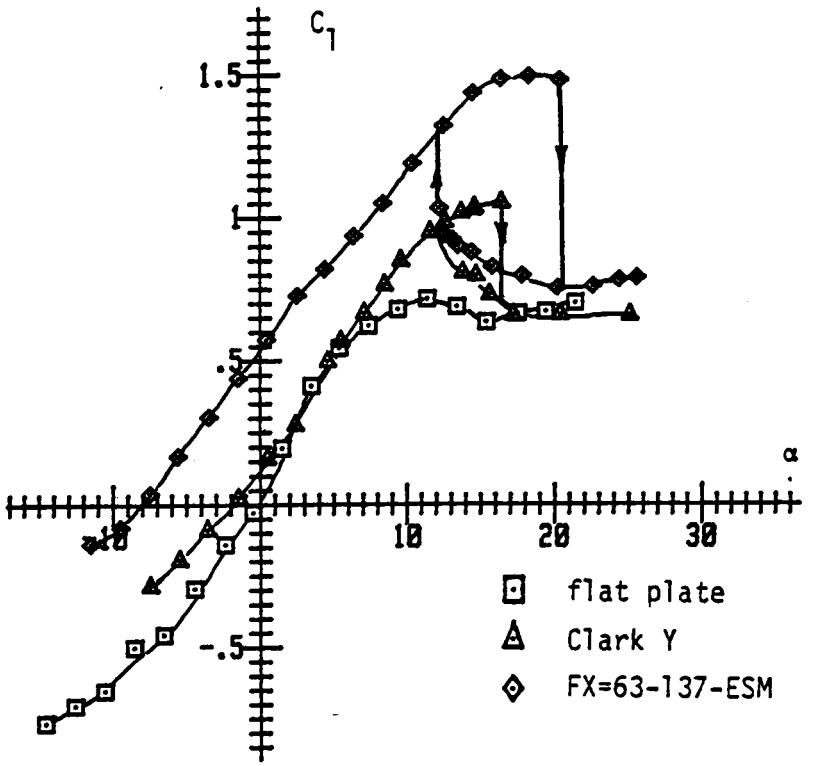

Fig. 4.34 $C_l \rightarrow \alpha$ for flat plate, Clark Y and FX-63-137-ESM , all AR=6, Re=200,000

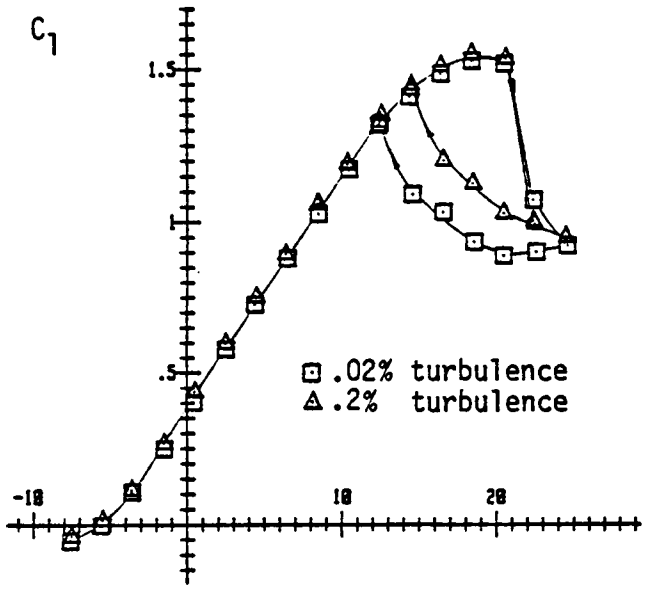

Fig. 4.35 $C_l \rightarrow \alpha$ showing the effects of free stream turbulence on hysteresis loop
AR=8 Re=200,000

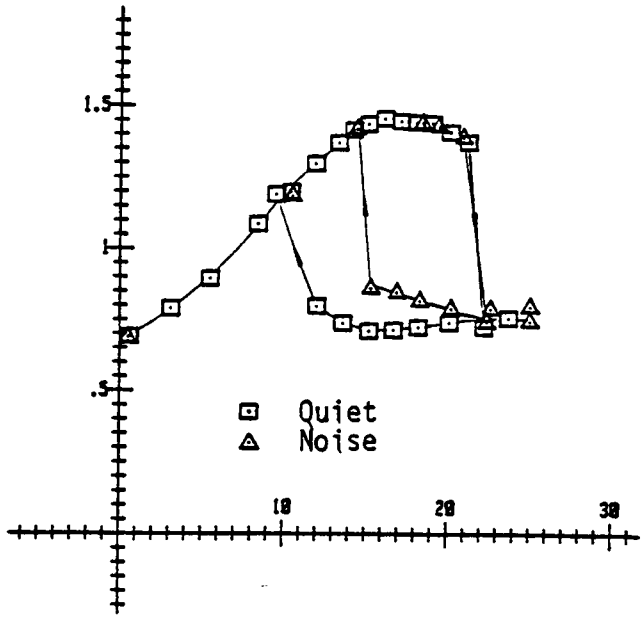

Fig. 4.36 $C_l \rightarrow \alpha$ showing the effects of 5.8kHz noise on hysteresis loop AR=8 Re=200,000

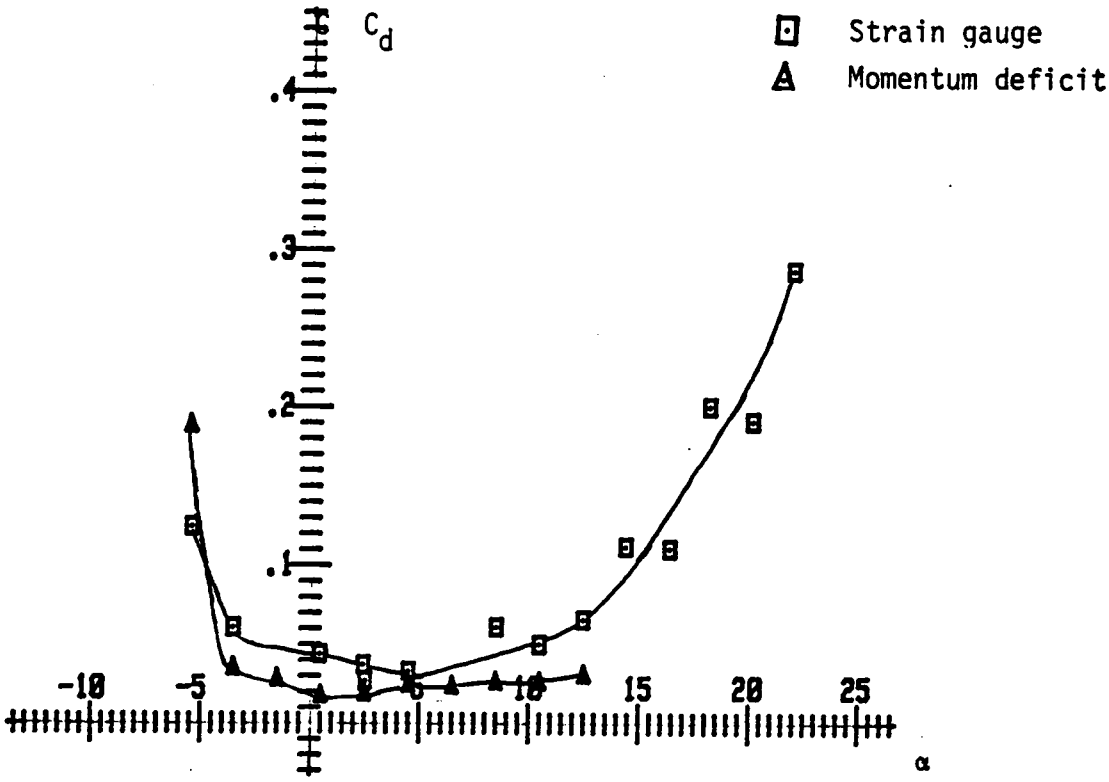

Fig. 4.37 $C_d \rightarrow \alpha$ comparison of results from momentum deficit and strain gauge methods, strain gauge data corrected to 2-D, Re=180,000

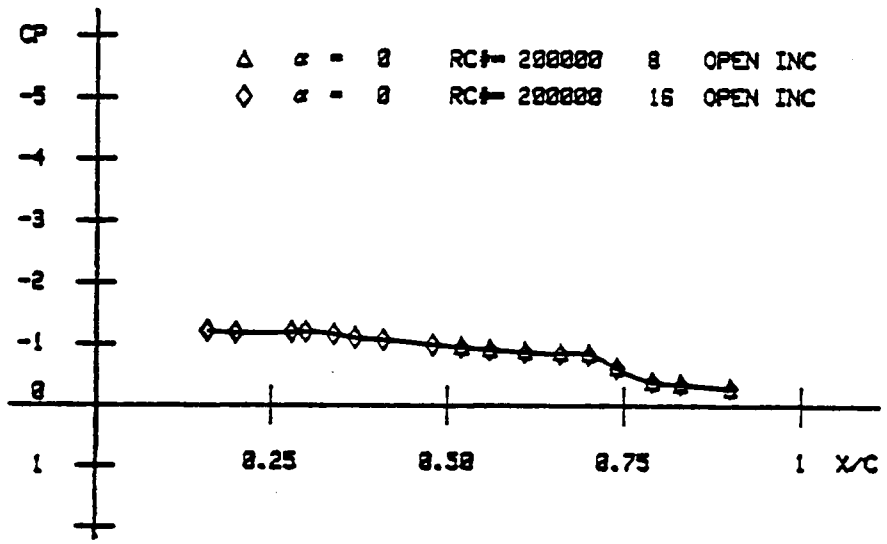

Fig 4.38 Cp→ $\frac{X}{C}$ comparison of 8 and 16 holes open

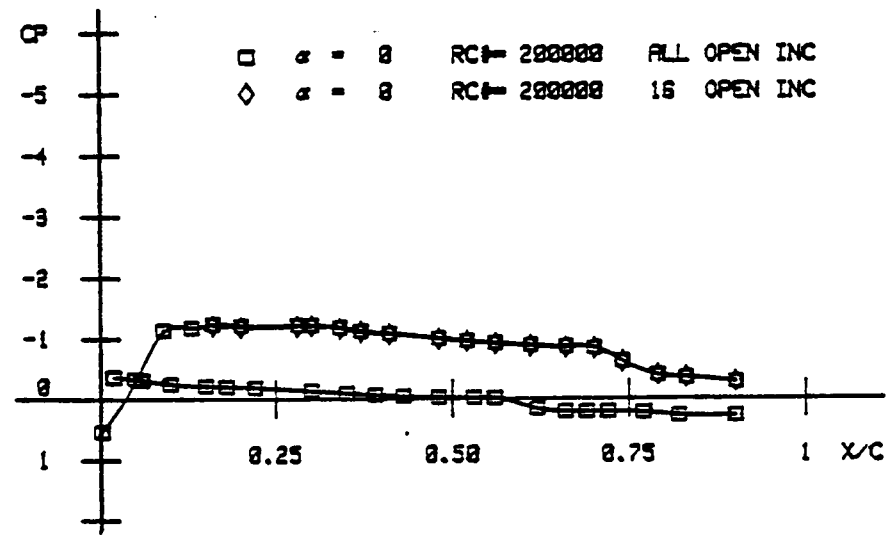

Fig. 4.39 Cp→ $\frac{X}{C}$ comparison of 16 and all holes open

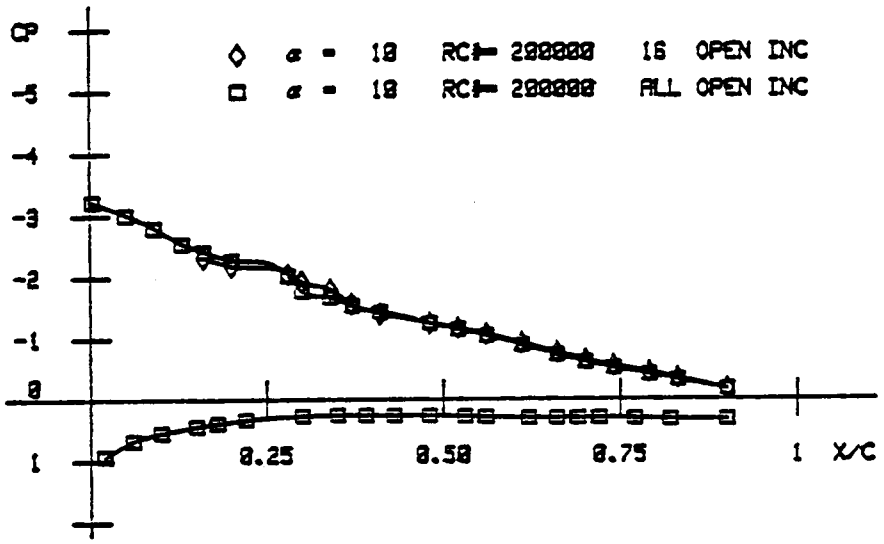

Fig. 4.40 Cp→ $\frac{x}{c}$ comparison of 16 and all holes open

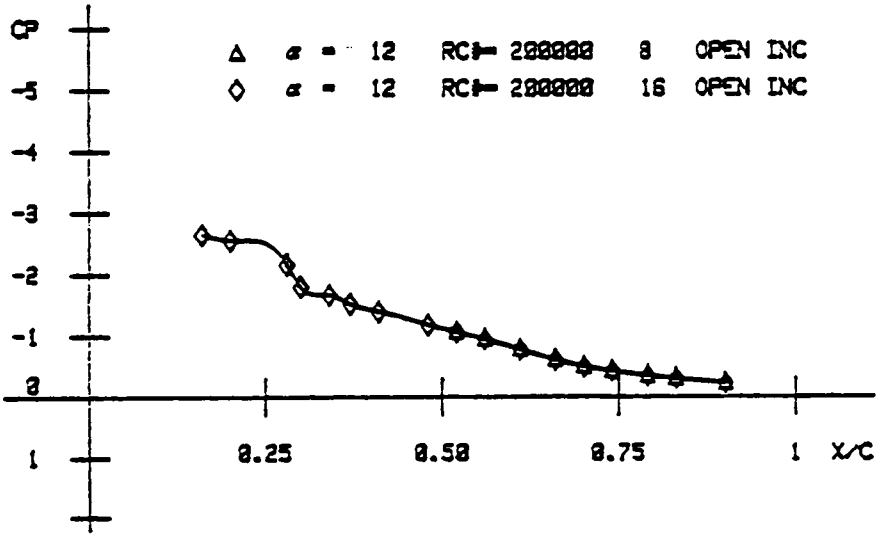

Fig. 4.41 Cp→ $\frac{x}{c}$ comparison of 8 and 16 holes open

Fig. 4.42 Evaporative film photograph of laminar separation bubble
$\alpha=14^0$ Re=200,000

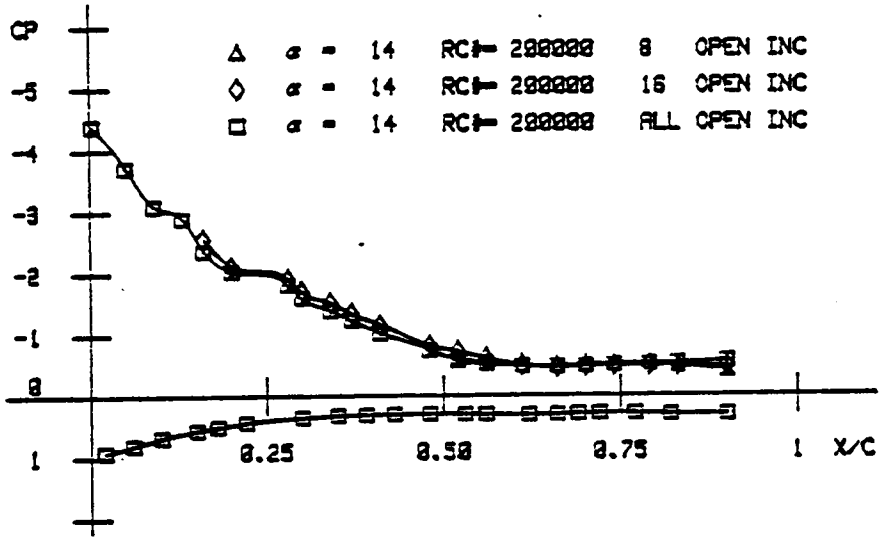

Fig. 4.43 Cp→ $\frac{X}{C}$ comparison of 8, 16 and all holes open

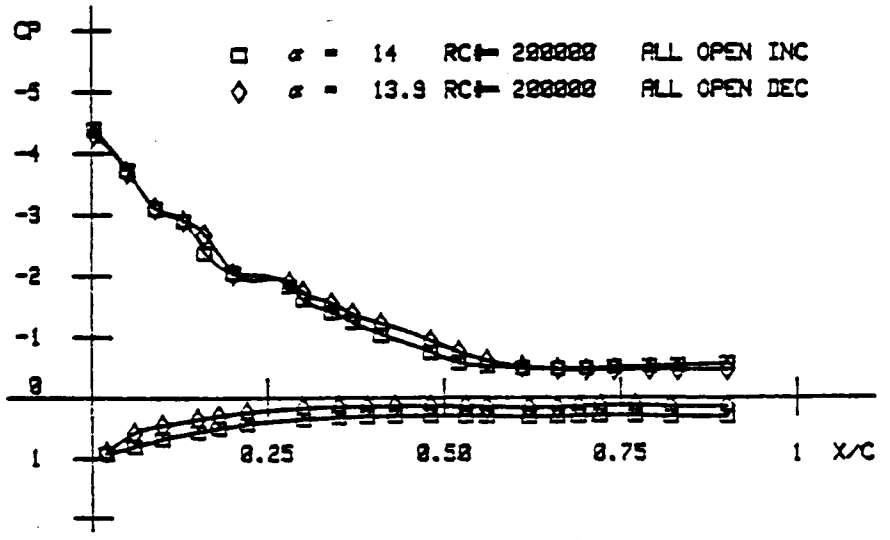

Fig. 4.44 Cp→ $\frac{X}{C}$ comparison of data on upper and lower branch of hysteresis loop

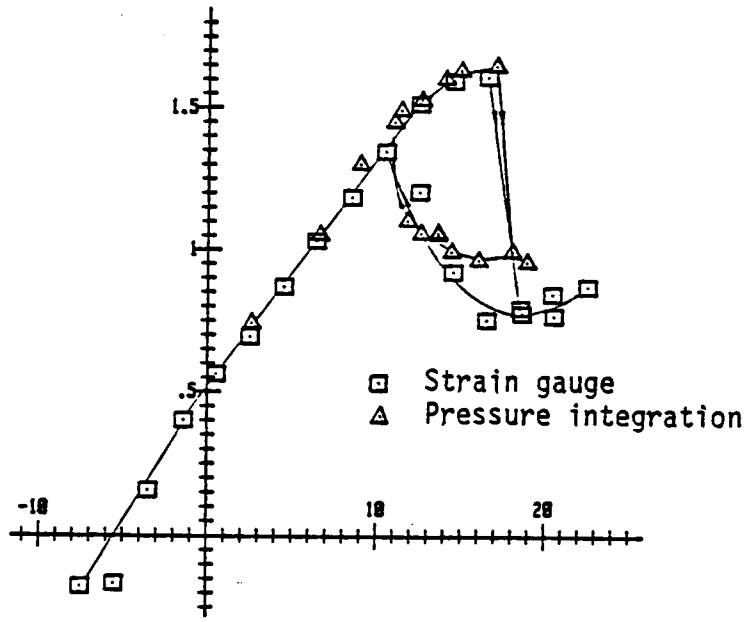

Fig. 4.45 $C_l \rightarrow \alpha$ comparison of data from strain gauge and pressure integration methods

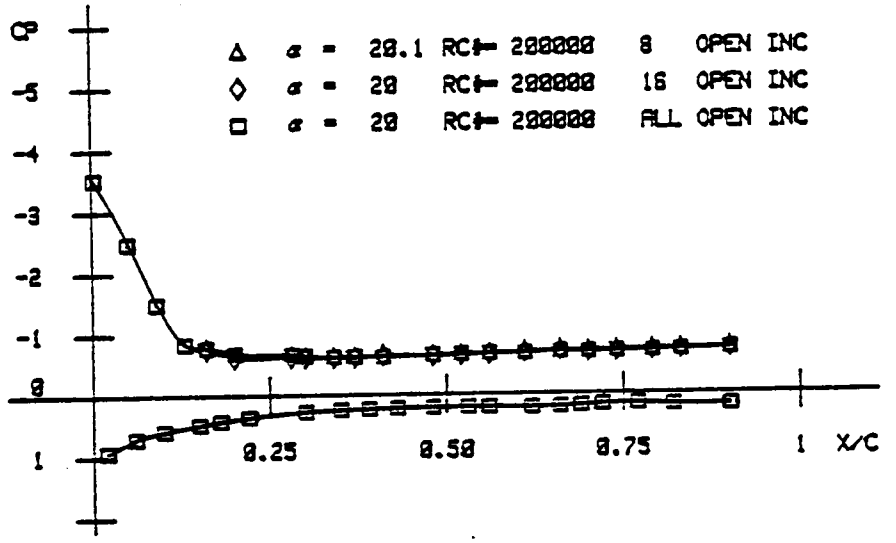

Fig. 4.46 Cp→ $\frac{x}{c}$ comparison of 8, 16 and all holes open

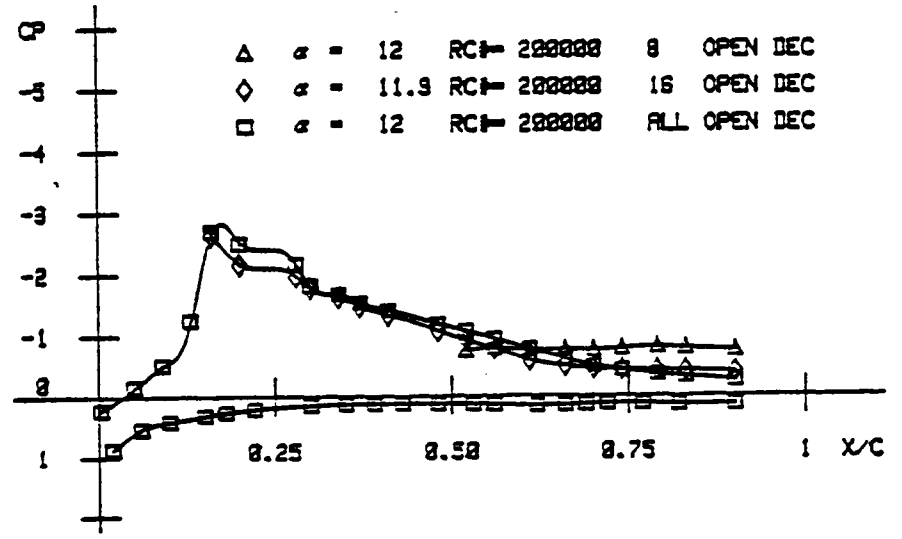

Fig. 4.47 Cp→ $\frac{x}{c}$ comparison of 8, 16 and all holes open

Fig. 4.48 Separated flow with pressure taps

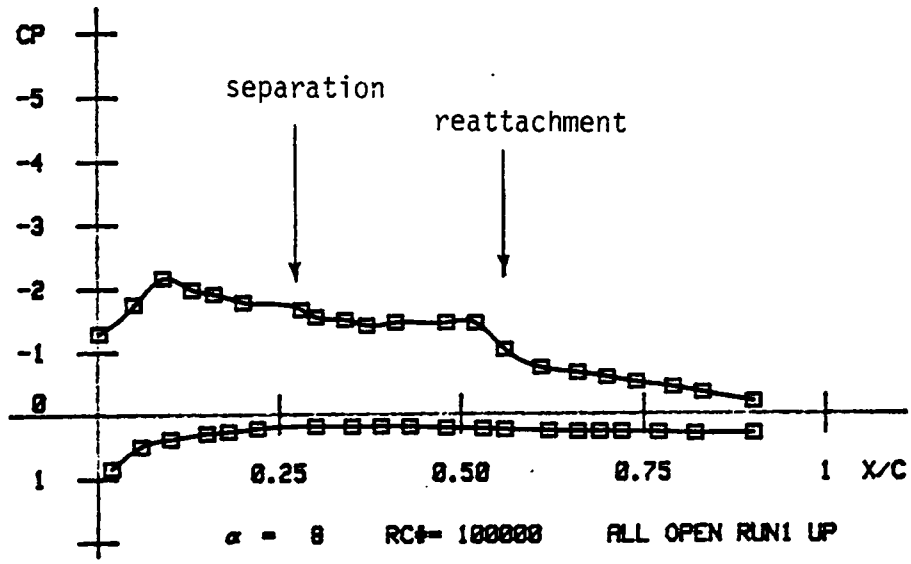

Fig. 4.49 $Cp \rightarrow \frac{x}{c}$ showing larger separation bubble

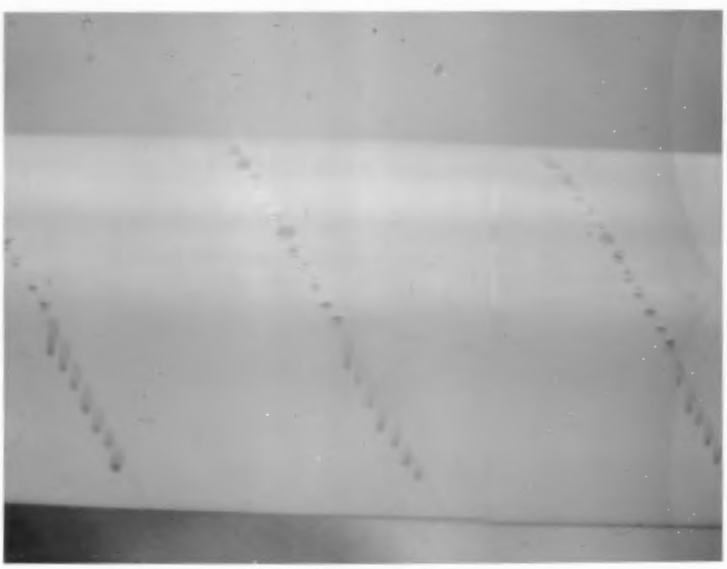

Fig. 4.50 Oil droplet photograph of laminar separation bubble $\alpha=5^0$ Re=200,000

Fig. 4.51 Evaporative film photograph corresponding to Fig. 4. 50
$\alpha=5^0$ Re=200,000

5.) COMPUTATIONAL RESULTS OF THE EPPLER CODE

In order to evaluate the performance of the code that has been developed by Eppler of the University of Stuttgart for low Reynolds number airfoil design and analysis, the FX-63-137-ESM airfoil was run through this code.

This program was developed by Eppler and Somers especially for what they call low speed airfoils. A complete description of the code can be found in reference 8. Basically the program initially performs an inviscid panel method computation to find the velocity and pressure distribution around the airfoil. After this a boundary layer analysis is performed in order to provide modifications to the lift and to find the drag of the airfoil (since the inviscid drag is approximately 0). The boundary layer calculations are accomplished by use of an integral method. All criteria for separation, transition etc. are of empirical nature. There is no specific treatment in the program for laminar separation bubbles other than the fact that as soon as laminar separation is detected a check of the local pressure gradient is performed and if the conditions for reattachement are met the boundary layer computations are continued from the laminar separation

point using the turbulent laws. Even though this is not an accurate way of handling the laminar separation bubble it should influence global results only little. After the initial boundary layer calculation it is possible to specify one displacement thickness iteration. This means that the shape of the body is modified by the displacement thickness of the boundary layer. Then a panel method computation is again performed using the new shape. After this the boundary layer computations are repeated using the new velocity distributions.

The program was run for the FX-63-137-ESM in both modes, with and without dispalcement iteration. It turned out that for the lift and drag data the displacement iteration did not show any effect on the results at all. There were some changes in the moment coefficient but these were limited to less than 5%.

Fig. 5.1 shows the lift results for the Eppler code both before boundary layer calculations and after and the experimental results for the aspect ratio 10 wing corrected for infinite aspect ratio. The Reynolds number for the experimental case is 250,000 and for the computational results 2 different Reynolds numbers of 300,000 and 1000,000. For a Reynolds number of 300,000 the stalling angle is only 6 degrees which is entirely

incorrect. For a Re of 1000,000 though the computations agree very well with the 250,000 experimental data. From this it can be concluded that the inviscid part of the code (panel method) does a good job of predicting the flow around the airfoil but the boundary layer analysis is inadequate at low Reynolds numbers.

Fig. 5.2 shows the drag results for the same cases as above. There is no inviscid curve since the inviscid drag prediction is zero anyway. The drag of the experimental case is corrected to infinite aspect ratio by excluding the induced drag. Drag predicition is seen to fail at negative angles of attack and is somewhat lower than the experimental data at higher angles of attack. The hysteresis loop is not predicted at all.

Fig. 5.3 shows the pitching moment data for the above cases. The prediction for Re=1000,000 cannot be compared to the experimental data. For the Re=300,000 predicition it appears that the trend is predicted accurately however moment coefficients are predicted too low. Also above an angle of attack of 17 degrees the Re=300,000 case falls to the same level as the Re=1000,000 case which is not present in the experimental data.

It should be noted that the Eppler code is, by

nature of the modeling used, not capable of predicting the hysteresis loop. Recently programs have been developed that are able to do an efficient and accurate computation of the flow in the laminar separation bubble (29,30,31). These programs use a viscous inviscid interaction scheme which is necessary since the separated flow region doe influence the inviscid outer flow. It would be beneficial for the Eppler codes accuracy if such a scheme could be incorporated into the program. Since the only part of the Eppler code that does produce good results is the inviscid part and this part predicts the lift with accuracy similar to thin airfoil theory for this airfoil the theory prediction is just as good as the computational one.

The reason for the inadequacy of this code is its inability to deal correctly with the laminar separation bubble. In the design mode where the appearance of a bubble is actively avoided this code produces good results.

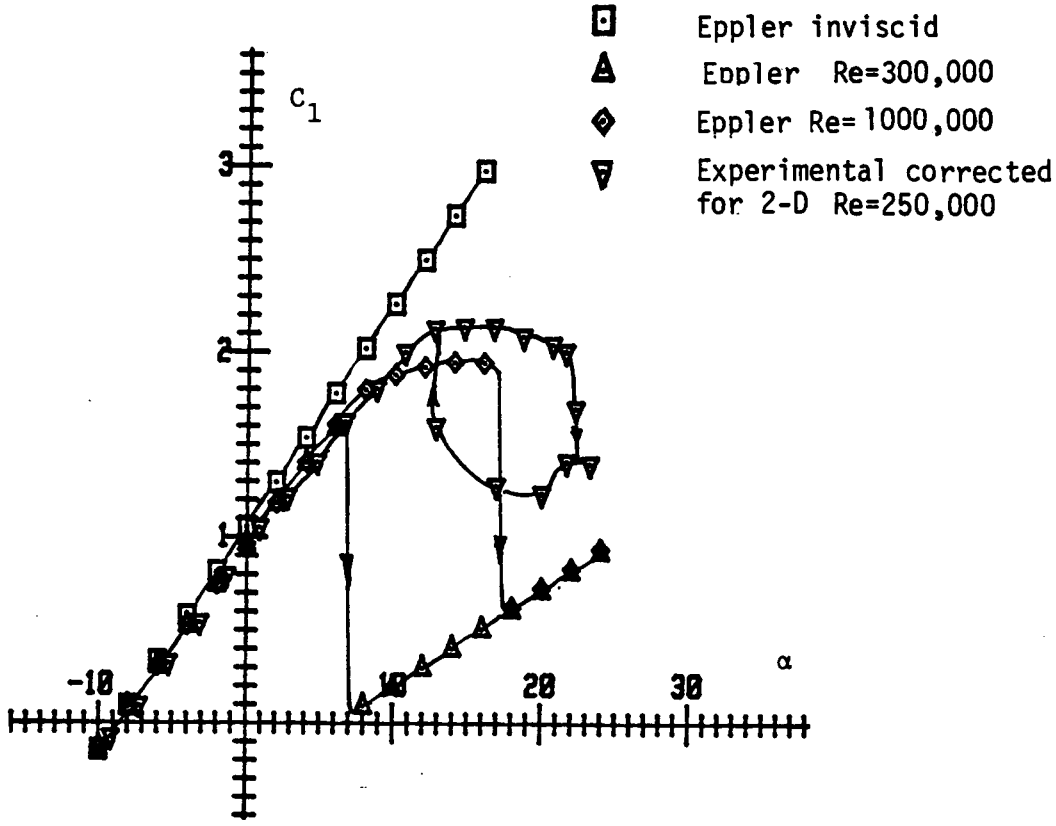

Fig. 5.1 $C_l \rightarrow \alpha$ for Eppler code and experiment

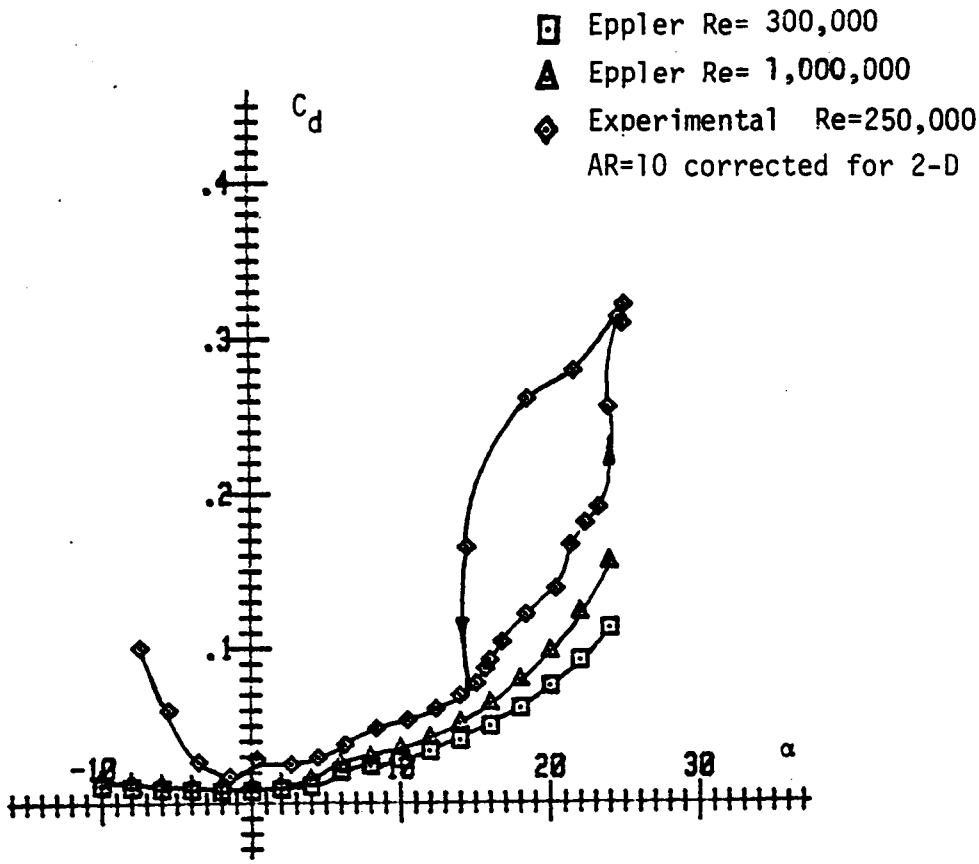

Fig. 5.2 Cd→α for Eppler code and experiment

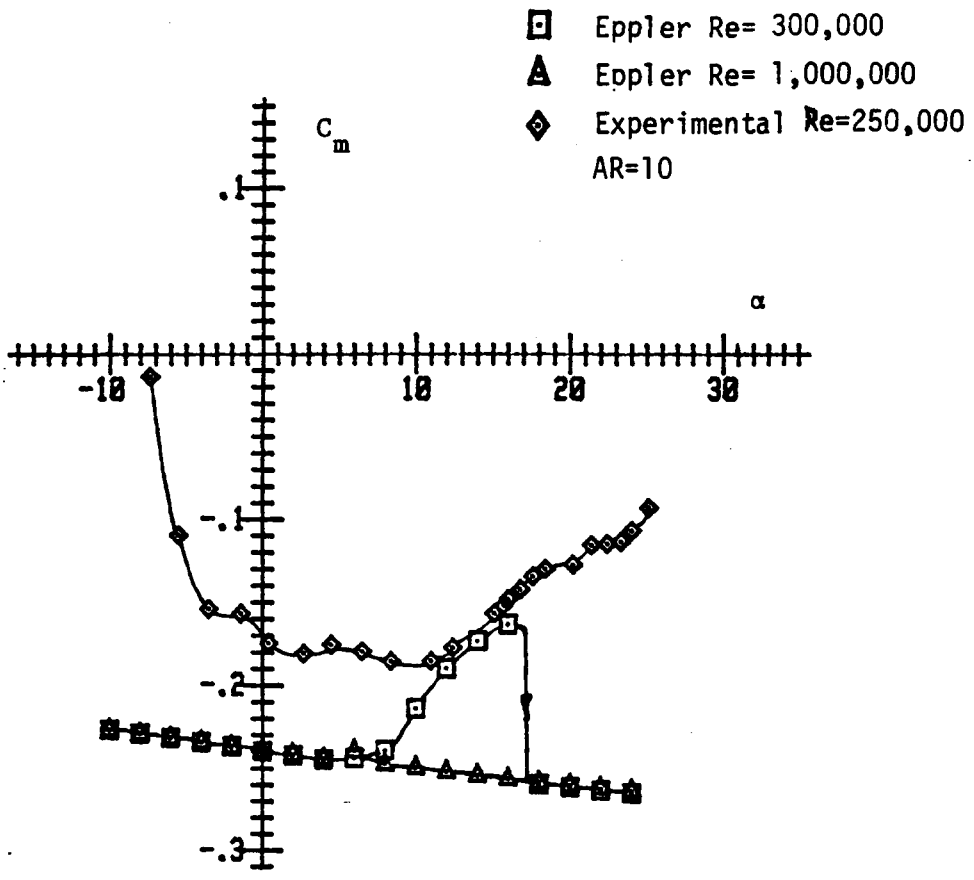

Fig. 5.3 $C_m \rightarrow \alpha$ for Eppler code and experiment

6.) CONCLUSIONS

In this study the primary objective was to determine the effect of aspect ratio in particular and in general the effect of three dimensionality on the flow around wings at low Reynolds numbers. It was seen that the effects observed at high Reynolds number are also present in this Re range. There is the usual increase in lift slope and this increase can even be predicted with reasonable accuracy using Prandtl's lifting line theory. In addition to the change in lift slope the zero lift angle of attack was also influenced by the aspect ratio.

Through flow visualization it was ascertained that the wingtips have a rather restricted effect on the laminar separation bubble. The dissappearance of the bubble extends only for a small distance inboard from the tips.

The size of the hysteresis loop and the Reynolds number at which hysteresis starts was found to be influenced by the aspect ratio.

The momentum deficit method was used to validate the data obtained by the strain gauge method and there was adequate agreement between the values found through the two methods.

From the measurements of pressure done around the airfoil contour one could determine both the location of the laminar separation bubble and the regions were flow is separated. The pressure taps themselves were found to influence measurements somewhat in certain regions of angle of attack and Reynolds number.

In the future it would be beneficial to continue strain gauge measurements on this airfoil with flaps and control surfaces to determine their effect on the formation of the laminar separation bubble. Also measurements on other shapes would give more insight into the phenomena occuring here. The effects of turbulence and noise will have to be investigated in detail to determine what performance to expect from an actual aircraft. Finally detailed measurements on boundary layer stability and its effect on the occurence of reattachment should be studied in detail to gain insight into the reasons for the presence of a hysteresis loop in stall at these Reynolds numbers.

7.) REFERENCES

1. Schmitz, F.W. - "Aerodynamics of the Model Airplane." Ludwig Prandtl Prize 1941, Translation by Redstone Scientific Information Center

2. Althaus, D. - "Profilpolaren fur den Modellflug." N. V. Neckar Verlag, Villingen-Schwenningen, 1980

3. Volkers, D.F. - "Preliminary Results of Wind Tunnel Measurements on some Airfoil Sections at Reynolds Numbers between 60,000 and 500,000." Delft University of Technology, Memo M-276, June 1979

4. Carmichael, B.H. - "Low Reynolds Number Airfoil Survey." NASA CR 165803 Vol. 1, November 1981

5. Pohlen, L.J. & Mueller, T.J. - "Boundary Layer Characteristics of the Miley Airfoil at low Reynolds Numbers." AIAA Applied Aerodynamics Conference, Danvers Massachussetts, July 1983

6. Knapp, C.F. & Roache, P.J. -"A Combined Visual and Hot Wire Anemometer Investigation of Boundary Layer Transition." AIAA Journal, Vol. 6, No. 1, Jan. 1968

7. White, F.M. - "Viscous Fluid Flow." Mc Graw Hill Inc., 1974

8. Eppler, R. & Somers, D.M. - "A Computer Program for the Design and Analysis of Low Speed Airfoils." NASA TM 80210, 1980

9. Maekawa, T. & Atsumi, S. - "Transition Caused by The Laminar Flow Separation." NACA TM 1352

10. Mc Cullough, G.B. & Gault, D.E. - "Examples of the Three Representative Types of Airfoil Section Stall at Low Speed." NACA TN 2502, September 1951

11. Gault, D.E. - "An Experimental Investigation of Separated Laminar Flow." NACA TN 3505, 1955

12. van Ingen, J.L. - "On the Calculation of Laminar Separation Bubbles in 2-D Incompressible Flow." AGARD Symposium at Gottingen, May 1975 , AGARD CP 168

13. van Ingen, J.L. - "Transition, Pressure Gradient, Suction, Separation and Stability Theory." AGARD Conference Proceedings No. 224, Laminar Turbulent Transition, 1977

14. Venkatesworlu, K. & Marsden, D.J. - "Prediction of Boundary Layer Development in the Presence of a Laminar Separation Bubble." University of Alberta, Edmonton, Canada, 1980

15. Kuethe, A.M & Chow, C.Y. - "Foundations of Aerodynamics." John Wiley & Sons Inc. , New York , 1976

16. Dommash, D.O. & Sherby, S.S. & Connolly, T.F. - "Airplane Aerodynamics." Pitman Publishing Corp. , New York , 1967

17. Abbott, I.H. & von Doenhoff A.E. - "Theory of Wing Sections." Dover Publications Inc. , New York , 1959

18. "Programming Techniques for the HP 9836 Desktop Computer." Hewlett-Packard Desktop Computer Division , Fort Collins , Colorado , 1982

19. "3052 Automatic Data Acquisition System Guide." Hewlett Packard Desktop Computer Division , Fort Collins , Colorado , 1976

20. Sumantran, V. & Sun, Z. & Marchman, J.F. - "Acoustic and Turbulence Influence on Low Reynolds Number Wing Pressure Distributions." Conference on Low Reynolds Number Aerodynamics , University of Notre Dame Notre Dame , Indiana , June 1985

21. Weihs, D. & Katz, J. - "Cellular Patterns in Poststall Flow over Unswept Wings." AIAA Journal, Vol. 21 , No. 12 , December 1983

22. Mueller, T.J. - "Low Reynolds Number Vehicles." AGARDograph No. 288 , AGARD (NATO) , February 1985

23. Miley, S.J. - "A Catalog of Low Reynolds Number Airfoil Data for Wind Turbine Applications." Texas A&M University , College Station , Texas , February 1982

24. Schaefer, C.G. - "Acoustic Effects on Stall Hysteresis for Low Reynolds Number Flow." AIAA Southeast Regional Conference , Atlanta , Georgia , April 1985

25. Mueller, T.J. - "The Influence of Laminar Separation and Transition on Low Reynolds Number Airfoil Aerodynamics." University of Notre Dame , Notre Dame , Indiana , 1984

26. Mueller, T.J. & Batill, S.M. - "Experimental Studies of the Laminar Separation Bubble on a Two-Dimensional Airfoil at Low Reynolds Numbers." AIAA 13th Fluid and Plasma Dynamics Conference , Snowmass , Colorado , July 1980

27. Mueller, T.J. & Pohlen, L.J. & Conigliaro, P.E. & Jansen, B.J. - "The Influence of Free Stream Disturbances on Low Reynolds Number Airfoil Experiments." Experiments in Fluids 1 , Springer Verlag , Heidelberg , 1983

28. Crimi, P. & Reeves B.L. - "Analysis of Leading Edge Separation Bubbles on Airfoils." AIAA Journal , Vol. 14 , No. 4 , 1976

29. Carter, J.E. & Vasta, V.N. - "Analysis of Airfoil Leading Edga Separation Bubbles." NASA CR 165935, May 1982

30. Davis, R.L. & Carter, J.E. - "Analysis of Airfoil Transitional Separation Bubbles." AIAA 17th Fluid Dynamics, Plasma Dynamics, and Lasers Conference, Snowmass Colorado, June 1984

31. Gleyzes, C. & Cousteix, J. & Bonnet, J.L. - "A Calculation Method of Leading Edge Separation Bubbles." ONERA/CERT, Toulouse, France

APPENDIX A

Coordinates of the FX-63-137-ESM Airfoil

Point #	x/c	y/c upper	y/c lower
1	1	0	0
2	.9989	.0007	.0004
3	.9957	.0025	.0017
4	.9904	.0050	.0037
5	.9830	.0082	.0063
6	.9735	.0119	.0092
7	.9619	.0160	.0122
8	.9484	.0204	.0151
9	.9330	.0252	.0179
10	.9157	.0302	.0205
11	.8967	.0355	.0228
12	.8759	.0411	.0248
13	.8535	.0471	.0263
14	.8297	.0532	.0273
15	.8044	.0596	.0277
16	.7778	.0661	.0274
17	.7500	.0727	.0267
18	.7211	.0793	.0253
19	.6913	.0859	.0234
20	.6607	.0921	.0210
21	.6294	.0980	.0181
22	.5975	.1034	.0148
23	.5653	.1082	.0111
24	.5327	.1123	.0072
25	.5000	.1157	.0031
26	.4673	.1184	-.0010
27	.4347	.1203	-.0049
28	.4024	.1214	-.0084
29	.3706	.1218	-.0117
30	.3393	.1214	-.0145
31	.3087	.1201	-.0169
32	.2787	.1180	-.0189
33	.2500	.1151	-.0204
34	.2222	.1113	-.0215
35	.1956	.1069	-.0223
36	.1703	.1018	-.0227
37	.1464	.0961	-.0227
38	.1241	.0898	-.0225
39	.1033	.0829	-.0219
40	.0843	.0757	-.0211

Point #	x/c	y/c upper	y/c lower
41	.0670	.0681	-.0201
42	.0516	.0603	-.0188
43	.0381	.0522	-.0172
44	.0265	.0440	-.0152
45	.0170	.0357	-.0128
46	.0096	.0270	-.0097
47	.0043	.0157	-.0057
48	.0011	.0090	-.0023
50	0	0	0

APPENDIX B

Hardwired Channel Assignment in Stabilty Wind Tunnel

Channel	Connected to
1	tunnel temperature
2	static pressure
3	lift
4	drag
5	pitching moment
6	sideforce
7	yawing moment
8	rolling moment
9	dynamic pressure

The vita has been removed from the scanned document